

THESIS ON CIVIL ENGINEERING F26

**Wave Scattering at Discontinuities in
Plates and Pipes**

MADIS RATASSEPP

TUT
PRESS

TALLINN UNIVERSITY OF TECHNOLOGY
Faculty of Civil Engineering
Department of Mechanics

The dissertation was accepted for defence of the Degree of Doctor of Philosophy in Engineering on January 22, 2010.

Supervisors: Professor Aleksander Klauson (Tallinn University of Technology, Estonia), Professor Micheal John Stewart Lowe (Imperial College London, UK)

Opponents: Professor Jüri Engelbrecht (Institute of Cybernetics at Tallinn University of Technology, Estonia), Professor Mihai V. Predoi (Department of Mechanics at University Politehnica Bucharest, Romania)

Defence of the thesis: February 23, 2010

Declaration:

Hereby I declare that this doctoral thesis, my original investigation and achievement, submitted for the doctoral degree at Tallinn University of Technology has not been submitted for any academic degree.

/Ratassepp /

Copyright: Madis Ratassepp, 2010
ISSN 1406-4766
ISBN 978-9985-59-965-5

EHITUS F26

Lainete interaktsioon defektidega plaatides ja torudes

MADIS RATASSEPP

Contents

1	Introduction	13
1.1	Motivation	13
1.2	Aim of investigation	14
1.3	Acknowledgements	15
2	Normal mode expansion (NME) for modelling the interaction of axisymmetric longitudinal waves with discontinuities in a pipe	16
2.1	Background	16
2.2	Wave propagation in an infinite isotropic pipe	17
2.2.1	Solution of the wave equation	17
2.2.2	Displacement and stress field	18
2.2.3	The characteristic dispersion equation	19
2.2.4	Properties of the modes	20
2.3	Description of the NME method	25
2.3.1	Solving the boundary value problem	25
2.3.2	Convergence of the solution: conservation of the energy	27
2.4	Example1: edge resonance in a semi-infinite thick pipe	28
2.4.1	Introduction	28
2.4.2	Modelling procedures	29
2.4.3	Experimental setup	32
2.4.4	Results and discussion	33
2.5	Example2: wave interaction with a vertical part-through crack in a thick pipe	42
2.5.1	Introduction	42
2.5.2	Modelling procedures	43
2.5.3	Results and discussion	47
2.6	Summary	52
3	Scattering of the SH_0 mode in a plate when incident at a crack aligned in the propagation direction of the mode	54
3.1	Background	54
3.2	Low frequency guided waves in a plate	55
3.3	Finite Element modelling	56
3.3.1	Plate with a through-thickness notch	56
3.3.2	Plate with a part-through notch	60
3.4	Experimental work	60
3.5	Results and discussion	63
3.5.1	Through-thickness crack: reflection and diffraction as a function of crack length	63

3.5.2	Through-thickness crack: influence of the distance of source and measurement location on direct reflection	67
3.5.3	A through-thickness crack: the influence of a "leaky type" surface wave on SH_0 reflection in the incident direction . . .	69
3.5.4	A part-through crack: reflection and diffraction as a function of defect depth, width and frequency-thickness	72
3.6	Summary	75
4	T(0,1) mode interaction with axial crack in pipes	76
4.1	Background	76
4.2	Experimental work	77
4.3	Finite Element modelling	79
4.3.1	The membrane model for through-thickness axial crack . . .	79
4.3.2	3D model for part-through axial crack	79
4.4	Results	80
4.4.1	Through-thickness notch (membrane models)	80
4.4.2	Part-thickness notch (3D model)	85
4.5	Discussion	88
4.5.1	The effect of frequency and pipe circumference in case of a through-thickness crack	89
4.5.2	Estimating the smallest detectable crack depth	90
4.5.3	The effect of the crack shape	93
4.6	Summary	94
5	Conclusions	95
5.1	Summary of findings	95
5.2	Recommendation for future research	96
	References	97
	List of publications	105
	Abstract	106
	Kokkuvõte	107
	Curriculum Vitae	108
	Elulookirjeldus	110

List of Tables

1	Material and geometric properties of the aluminium pipe used in the study.	22
2	Summary of FE models used in the study.	31
3	Predicted edge resonance frequencies by numerical and FE model . . .	38
4	Material properties for steel used in the FE plane stress model. . . .	57
5	Material properties for the aluminium used in the FE 3D model. . . .	60
6	Plates with defects used in the experiment.	60

List of Figures

1	Transducer array employed for guided wave inspection of pipes. . . .	14
2	Formulation of the problem in cylindrical coordinates.	18
3	Axial wave number ξ dispersion curves for a pipe. Material properties are given in Table. 1	23
4	The zoomed area in Fig. 3 at low frequencies showing the difference between the wave numbers ξ of the pipe modes $L(0, 1)$, $L(0, 2)$ and the plate Lamb modes A_0 , S_0	23
5	The dependence of phase velocity c_{ph} of the $L(0, 1)$ mode on the curvature parameter Δ	24
6	Axial u_z (solid line) and radial u_r (dashed line) displacements of the $L(0, 1)$ mode. a) $\Delta \approx 0.25$; b) $\Delta = 1$	24
7	a) modulus of normalized axial u_z (solid line) and radial u_r (dashed line) displacements of the complex modes, b) modulus of normalized stresses σ_{zz} (solid line) and σ_{rz} (dashed line); $\Delta \approx 0.25$ and $fd = 0.1\text{MHz}\cdot\text{mm}$	25
8	Formulation of the scattering problem for axi-symmetric longitudinal waves in the wall of the pipe	26
9	$L(0,m)$ mode reflection at the edge of the pipe wall.	30
10	a) FE axi-symmetric model of the pipe; b) group velocity dispersion curves for axi-symmetric longitudinal modes propagating in an aluminium pipe, $\Delta= 1.0$	31
11	a) Typical time record showing the edge resonance in case of $L(0,2)$; center frequency-thickness product is $2.335\text{ MHz}\cdot\text{mm}$; $\Delta=0.25$. b) Frequency spectrum of the resonance part of the signal shown in a).	32
12	Scheme of the experimental setup.	33
13	Reflection of $L(0,2)$ mode at a pipe edge. The parameters of the pipe: $a = 40\text{ mm}$, $d = 1\text{ mm}$, $\Delta = 0.025$, $\rho = 7800\text{ kg/m}^3$, $c_L = 1000\text{ m/s}$, $c_T = 577.4\text{ m/s}$	34

14	Normalized displacement u_r amplitudes of reflected modes at the edge of the pipe. The parameters of the pipe: $a = 40$ mm, $d = 1$ mm, $\Delta = 0.025$, $\rho = 7800$ kg/m ³ , $c_L = 5850$ m/s, $c_T = 3150$ m/s. . .	35
15	a) Resonance spectrum of normal displacement of L(0,2) mode measured at 0.1 mm from the pipe end. b) Contour plot of measured normal displacements in time and space domain showing the generation of edge resonance.	36
16	Normal surface displacement u_r time record at 0.1 mm from the pipe end at $fd = 2.435$ MHz-mm.	37
17	Normalized radial displacement u_r amplitudes of reflected modes at the edge of the pipe as a function of curvature parameter Δ . (—) GE, (o o o) LS.	38
18	The normal displacement component of the total displacement field at the outer surface of the pipe measured as the function of the distance near the edge at resonance frequency. (—) analytical model, (o o o) FE predictions. The results have been normalized by the outer surface radial displacement amplitude of the incident mode.	39
19	Through-thickness mode shapes of the edge at resonance frequencies for different pipes $\Delta = 0.25$; 0.75; 1.0. Numerical predictions u_r (dashed line), u_z (solid line); FE predictions u_r (o o o), u_z (x x x). The extremities of the normalized radius scale represent the inner and outer radii of the pipe.	39
20	Energy balance of the L(0,2) mode as the function of curvature parameter Δ . a) The energies for the modes have been obtained at resonance frequencies. b) All energies have been calculated at $fd = 2.405$ MHz-mm.	40
21	Energy balance of the L(0,2) mode as the function of frequency-thickness fd for the pipe of $\Delta = 0.667$	40
22	Relative error ϵ in energy balance of the propagating modes as the function of frequency-thickness product fd and curvature parameter Δ ; $\delta = 0$. (—) GE, (o o o) LS.	41
23	Relative error ϵ in energy balance of the propagating modes as the function of number of modes (a) and the parameter δ/s which controls the position of collocation points (b) at $fd = 2.42$ MHz-mm. (x x x) GE, (o o o) LQ.	42
24	L(0,m) mode scattering at the surface crack in the wall of the pipe. .	43
25	FE axi-symmetric model of the pipe with a surface crack.	45
26	Group velocity dispersion curves and some mode shapes for axi-symmetric longitudinal modes with the pipe curvature $\Delta = 0.25$ (thick solid line) and $\Delta = 1$ (solid line).	46

27	Typical time records of u_z displacement from FE simulations; the crack is $p = 50\%$ deep, the pipe's curvature parameter is $\Delta = 0.25$. a) Reflected signal, b) transmitted signal.	47
28	Reflection coefficients of the L(0,2) mode for the full circumference outer crack in a pipe with the depth $p = 50\%$ as the function of frequency; FE - Alleyne <i>et al.</i> , NME - current method.	48
29	Reflection coefficients of the L(0,2) mode from a surface breaking crack, for various depths of the crack and frequency-thickness value; FE - Lowe <i>et al.</i> (solid line), NME - (o o o).	49
30	Through-thickness displacements on both sides of an outer-surface crack ($p = 50\%$) in a pipe for the incident L(0,2) mode at 1.12 MHz-mm. Result from Castaings <i>et al.</i> (solid line), pipe NME results: u_z - (x x x), pipe u_r - (o o o).	49
31	Predicted (a) reflection and (b) transmission coefficients of L(0,2) mode and relative error ϵ in energy balance (dotted line) for L(0,2) incident on outer and inner surface crack as a function of relative crack depth at 1.3 MHz-mm. NME results (—); FE results (o o o).	50
32	Predicted (a) reflection and (b) transmission coefficients of L(0,1) mode for L(0,2) incident on the outer and inner surface crack as a function of relative crack depth at 1.3 MHz-mm. NME results (—) and various FE results.	51
33	Predicted FE results showing (a) mode conversion intensity and (b) mode conversion intensity ratio for inner and outer cracks for L(0,2) incident at 1.3 MHz-mm.	52
34	Group velocity dispersion curves for shear and Lamb waves in a steel plate.	56
35	Predominant displacement mode shapes of A_0 , S_0 and SH_0 at low frequencies propagating in x -direction.	57
36	(a) Setup of the FE model. (b) Typical FE time record showing the displacement amplitudes of reflected and diffracted waves around the crack after the interaction of the SH_0 mode with the 24mm long crack.	58
37	FE defect models: (a) crack, (b) rectangular notch, (c) V-notch.	59
38	Arrangement of the experimental test. (a) side view, (b) plan view.	61
39	Typical experimental signals; center frequency is 200kHz; the through-thickness notch is 12 mm long. (a) time record from the 1 st monitoring point 118 mm away from notch, (b) time record from the 2 nd monitoring poing 118 mm away from notch. Both signals are plotted to the same scale.	62
40	Typical FE time records from the (a) first, (b) second, and (c) third monitoring points showing the reflected and diffracted signals; 0.7 mm wide notch 24 mm in length was used in the model; and center frequency of the incident pulse is 100 kHz.	63

41	Predicted variation of reflection modulus with length of the crack normalized to wavelength. Monitored SH_0 mode at the 1st point: FE results with a 0.7 mm width notch (solid circle), 0.7 mm width V crack (dash-dot), zero-width crack (dotted line), and experimental results (empty circle). Monitored S_0 at the 3rd point - FE results (solid square).	64
42	Predicted variation of diffraction modulus with length of the defect normalized to wavelength. Monitored SH_0 mode at the third point: FE results with a 0.7 mm width notch (solid circle), 0.7 mm width V-notch (dash-dot), crack (dotted line), and experimental results (empty circle).	65
43	Reflection modulus of SH_0 mode for short and long defects. FE results: SH_0 near tip reflection at 0.7 mm V-notch (solid square), SH_0 far tip reflection at 0.7 mm V-notch (solid circle), and SH_0 far tip reflection at the crack (dashed). Experimental SH_0 far tip reflection (empty circle).	66
44	Typical time domain signals showing the reflections at long cracks. (a) FE measurement at 262 mm ($8.1\lambda_{SH_0}$) long crack, center frequency 100 kHz; (b) experimental measurement at 70 mm ($8.1\lambda_{SH_0}$) long crack, center frequency 390 kHz.	67
45	FE predictions of SH_0 reflection modulus as a function of crack length for various source distances λ_s from the crack. The distance between the source and monitoring point was always $5\lambda_{SH_0}$	68
46	FE predictions of the dependence of reflection modulus on the distance between the source and the crack for different crack length to wavelength ratios. Reflection modulus extrapolated from the source distance $40\lambda_{SH_0}$ (line), reflection modulus obtained using the source distances 10, 20 and $30\lambda_{SH_0}$ (empty circle).	68
47	Various FE time records showing the displacement amplitudes of the wave field around the crack during the interaction of the SH_0 mode with the crack. (a) Incident SH_0 mode interaction with the near tip of the crack. (b) Rayleigh type wave interaction with the far tip of the crack. (c) Reflected and diffracted waves after back propagating leaky and Rayleigh type wave interaction with the near tip of the crack.	70
48	FE time traces; the length of the crack is $15\lambda_{SH_0}$; center frequency is 100 kHz. (a) Measurement at the second point; (b) measurement at the first point.	71
49	Phase differences from FE simulations as a function of crack length. (a) ϕ_2 and its slope showing the wave number of Rayleigh type surface waves; (b) ϕ_3 and its slope showing the wave number of leaky type surface waves.	71

50	Predicted (a) reflection and (b) diffraction coefficients from an 80% deep crack and 0.6 mm wide notch expressed as a function of ratio of defect length to incident wavelength. The SH_0 mode was excited at 250 kHz in a 3 mm thick plate.	72
51	Measured (empty) and predicted (solid) (a) reflection and (b) diffraction coefficients from an 80% and 100% deep (dashed line) notch expressed as a function of ratio of defect length to incident wavelength. Measurements and predictions are made within the frequency range of 200 to 325 kHz.	73
52	Predicted variation of (a) reflection and (b) diffraction coefficient as the function of depth of the crack normalized to wavelength $l/\lambda_{SH0} = 0.7$. The SH_0 mode was excited at 100, 250 and 350 kHz in a 3 mm thick plate.	74
53	Predicted (a) reflection and (b) diffraction coefficient versus frequency-thickness for 80% deep crack in a plate at $l/\lambda_{SH0} = 0.7$	75
54	Experimental setup of pipe testing.	78
55	Predicted FE (a) and experimental (b) time record for a 5 inch pipe with a 56 mm axial notch, and a 5-cycle T(0,1) mode incident at 35 kHz.	81
56	Variation of the reflection coefficient with the length of the notch normalized to wavelength for a 5 inch pipe and T(0,1) mode incident at 30, 35 and 40 kHz; (ooo) - experiment, (solid line) - FE membrane model with a notch, (dashed line) - FE membrane model with a crack.	82
57	Variation of the reflection coefficient with the length of the crack normalized to wavelength at various frequencies for a 5 inch pipe.	83
58	Results for a 5-cycle T(0,1) mode incident at an axial crack $l = 36mm(l/\lambda = 0.524)$: (a) predicted FE time record and (b) reflection coefficient as the function of frequency and pipe circumference for 5 inch pipe at 45 kHz.	84
59	Variation of reflection coefficient with circumference: (solid line) - time domain values at 45 kHz, (dashed line) - frequency domain values at 45 kHz, (solid triangle) - values at 15 to 60 kHz for a 5 inch pipe.	85
60	Predicted FE time record from 56 mm 80% deep axial notch at 35 kHz for a 5 inch pipe.	86
61	Variation of reflection coefficient with a length of the 80% deep notch normalized to wavelength at 35 and 40 kHz for a 5 inch pipe; (ooo) - experiment, (solid line) - 3D model with a notch, (dashed line) - 3D FE model with a crack.	86
62	Variation of reflection coefficient with length of the 80% deep crack normalized to wavelength at various frequencies for a 5 inch pipe.	87

63	Predicted variation of normalized reflection coefficient with the length of crack normalized to wavelength for 60% and 80% deep cracks. (solid line) - plate FE results, (ooo) - pipe FE results; waves were excited at 250 kHz and the thickness of the structure was 3 mm. . .	88
64	Variation of the crack length with a frequency for reflection amplitude 2% from incident wave amplitude for schedule 80 pipes; results derived from FE 5 inch pipe membrane model.	90
65	Results for schedule 80 pipes and T(0,1) mode incident: (a) 3D graph of reflection coefficient from axial cracks with varying depth and length and (b) contour curves of reflection coefficients 1, 2, 3, 4 and 5% at 35 kHz in a 5 inch pipe; (c) variation of the crack length with depth and frequency for a reflection amplitude of 2% from incident wave amplitude for various pipe sizes, results are derived from the FE 5 inch pipe membrane model.	92
66	Schematic representation of irregularly shaped cracks (a) and (b). (c) Variation of reflection coefficient with a crack circumferential width w for the 24mm long and 80, 100% deep crack. The results are for T(0,1) incident at 45kHz in a 5 inch schedule 120 pipe. (empty circle) - crack (a), (solid triangle) - crack (b).	93

1 Introduction

1.1 Motivation

Routine monitoring of large areas such as plate and pipe structures is an important topic ensuring the safety for power and oil industries. For such aging structures, the presence of hidden damage can severely limit their performance and cause extensive environmental and economic damage. One potential inspection solution is to employ non-destructive testing (NDT) techniques which should detect defects that are still smaller than a given critical size before they lead to failure.

Among the various NDT techniques, ultrasonic guided waves are becoming established for the inspection of plate and pipe structures [1, 2]. This technique is particularly advantageous since ultrasonic waves are guided by the structure to enable the monitoring of large areas from a single point as shown in Fig. 1. By generating waves in a chosen direction in the structure and then analyzing received reflections, it is then possible to locate and quantify any defects along the line of wave propagation. This reduces inspection time substantially and also enables the inspection of areas in structures that are not directly accessible (for example, insulated pipes). This is not possible with conventional local point-by-point scanning techniques.

For long range pipe testing, axi-symmetric longitudinal $L(0,2)$ and torsional $T(0,1)$ mode are commonly used [3]. These modes can be easily excited and received at one axial location using an array of transducers distributed around the circumference of the pipe. Uniform wave field around the pipe circumference due to axi-symmetry and nearly constant mode shape through the wall thickness allow to achieve 100% pipe wall inspection coverage. Moreover both modes can propagate long axial distances (tens of meters in either direction) without significant loss of signal strength and maintain their waveforms due to non-dispersive nature. The development and research of using these modes for inspection purposes is well covered in literature.

An important subject in this field has been to understand how the guided waves interact with different type of discontinuities. It is essential when processing received signals properly for those which arise due to scattering from different defects and features. However, the wave interaction with discontinuities is a complex phenomenon which has not been explained for all of the possible cases encountered in real life. Previous theoretical studies with guided waves usually employed a simplified model of the defect, but typically do not make use of all available information, so there is potential for improvement. In this thesis we deal with understanding the effect of some geometrical discontinuities on guided wave propagation in plates and pipes. The background literature on different issues is presented in the relevant chapters.



Figure 1. Transducer array employed for guided wave inspection of pipes.

1.2 Aim of investigation

This thesis will focus on the interaction of ultrasonic guided waves with geometric discontinuities in a wave-guide structure. The aim is to bring new understanding into the detection capability of existing guided wave testing systems, as well as to aid the signal processing procedure used by these systems. Two separate problems are investigated by using semi-analytical approaches, finite element (FE) methods and experimental measurements. The specific objectives are:

- Develop a numerical model which is based on normal mode expansion technique and to help analyzing longitudinal wave interaction with discontinuities in a cylindrical pipe. The reflection of $L(0,2)$ mode from a free edge of a pipe wall will be studied in order to give understanding on the role of different wave modes participating in the scattering phenomenon. Secondly, the interaction of $L(0,2)$ mode with a circumferential surface breaking crack will be examined in order to find out the sensitivity to inner and outer surface cracks. Influence of the pipe curvature on the scattering problems will be discussed.
- Investigate the detection capability of cracks which are aligned in the propagation direction of the wave. Two FE models will be exploited. Firstly, the study with a low frequency shear horizontal mode SH_0 in a plate will be performed to understand the key physical mechanism and to evaluate the sensitivity to

such defects. Secondly, the interaction of low-frequency torsional mode $T(0,1)$ with an axial crack in a pipe is studied. A systematic analysis of the reflection coefficient will be carried out as the function of pipe size, defect size, and frequency of the incident signal.

1.3 Acknowledgements

This research would not have been performed without the excellent guidance and invaluable support of my supervisor, Professor Aleksander Klauson and my coadvisor, Professor Mike Lowe.

I would also like to thank Professor Gerard Maze and his colleagues Dr. Farid Chati and Dr. Fernand Leon from LeHavre Ultrasound Laboratory for contributing to my research at the beginning of my studies.

I would like to express my gratitude to Professor Peter Cawley, Professor Mike Lowe and Dr. Francesco Simonetti for offering me a chance to conduct research in the Non-destructive Testing (NDT) Lab at London Imperial College. Special thanks go to the present and former members of NDT Lab: Dr. Frederic Cegla, Dr. Tindaro Cicero, Dr. Thomas Clarke, Dr. George Connolly, Dr. Jacob Davies, Dr. Mickael Drozd, Dr. Matthew Fleming, Sam Fletcher, Dr. Daniel Hezze, Dr. Bubyong Kang, Dr. Jian Ma, Dr. Marco Morbidini, Dr. Prabhu Rajagopal, Dr. Giuseppe Sposito, David Fan, Dr. Pierre Belanger and David Tomlin.

I would like to acknowledge the Estonian Science Foundation and the Imperial College NDT Group which funded this work.

Finally, I would like to thank my parents and, of course, Kristel for their encouragement and support throughout my studies.

2 Normal mode expansion (NME) for modelling the interaction of axi-symmetric longitudinal waves with discontinuities in a pipe

2.1 Background

The aim of this chapter is to examine the axi-symmetric longitudinal wave propagation in a pipe and their interaction with discontinuities in the pipe wall.

A large number of wave modes can exist in a pipe with different propagation characteristics. Each mode is described by its dependence on frequency, called dispersion, but also the distribution of field variables over the cross section of the pipe, referred to as mode shape. When a specific propagating mode interacts with the discontinuity, scattering occurs. In general, this is a very complicated phenomenon because the wave field near the discontinuity is transformed and represents a diverse superposition of propagating and infinite number of nonpropagating modes. The resulting vibration depends on many parameters of the system such as the geometry of the waveguide, the shape of the discontinuity, the stress level of the incident mode at the defect location and is therefore difficult to interpret.

Such scattering problems can be solved analytically only for limited cases, and usually a numerical approach is therefore required. Papers can be found on this subject, presenting models either on finite element, boundary element or hybrid methods [4–6]. Although these numerical models allow to predict the amplitudes of scattered waves, they usually are time consuming for parametric analysis and do not provide easily a detailed information about the physics of the scattering process. This can be achieved with semi-analytical approaches such as NME technique [7] which allows flexible treatment of input data and fast computation. In this method the wave field is expanded into the so-called normal modes which must satisfy the boundary conditions of the wave-guide with discontinuity. Previously, this method has been introduced for various geometries and interaction problems. Engan [8] treated the case of torsional waves being scattered from a step change in the waveguide diameter. Vogt *et al.* [9] examined the scattering of longitudinal and torsional waves at a point when a free waveguide enters an embedding material. Grahn [10] investigated the scattering from a circular partly through-thickness hole in a plate. Wang *et al.* [11] considered anti-plane shear wave interaction with an elastic cylinder centered in an isotropic plate. Castaigns *et al.* [12] studied the reflection and transmission of low-order Lamb modes from vertical cracks in a plate. This method can be also applied to the investigation of two-dimensional scattering problems in thick pipes.

The chapter starts with a brief introduction of wave propagation in an infinite pipe. Then NME method is addressed followed by two examples describing the resonance of pipe end and the wave scattering at circumferential surface breaking cracks in case of $L(0,2)$ mode incidence. The effect of pipe curvature on the wave scattering process

is considered. FE modelling and experiments will be used for the validation of the theoretical results.

2.2 Wave propagation in an infinite isotropic pipe

This subsection describes the axi-symmetric longitudinal wave propagation in a cylindrical pipe. The expressions of displacements, stresses and the characteristic dispersion equation for the modes have been given. The dispersion curves for propagating, nonpropagating modes are shown and some characteristic mode shapes illustrated. The derivation of the model is based on the work of Gazis [13] and Pavlakovic [14].

2.2.1 Solution of the wave equation

The motion of isotropic elastic media can be described by Navier's equation

$$\mu \nabla^2 \vec{u} + (\lambda + \mu) \nabla \nabla \cdot \vec{u} = \rho(\partial \vec{u}^2 / \partial t^2), \quad (1)$$

where \vec{u} is the displacement vector, ρ density of the material, λ and μ Lamé's constants and ∇^2 is the three-dimensional Laplace operator. Displacement field \vec{u} can be presented as the sum of scalar and vectorial fields

$$\vec{u} = \nabla \phi + \nabla \times \vec{\psi}, \quad (2)$$

where ϕ is the field's scalar potential and $\vec{\psi}$ vector potential. Inserting potentials into equation (1), it is possible to separate dilatational and rotational fields

$$\begin{aligned} \nabla^2 \phi - \frac{1}{c_L} \frac{\partial^2 \phi}{\partial t^2} &= 0, \\ \nabla^2 \vec{\psi} - \frac{1}{c_T} \frac{\partial^2 \vec{\psi}}{\partial t^2} &= 0, \end{aligned} \quad (3)$$

where c_L and c_T are the longitudinal and transverse wave speeds in the media, respectively. The solutions of (3) can be derived for pipe geometry, shown in Fig. 2, in cylindrical coordinates (r, θ, z) in the form

$$\begin{aligned} \phi(r, \theta, z, t) &= R_\phi(r) e^{i(k_\theta \theta + \xi z - \omega t)}, \\ \vec{\psi}(r, \theta, z, t) &= \vec{R}_\psi(r) e^{i(k_\theta \theta + \xi z - \omega t)}, \end{aligned} \quad (4)$$

where k_θ is wave number's θ -azimuthal component, ξ wave number's z -axial component, ω angular frequency and $R_\phi(r), \vec{R}_\psi(r)$ the quantities describing the fields'

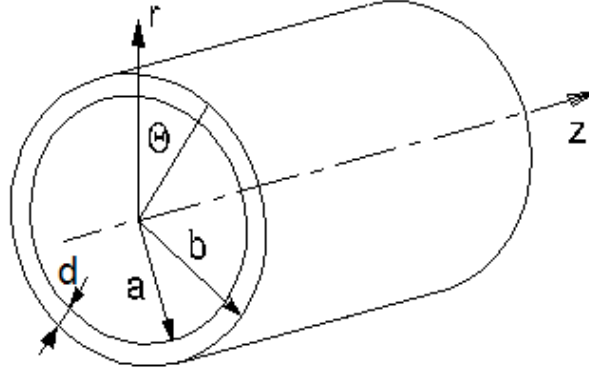


Figure 2. Formulation of the problem in cylindrical coordinates.

dependence on coordinate r . The waves propagating in z -direction and having motion only in (r, z) -plane ($\theta = 0$) can be described with two potentials

$$\begin{aligned}\phi &= f(r)e^{i(\xi z - \omega t)}, \\ \psi_\theta &= -ig(r)e^{i(\xi z - \omega t)}.\end{aligned}\quad (5)$$

Substituting the potentials from (5) into equations (3), we can find the unknowns

$$\begin{aligned}f(r) &= C_1 J_0(\alpha r) + C_3 N_0(\alpha r), \\ g(r) &= C_2 J_1(\beta r) + C_4 N_1(\beta r),\end{aligned}\quad (6)$$

where C_1, C_2, C_3, C_4 are unknown variables and

$$\begin{aligned}\alpha^2 &= \omega^2/c_L^2 - \xi^2, \\ \beta^2 &= \omega^2/c_T^2 - \xi^2.\end{aligned}\quad (7)$$

Here $J_{0,1}$ and $N_{0,1}$ are cylindrical Bessel functions of the first and second kind, respectively.

2.2.2 Displacement and stress field

The displacement components in (r, z) -plane can be found using equation (2)

$$\begin{aligned}u_r &= \frac{\partial \phi}{\partial r} - \frac{\partial \psi_\theta}{\partial z}, \\ u_z &= \frac{\partial \phi}{\partial z} + \frac{1}{r} \frac{\partial}{\partial r}(r\psi_\theta).\end{aligned}\quad (8)$$

This leads to displacement field in terms of potential function of equation (5)

$$\begin{aligned} u_r &= (f' + \xi g)e^{i(\xi z - \omega t)}, \\ u_z &= i(\xi f + \frac{1}{r}g + g')e^{i(\xi z - \omega t)}, \end{aligned} \quad (9)$$

where symbol ' means the derivation $\partial/\partial r$.

The stresses can be found from Hook's Law, which gives the relations between the displacements, strains and stresses

$$\begin{aligned} \varepsilon_{rr} &= \frac{\partial u_r}{\partial r}, \\ \varepsilon_{rz} &= \frac{1}{2}\left(\frac{\partial u_r}{\partial z} + \frac{\partial u_z}{\partial r}\right), \\ \varepsilon_{zz} &= \frac{\partial u_z}{\partial z} \end{aligned} \quad (10)$$

and

$$\begin{aligned} \sigma_{rr} &= \lambda \Delta + 2\mu\varepsilon_{rr}, \\ \sigma_{rz} &= 2\mu\varepsilon_{rz}, \\ \sigma_{zz} &= \lambda \Delta + 2\mu\varepsilon_{zz}, \end{aligned} \quad (11)$$

where

$$\Delta = \nabla^2 \phi = -\left(\frac{\omega^2}{c_L^2}\right) f e^{i(\xi z - \omega t)} = -(\alpha^2 + \xi^2) f e^{i(\xi z - \omega t)}. \quad (12)$$

The resulting stress components in (r, z) -plane in terms of potentials are

$$\begin{aligned} \sigma_{rr} &= [-\lambda(\alpha^2 + \xi^2)f + 2\mu(f'' + \xi g')]e^{i(\xi z - \omega t)}, \\ \sigma_{rz} &= i\mu[2\xi f' + (\xi^2 - \beta^2)g]e^{i(\xi z - \omega t)}, \\ \sigma_{zz} &= [-\lambda(\alpha^2 + \xi^2)f - 2\mu\xi(\xi f + \frac{1}{r}g + g')]e^{i(\xi z - \omega t)}. \end{aligned} \quad (13)$$

2.2.3 The characteristic dispersion equation

The waves propagating in an infinite cylindrical pipe must satisfy stress-free boundary conditions on the inner $(r = a)$ and outer surfaces $(r = b)$

$$\sigma_{rr} = \sigma_{rz} = 0. \quad (14)$$

This leads to the system of linear equations for axi-symmetric longitudinal waves

$$\mathbf{G} \cdot \mathbf{C} = \begin{bmatrix} G_{11} & G_{12} & G_{13} & G_{14} \\ G_{21} & G_{22} & G_{23} & G_{24} \\ G_{31} & G_{32} & G_{33} & G_{34} \\ G_{41} & G_{42} & G_{43} & G_{44} \end{bmatrix} \begin{bmatrix} C_1 \\ C_2 \\ C_3 \\ C_4 \end{bmatrix} = 0, \quad (15)$$

where

$$\begin{aligned} G_{11} &= -(\beta^2 - \xi^2)a^2 J_0(\alpha a) + 2\alpha a J_1(\alpha a), \\ G_{12} &= 2\xi\beta a^2 J_0(\beta a) - 2\xi a J_1(\beta a), \\ G_{13} &= -(\beta^2 - \xi^2)a^2 N_0(\alpha a) + 2\alpha a N_1(\alpha a), \\ G_{14} &= 2\xi\beta a^2 N_0(\beta a) - 2\xi a N_1(\beta a), \\ G_{21} &= 2\xi\alpha a^2 J_1(\alpha a), \\ G_{22} &= (\beta^2 - \xi^2)a^2 J_1(\beta a), \\ G_{23} &= 2\xi\alpha a^2 N_1(\alpha a), \\ G_{24} &= (\beta^2 - \xi^2)a^2 N_1(\beta a). \end{aligned} \quad (16)$$

The remaining two rows of matrix \mathbf{G} are obtained from the first two by the substitution of b by a . To obtain nontrivial eigensolutions ξ , the characteristic equation should be

$$\det |\mathbf{G}| = 0. \quad (17)$$

The roots of this equation system can be found numerically, using Newton-Raphson method [15].

2.2.4 Properties of the modes

The wave field structure in the pipe is characterized by its displacement and stress components as well as field variation in the direction of propagation described by the wave number. Following expressions (9) and (13), the arbitrary axi-symmetric longitudinal mode can be described in a vectorial form

$$\begin{aligned} \vec{u}(r, z, t) &= \vec{u}(r) e^{i(\xi z - \omega t)}, \\ \sigma(r, z, t) &= \sigma(r) e^{i(\xi z - \omega t)}, \end{aligned} \quad (18)$$

from which it can be seen that the behaviour of radial $\vec{u}(r)$, $\sigma(r)$ and axial $e^{i(\xi z)}$ can be analyzed separately.

In general, the solution ξ of the dispersion equation (17) can be real or complex, having the real part ξ_{re} and imaginary part ξ_{im} . Separating the real and imaginary

parts in expressions (18), we can get

$$\begin{aligned}\vec{u}(r, z, t) &= \vec{u}(r)e^{i(\xi_{re}z - \omega t)}e^{-\xi_{im}z}, \\ \sigma(r, z, t) &= \sigma(r)e^{i(\xi_{re}z - \omega t)}e^{-\xi_{im}z}.\end{aligned}\tag{19}$$

By the value of ξ it is possible to separate the modes into three families:

- propagating modes ($\xi_{re} \neq 0, \xi_{im} = 0$);
- nonpropagating modes ($\xi_{re} = 0, \xi_{im} \neq 0$);
- inhomogeneous modes ($\xi_{re} \neq 0, \xi_{im} \neq 0$).

Physically, propagating modes do not attenuate in the direction of propagation. Non-propagating modes attenuate without spacial oscillation and inhomogeneous modes attenuate while propagating. Therefore, only propagating modes are of interest in long range inspection as they can transport information without attenuation. However, in the scattering problems they solely cannot describe the wave field around the scatterer. The boundary value problem of the interaction can be treated properly only in co-existence with all three wave mode families.

Fig. 3 represents a typical plot of wave numbers ξ for various propagating, non-propagating and inhomogeneous modes as a function of frequency-thickness product fd in the pipe. The material properties for the aluminium pipe are given in Table. 1. The propagating modes are labelled as $L(0, 1), L(0, 2), \dots$ after Silk *et. al* [16]. The nonpropagating and inhomogeneous modes with complex wave numbers are denoted as C_0, C_1, C_2, \dots and their spatial attenuation along the propagation path is characterized by its imaginary part ξ_{im} . The behavior of these modes is very similar to Lamb modes in a plate, except in the region of low frequency where the mode with a long wavelength is curvature dependent. This is shown in Fig. 4, where the deviation of the lower order pipe modes $L(0, 1)$ and $L(0, 2)$ from Lamb modes A_0 (flexural mode) and S_0 (membrane mode) can be seen. The curve of the mode $L(0, 1)$ slowly separates from Lamb mode A_0 as the fd product decreases, and finally tends towards S_0 mode, but these two curves remain separate as can be seen later. Mode $L(0, 2)$, which is similar to S_0 mode in plate, vanishes below the cutoff frequency $fd \approx 0.21$ MHz-mm and the complex branch C_0 appears. This mode does not appear in the plate. The effect of the curvature increases as the curvature radius decreases. This is shown in Fig.5 where the phase velocity ($c_{ph} = \omega/\xi_{re}$) curves are presented for different thicknesses to middle radius ratio Δ , defined as

$$\Delta = d/R_0, (R_0 = a + d/2),\tag{20}$$

so that $\Delta = 2$ in case of a solid cylinder. Here, R_0 is the mean radius of the pipe. For example, the decrease in the inner radius a towards zero of the pipe causes the

bending type mode $L(0, 1)$ to vibrate in the same way as the compressional type mode of a solid cylinder as was also shown by Nishino *et. al* [17].

Wave field components $\vec{u}(r)$, $\sigma(r)$ illustrate how the displacements, stresses or energy of the modes may vary through the thickness of the pipe. In general each mode has its unique mode shape varying across the thickness of the pipe wall, depending also on the frequency and curvature parameter Δ . These effects are shown in Fig. 6 for the mode $L(0, 1)$, where normalized axial and radial displacements as the function of radius are calculated. A normalized amplitude is the ratio of the desired displacement amplitude to the largest amplitude of the displacement. It can be seen in Fig. 6(a) that the symmetry and antisymmetry of the displacement components about the mid-thickness surface of the pipe wall is inherent to a pipe with a ratio between a small and large radius as it is intrinsic to plate Lamb modes. On the other hand, Fig. 6(b) shows that it does not hold true for thick-walled pipes. The symmetry and antisymmetry of the displacement field is destroyed and, for example, $L(0, 1)$ mode becomes a compressional wave at $fd = 0.3\text{MHz}\cdot\text{mm}$. Fig. 7 illustrates the displacement and stress components of complex modes C_0 , C_3 and C_6 . A normalized amplitude is the ratio of desired stress amplitude to the largest amplitude of stress. It can be seen that the wave field of higher order modes is characterized by increasing variation across the thickness of the pipe's wall.

All the results with real modes were validated using the commercial software package DISPERSE [18].

Table 1. Material and geometric properties of the aluminium pipe used in the study.

a (mm)	d (mm)	ρ (kg/m ³)	c_L (m/s)	c_T (m/s)
7.85	2.2	2765	6440	3113

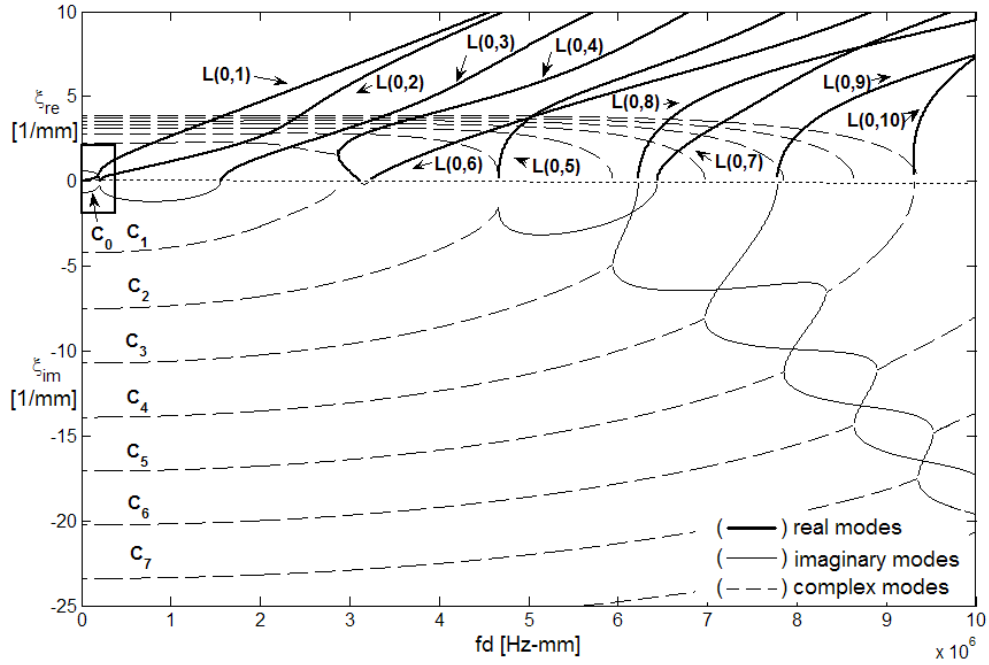


Figure 3. Axial wave number ξ dispersion curves for a pipe. Material properties are given in Table. 1

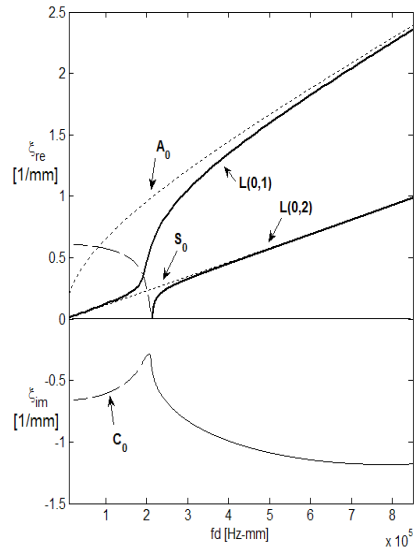


Figure 4. The zoomed area in Fig. 3 at low frequencies showing the difference between the wave numbers ξ of the pipe modes $L(0, 1)$, $L(0, 2)$ and the plate Lamb modes A_0 , S_0 .

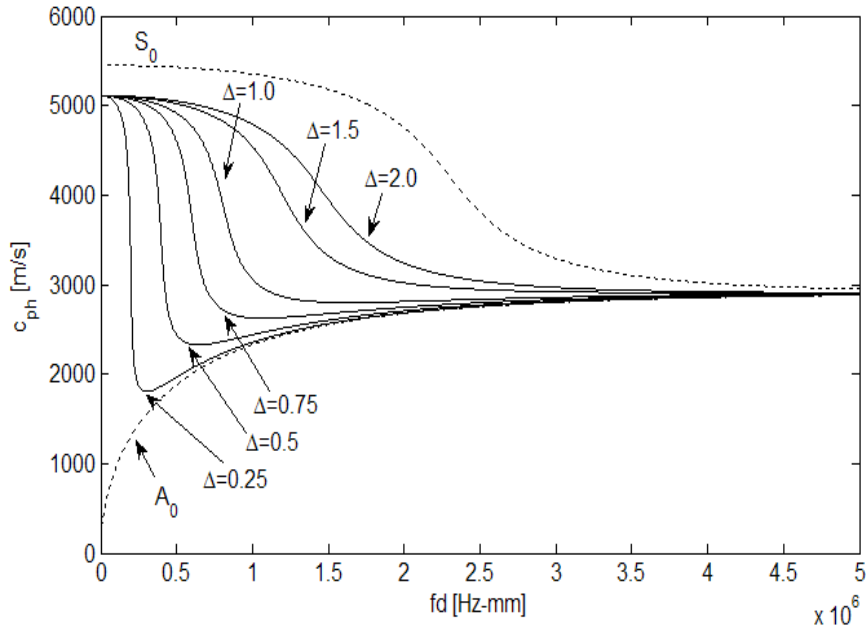


Figure 5. The dependence of phase velocity c_{ph} of the $L(0, 1)$ mode on the curvature parameter Δ .

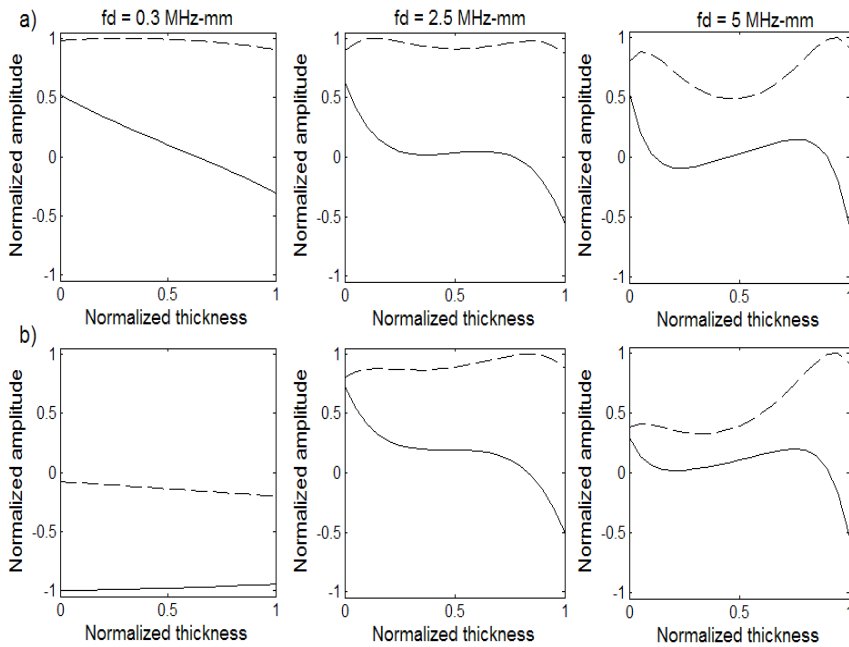


Figure 6. Axial u_z (solid line) and radial u_r (dashed line) displacements of the $L(0, 1)$ mode. a) $\Delta \approx 0.25$; b) $\Delta = 1$.

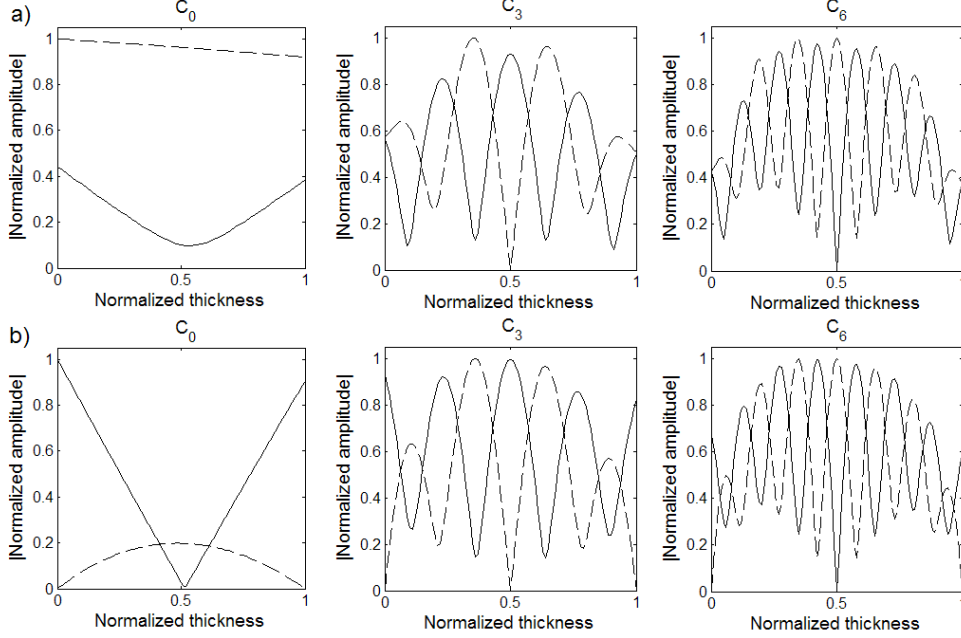


Figure 7. a) modulus of normalized axial u_z (solid line) and radial u_r (dashed line) displacements of the complex modes, b) modulus of normalized stresses σ_{zz} (solid line) and σ_{rz} (dashed line); $\Delta \approx 0.25$ and $fd = 0.1\text{MHz}\cdot\text{mm}$.

2.3 Description of the NME method

2.3.1 Solving the boundary value problem

In a NME analysis, any acoustic field can be developed as a sum of eigenmodes of the structure. Ditre *et. al* [19] showed that the modes of the hollow cylinder form a complete and orthogonal set, which allows them to be used in wave field expansions.

Let us consider an incident wave in Fig. 8 propagating in the z-direction in the pipe wall and interacting with the void type discontinuity. Due to material changes in the waveguide, reflected and transmitted waves occur. The total displacement and stress field, \vec{u}_{tot} and σ_{tot} at the discontinuity can be considered as the sum of incident, reflected and transmitted wave fields

$$\begin{aligned}\vec{u}_{tot} &= \vec{u}_{inc} + \vec{u}_{refl} + \vec{u}_{trans}, \\ \sigma_{tot} &= \sigma_{inc} + \sigma_{refl} + \sigma_{trans}.\end{aligned}\tag{21}$$

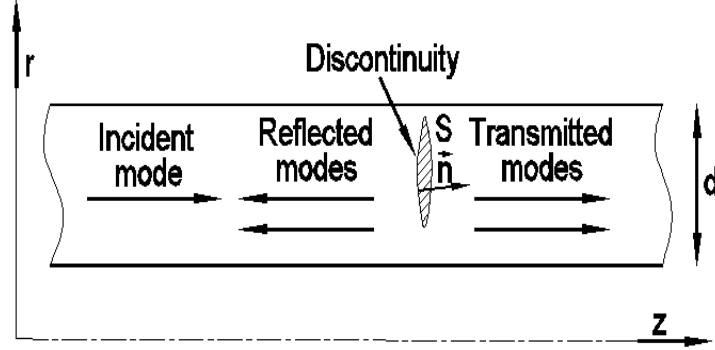


Figure 8. Formulation of the scattering problem for axi-symmetric longitudinal waves in the wall of the pipe

The scattered wave fields can be developed into an expansion, yielding

$$\begin{aligned}\vec{u}_{tot} &= (c_0 \vec{u}_0)_{inc} + \left(\sum_{i=1}^{\infty} c_i \vec{u}_i \right)_{refl} + \left(\sum_{i=1}^{\infty} d_i \vec{u}_i \right)_{trans}, \\ \sigma_{tot} &= (c_0 \sigma)_{inc} + \left(\sum_{i=1}^{\infty} c_i \sigma_i \right)_{refl} + \left(\sum_{i=1}^{\infty} d_i \sigma_i \right)_{trans},\end{aligned}\quad (22)$$

where $\vec{u}_i = \vec{u}_i(r) e^{i(\xi z - \omega t)}$ and $\sigma_i = \sigma_i(r) e^{i(\xi z - \omega t)}$ are the displacement and stress field for the i th mode and c_i and d_i represent the amplitude of reflected and transmitted waves, respectively. In the expansions, there is a finite number of real propagating and imaginary nonpropagating modes and an infinite number of inhomogeneous modes with complex wave numbers. The reflection and transmission of the modes requires selecting specific imaginary and complex roots, so that the amplitudes of the modes decrease away from the obstacle. Therefore the sign for reflected modes must be taken

$$\begin{cases} -\xi_{re}, & \text{for propagating modes} \\ i\xi_{im}, & \text{for nonpropagating modes} \\ \pm \xi_{re} + i\xi_{im}, & \text{for inhomogeneous modes} \end{cases} \quad (23)$$

and for transmitted modes

$$\begin{cases} \xi_{re}, & \text{for propagating modes} \\ -i\xi_{im}, & \text{for nonpropagating modes} \\ \pm \xi_{re} - i\xi_{im}, & \text{for inhomogeneous modes.} \end{cases} \quad (24)$$

The different coefficients of expansion c_i and d_i could be determined from the boundary conditions: normal traction vanishes on the boundary S and traction and particle

displacements are continuous where the defect is not presented

$$\begin{aligned}
\sigma_{tot} \cdot \vec{n} &= 0 && \text{if } (r, z) \in S \\
(c_0 u_z)_{inc} + (\sum_{i=1}^{\infty} c_i u_{zi})_{refl} &= -(\sum_{i=1}^{\infty} d_i u_{zi})_{trans}, && \text{if } (r, z) \notin S \\
(c_0 \sigma_{rr})_{inc} + (\sum_{i=1}^{\infty} c_i \sigma_{rri})_{refl} &= -(\sum_{i=1}^{\infty} d_i \sigma_{rri})_{trans}, && \text{if } (r, z) \notin S \\
(c_0 \sigma_{rz})_{inc} + (\sum_{i=1}^{\infty} c_i \sigma_{rzi})_{refl} &= -(\sum_{i=1}^{\infty} d_i \sigma_{rzi})_{trans}, && \text{if } (r, z) \notin S \\
(c_0 \sigma_{zz})_{inc} + (\sum_{i=1}^{\infty} c_i \sigma_{zzi})_{refl} &= -(\sum_{i=1}^{\infty} d_i \sigma_{zzi})_{trans}, && \text{if } (r, z) \notin S.
\end{aligned} \tag{25}$$

However, it cannot readily be seen how to calculate the scattering coefficients from this system because of the finite number of boundary conditions and an infinite number of unknown coefficients. This can be done numerically. Truncating the system after a certain mode and applying the boundary conditions in l discrete point on the defect surface and in the plane normal to the pipe surface and containing the defect leads to finding a solution of a linear system of equations

$$\mathbf{M} \cdot \mathbf{X} = \begin{bmatrix} M_{11} & M_{12} & \cdots & M_{1m} \\ M_{21} & M_{22} & \cdots & M_{2m} \\ \vdots & \vdots & \ddots & \vdots \\ M_{l1} & M_{l2} & \cdots & M_{lm} \end{bmatrix} \begin{bmatrix} x_1 \\ x_2 \\ \vdots \\ x_m \end{bmatrix} = \begin{bmatrix} y_1 \\ y_2 \\ \vdots \\ y_m \end{bmatrix} = \mathbf{Y}, \tag{26}$$

where \mathbf{M} consists of displacements and stresses of scattered modes, \mathbf{X} is the vector of unknown scattering coefficients and \mathbf{Y} is the vector for displacements and stresses of the incident mode. There can be used several methods to solve this system. In the case when $l = m$, the usual Gaussian elimination (GE) scheme is applied; when $l \geq m$, the method of least squares (LS) or singular value decomposition (SVD) can be used [15].

2.3.2 Convergence of the solution: conservation of the energy

An energy balance criterion is used to check the validity of the numerical results: the energy carried by the reflected and transmitted propagating modes must be as close as possible to the energy of incident mode. The nonpropagating and inhomogeneous modes do not transport energy in z -direction and therefore all the energy is divided between the propagating modes.

The energy carried by an arbitrary propagating i th mode can be expressed as

$$E_i = c_i c_i^* p_i, \tag{27}$$

where the superscript asterisk means complex conjugate. In this expression, p_i is the acoustic Poynting vector flow, which represents the average power flow over a period

of the i th mode propagating in the z -direction

$$p_i = -\frac{1}{2}Re \left[-i\omega \int_0^{2\pi} \int_a^b (u_{ri}^* \sigma_{rzi} + u_{zi}^* \sigma_{zzi}) d\theta dr \right] \quad (28)$$

The propagating wave energy reflection and transmission coefficient R_i and T_i can be calculated by dividing the energy of the reflected or transmitted wave E_i and E_j , respectively, by the incident wave energy E_0

$$R_i = \frac{E_i}{E_0}, T_j = \frac{E_j}{E_0}. \quad (29)$$

Obviously, the guided wave scattering solutions in this study can be influenced by the inevitable error sources from the NME method scheme: the approximated field variables, the numerical integration, the Gaussian elimination scheme with finite integration points, the discretized boundary with finite boundary nodes, and the finite number of modes used in the mode superposition. The relative error in energy balance ϵ due to approximated solution is

$$\epsilon = \left| 1 - \sum_i R_i - \sum_j T_j \right|. \quad (30)$$

2.4 Example1: edge resonance in a semi-infinite thick pipe

2.4.1 Introduction

In this section the NME method is applied to investigate the interaction of axisymmetric longitudinal L(0,2) mode with the edge of a semi-infinite pipe. The reflection at the edge is one of the simplest cases of guided wave scattering, but it provides insight into its essential features. It helps to understand the role of different wave modes in the scattering processes and also to evaluate the influence of waveguide parameters on the interaction phenomenon.

The studies of Lamb wave interaction with the free edge of the plate [20–25] have shown that the end of the plate is often accompanied by mode conversions and the generation of nonpropagating modes. At certain conditions of the waveguide and the incident mode the vibration of these nonpropagating modes is strongly amplified leading to the edge resonance phenomenon. The behavior of this type of motion has been thoroughly studied both theoretically and experimentally in plates [26–32], solid cylinders [33–37] and rods [38]. In plates it was found that the edge resonance appeared as a result of the superposition of incident and reflected first symmetric Lamb mode S_0 and rapidly attenuating vibration modes that must satisfy the stress-free boundary condition at the end of the plate all at the same time. The first pair of nonpropagating modes caused a remarkable increase in the displacements of the plate end and clearly indicated the resonance phenomenon. Similarly, in solid cylinders at

a specific frequency the symmetric L(0,1) mode caused a strong vibration of low order nonpropagating modes.

However, only a few works deal with the explanation of the resonance phenomenon in pipe-like structures [39, 40]. In these papers the authors used the theory of shells, which restricted the analysis to thin-walled structures. Only Grinchenko [41] has investigated the edge resonance in a thick pipe but in the case when the first longitudinal mode is incident. The aim of this study is to extend the analysis of edge resonance to thick pipes and additionally to investigate the influence of the curvature on axisymmetric longitudinal wave propagation characteristics in a semi-infinite pipe. The influence of the curvature on the excitation of edge mode in the case of incident L(0,2) is thoroughly investigated and the results are compared with the results of the finite element (FE) method. Finally, an experimental determination of edge resonance is made in an aluminium pipe in order to verify the computational predictions.

The experimental work presented in this section was the result of the collaboration between the Department of Mechanics at Tallinn University of Technology and the Laboratoire d'Acoustique Ultrasonore et d'Electronique at the Université du Havre. It resulted in a joint publication [P5].

2.4.2 Modelling procedures

Computation of the reflection at the end of a semi-infinite pipe

Consider a two-dimensional axial cross-section of a semi-infinite pipe wall as shown in Fig. 9. An incident mode L(0,m) propagating in the $z > 0$ direction interacts with the free end of the pipe at $z = 0$. The general boundary problem (25) introduced in Subsection 2.3 can be simplified to a problem where only the normal and shear stress σ_{zz} and σ_{rz} at the edge must vanish

$$\begin{aligned}\sigma_{zz}(r) &= \sum_{i=0}^{\infty} c_i \sigma_{zzi}(r) = 0, \\ \sigma_{rz}(r) &= \sum_{i=0}^{\infty} c_i \sigma_{rzi}(r) = 0.\end{aligned}\tag{31}$$

This system can be solved approximately, setting σ_{zz} and σ_{rz} equal to zero at a fixed number l points along the edge of the pipe, thus forming a system of equations. The l equations are

$$\sigma_{zz}(r_j) = \sum_{i=0}^m c_i \sigma_{zzi}(r_j) = 0 \text{ and } j = 1, 2, \dots, \frac{l+1}{2};\tag{32}$$

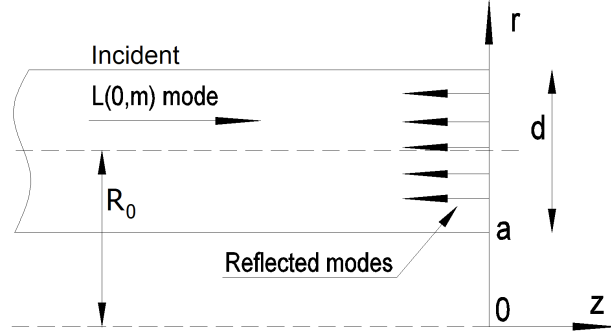


Figure 9. L(0,m) mode reflection at the edge of the pipe wall.

where $r_j = a + \frac{2d(j-1)}{l-1}$ and

$$\sigma_{rz}(r_j) = \sum_{i=0}^m c_i \sigma_{rzi}(r_j) = 0 \text{ and } j = 1, 2, \dots, \frac{l-1}{2}; \quad (33)$$

where $r_j = a + \frac{2dj}{l-1} + \delta$. Here δ is the parameter which allows to change the position of the collocation points for σ_{rz} and is taken always smaller than the step $s = \frac{2dj}{l-1}$.

The energies of the reflected waves are found numerically using the composite Simpson's rule [15] in the integration formula in Poynting vector flow expression (28).

FE modelling

The edge resonance has been successfully studied with the FE method in plates in case of S_0 incidence [29]. A similar study was performed to predict the effect of curvature on edge vibration of the pipe in case of incident L(0,2) mode using the explicit procedure of the program ABAQUS [42]. Due to the axial symmetry of the problem, a two-dimensional region representing a radial-axial section through the pipe was modelled as shown in Fig. 10(a). The thickness of the wall of the pipe was 2.2 mm and the length varied from 250 to 750 mm. The mesh of the pipe consists of four noded linear quadrilateral axi-symmetric elements with 2 degrees of freedom in each node (displacements in r , z directions). These elements satisfactorily describe the motion of axi-symmetric longitudinal pipe modes, as was shown in previous studies [43, 44]. On one side of the pipe the absorbing region [45] is applied to decrease the model size and neglect undesired reflections from the edge. The waves that enter this area are increasingly damped and eventually die out. A number of geometries was set up in order to model the pipes with different thickness to mid-radius ratios

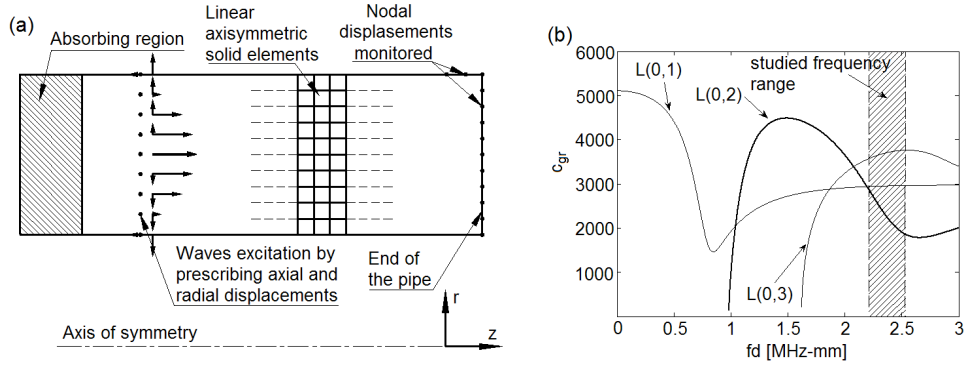


Figure 10. a) FE axi-symmetric model of the pipe; b) group velocity dispersion curves for axi-symmetric longitudinal modes propagating in an aluminium pipe, $\Delta = 1.0$.

Δ . The thickness of the pipe always remained the same; only the position of the axis was modified to model the pipe with the desired radius. The pipes with the following geometries were studied: $\Delta = d/R_0 = 0.25; 0.5; 0.75$ and 1 . In each model the density of the mesh was also changed according to the wavelength of propagating modes. At least 15 elements per wavelength were used, that is more than the lower limit of spatial discretization of 8 elements per wavelength for accurate modeling. A summary of the FE models that were used in the study can be found in Table. 2. The signal was generated 20 mm away from the edge of the pipe where the absorbing region was applied. The excitation of the L(0,2) mode was achieved by "center mode shape" excitation technique [46] which is used for pure mode generation in a non-dispersive regime. The desired mode in the FE model was generated by scaling the tone bursts applied to each node through thickness according to the amplitude of displacement at that location in the exact mode shape profile at a center frequency of excitation. However, the group velocity curves in Fig. 10(b) show that it is not possible to generate an entirely pure mode with this technique because over the investigated frequency bandwidth the excited mode L(0,2) is dispersive and the other

Table 2. Summary of FE models used in the study.

Δ	Length (mm)	Element through thickness	Tone burst (cycles)
0.25	250	15	20
0.5	350	15	40
0.75	450	20	50
1.0	750	20	60

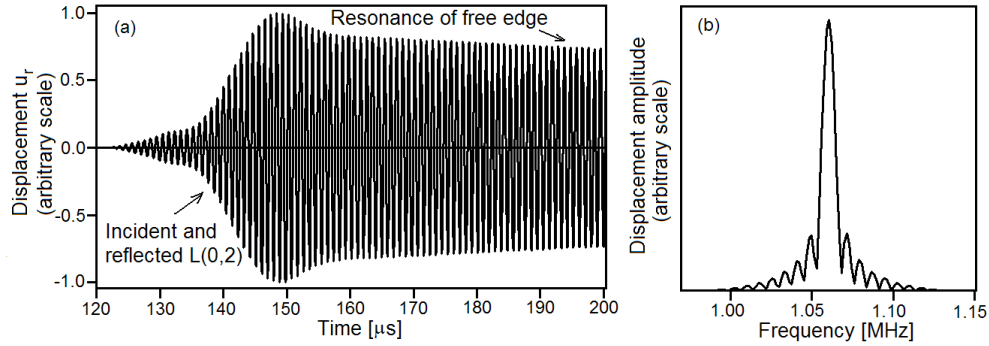


Figure 11. a) Typical time record showing the edge resonance in case of L(0,2); center frequency-thickness product is 2.335 MHz-mm; $\Delta=0.25$. b) Frequency spectrum of the resonance part of the signal shown in a).

lower order axisymmetric modes L(0,1) and L(0,3) are also generated. To avoid any other modes interfering with the results a sufficiently long propagation distance was chosen to make the signals separable in time domain.

In each pipe model a different tone burst was used. The narrow band signals consisting of a tone burst multiplied by sinusoid window containing 20, 40, 50 and 60 cycles centered at resonance frequency were used for the excitation. The higher number of cycles was used in models where the wave propagation distance was longer and reduction of distortion of the wave packet was needed. The resonance of the edge was supposed to be excited at a specific frequency in the frequency spectrum of the excitation. The rough estimation of this frequency was achieved by using the numerical modeling results and the calculation was repeated with adjusted frequency. The results of the simulations were obtained by monitoring nodal displacements at the free edge and close to the edge on the surface of the pipe. Both radial and axial displacement components were monitored to describe the edge mode. An illustrative time record of radial displacement of the outer corner of the edge measured at resonance frequency is plotted in Fig. 11(a), showing permanent high amplitude vibration of the edge. The resonance frequency was measured as that corresponding to maximum value from the frequency spectrum, shown in Fig. 11(b).

2.4.3 Experimental setup

The experimental set-up is described in Fig. 12. Measurements were performed on aluminium pipe of 230 mm length, with an inner radius of 7.85 mm and a wall thickness of 2.2 ± 0.1 mm ($\Delta = 0.25$). The pipe was vertically posed to the transducer.

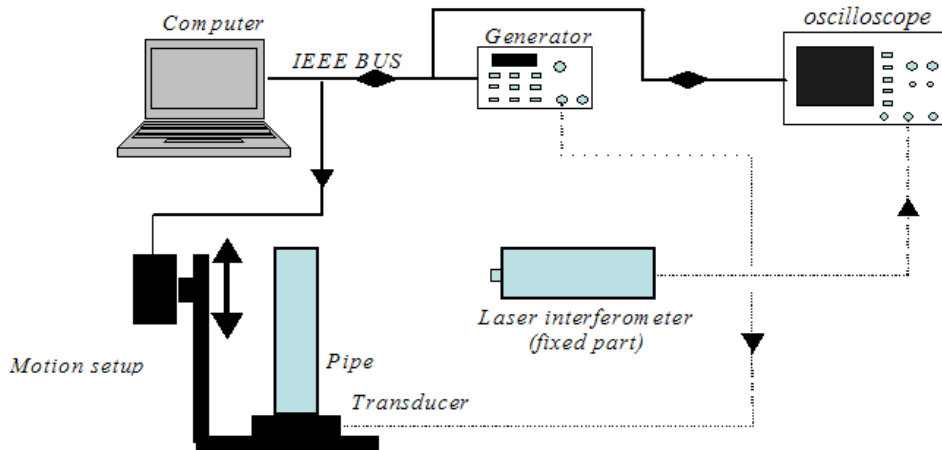


Figure 12. Scheme of the experimental setup.

Metalscan gel layer was used to ensure a good ultrasound coupling. The set is vertically mobile by means of a motion setup, which allows measuring the displacement from different positions on the pipe surface.

Excitation of the $L(0,2)$ mode was achieved using the broadband piezoelectric transducer (Panametrics V401) with a central frequency of 1MHz. The transducer was excited using a narrow band signal consisting of a tone burst multiplied by sinusoid window containing 20 cycles using the signal generator (3314 Generator). The detection of the signal was achieved using a laser interferometer (BMI heterodyne probe SH140) to measure the normal displacement on the surface of the tube. The measurements were taken at a series of equally spaced positions along the pipe from 0.1 to 16.7 mm with the step 0.1 mm at the upper end. The measured signals by the laser interferometer were averaged (sweep average: 200) and displayed on a digital oscilloscope. Thereafter the obtained signal was recorded on a computer via the IEEE bus in order to reveal the numerical treatments. This computer also allowed us to drive and to control the motion of the pipe.

2.4.4 Results and discussion

Reflection of $L(0,2)$ mode by a free end: validation of analytical calculations

From previous research with plates [26] it is well known that the edge resonance is produced by Lamb mode S_0 at a particular frequency and is due to the high amplitude standing waves raised by complex modes at the end of the plate. In the previous

section it was shown that the propagation of L(0,2) mode in a thin-walled pipe is similar to Lamb mode S_0 propagation in a plate. It means that the behavior of the reflection of L(0,2) mode at the edge must be analogous. This is shown in Fig. 13, where the reflection ratio of this mode is observed as a function of frequency. A similar incident energy transformation into energies of higher order modes is seen, and was observed in the plate by Gregory et al [47]. Plate results are shown by dots, which fit the curves very well corresponding to the pipe results. Therefore it can be expected that the edge resonance in thin-walled pipe appears at the same frequency and is mainly due to the oscillation of the first complex mode C_1 . This statement is confirmed in Fig. 14, where the displacement amplitudes of this mode clearly exceed those of the incident wave and other higher order complex modes near the resonance frequency $fd = 2.317$ MHz-mm. Again there is a good agreement with the previous results of Wilkie-Chancellor *et. al* [30]. The accuracy of the numerical results was estimated by the concept of energy conservation and the relative error ϵ was found to be less than 5%.

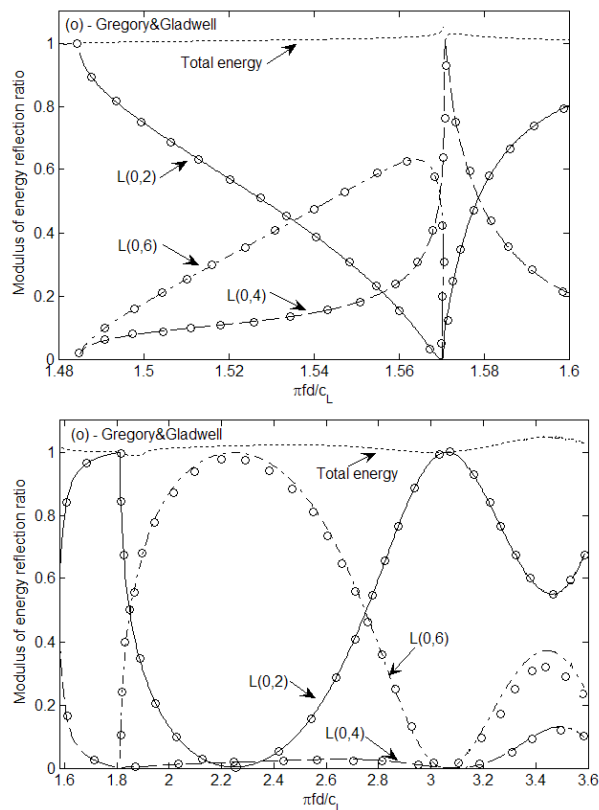


Figure 13. Reflection of L(0,2) mode at a pipe edge. The parameters of the pipe: $a = 40$ mm, $d = 1$ mm, $\Delta = 0.025$, $\rho = 7800$ kg/m³, $c_L = 1000$ m/s, $c_T = 577.4$ m/s.

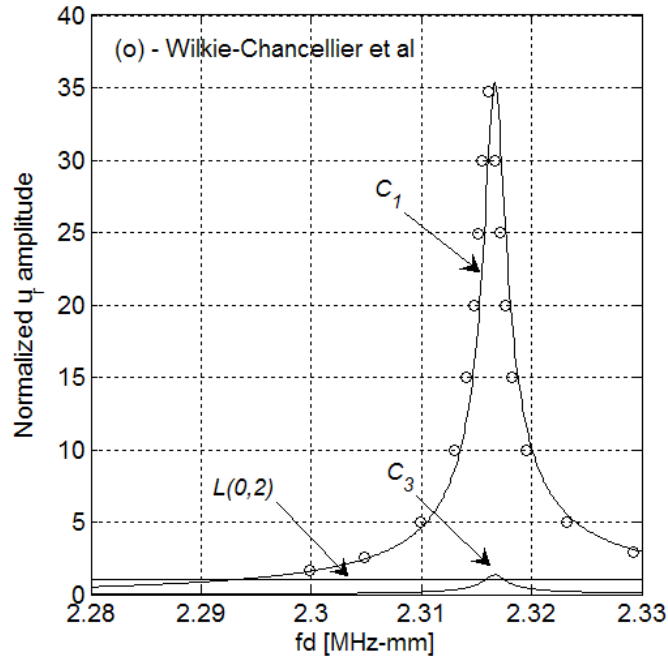


Figure 14. Normalized displacement u_r amplitudes of reflected modes at the edge of the pipe. The parameters of the pipe: $a = 40$ mm, $d = 1$ mm, $\Delta = 0.025$, $\rho = 7800$ kg/m³, $c_L = 5850$ m/s, $c_T = 3150$ m/s.

Experimental detection of the edge resonance

Due to the spread in thickness of the pipe, an effort should be made to determine the frequency of the edge resonance accurately. Initially, a resonance spectrum was measured at 0.1 mm from the upper end of the pipe in the frequency-thickness product range 2.2-2.53 MHz-mm with a step of 0.011 MHz-mm. Fig. 15(a) shows the variation of the amplitude for the normal surface displacement u_r depending on the fd . The edge resonance frequency was determined at the maximum of the measured magnitude of the resonance spectrum at $fd = 2.435$ MHz-mm. This value differs from the theoretically obtained result $fd = 2.336$ MHz-mm. However, the non-uniform thickness of the pipe used in the test allows for expanding the resonance frequency range to $fd = (2.324, 2.565)$ MHz-mm. Thereafter the spatiotemporal representation at the resonance frequency was performed as shown in Fig. 15(b). Here it is clearly seen that after the reflection of the incident mode with the end (140 s), the edge remains vibrating at a high amplitude, which is the resonance behavior. Fig. 16 shows the time domain record measured at 0.1 mm from the pipe edge. The long tail due to edge resonance can be clearly seen in this plot.

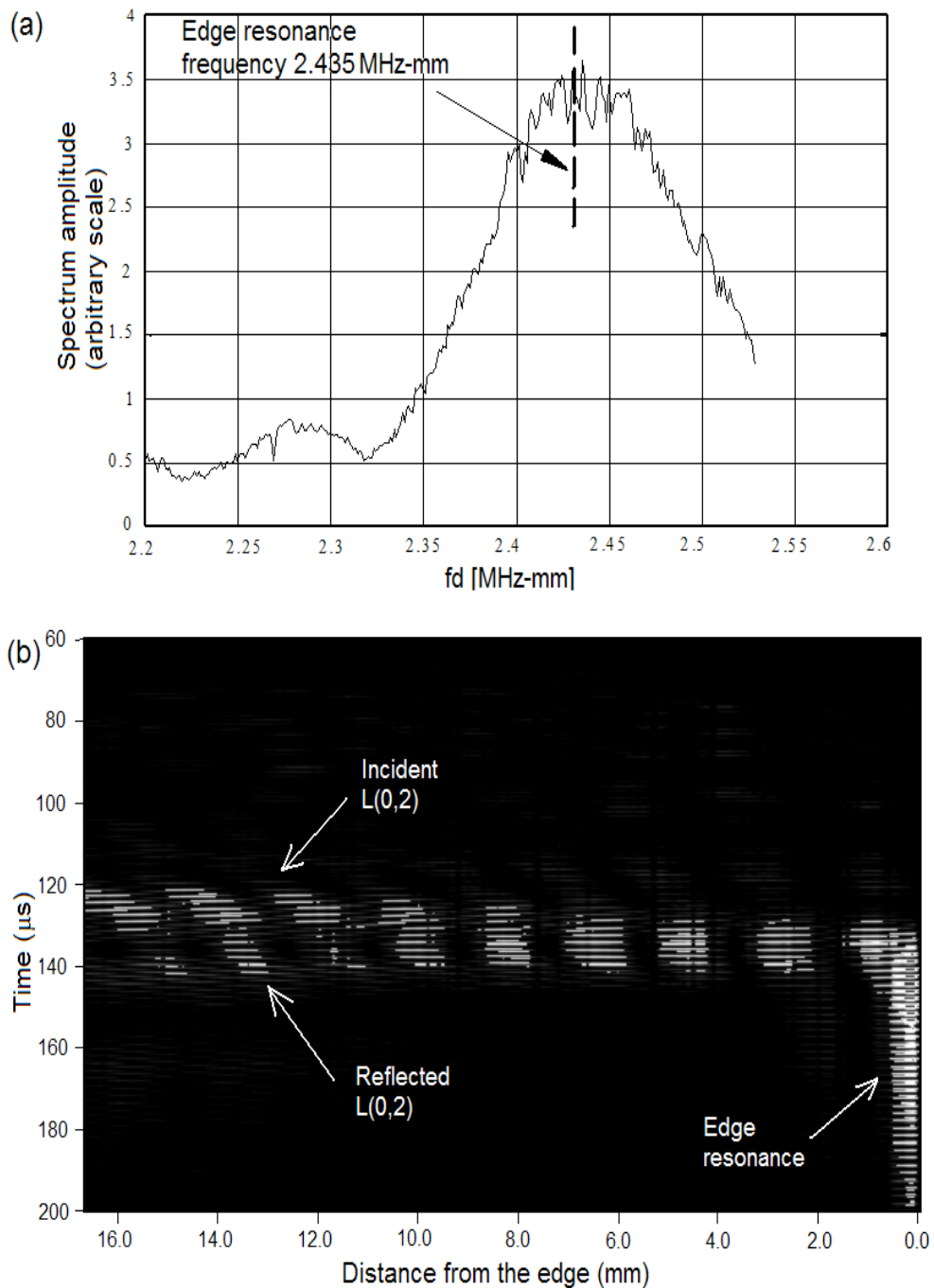


Figure 15. a) Resonance spectrum of normal displacement of L(0,2) mode measured at 0.1 mm from the pipe end. b) Contour plot of measured normal displacements in time and space domain showing the generation of edge resonance.

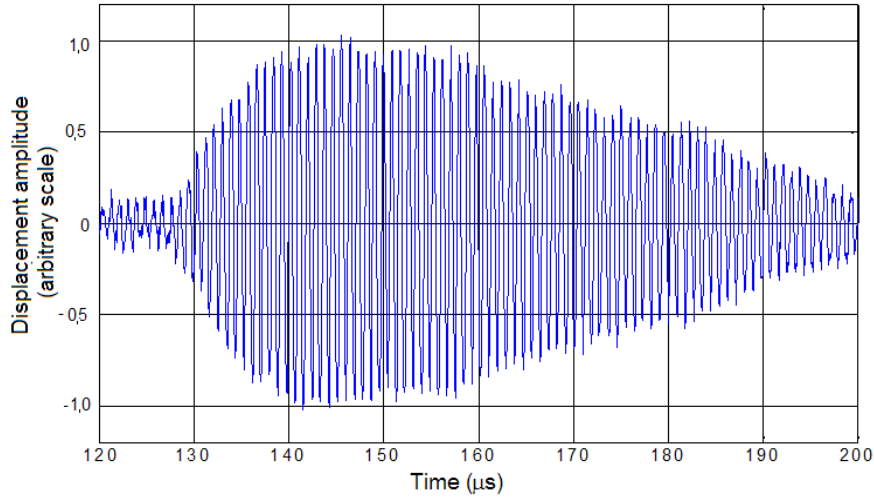


Figure 16. Normal surface displacement u_r , time record at 0.1 mm from the pipe end at $fd = 2.435$ MHz-mm.

Influence of the curvature on the edge resonance. Mode conversion

The variation of the curvature parameter Δ strongly affects the interaction of L(0,2) mode with the end of the pipe and the generation mechanism of the edge resonance. The edge resonance can be found at a maximum displacement amplitude value of complex mode C_1 versus frequency-thickness product fd . An illustrative calculation was performed for the pipes with a curvature parameter $\Delta = 0.25; 0.5; 0.75; 1.0$, as shown in Fig. 17, where the normalized radial displacement amplitude of C_1 at the edge is shown as a function of fd . A normalized amplitude is the ratio of the largest amplitude of complex mode to the largest amplitude of the L(0,2) incident wave anywhere in the thickness of the pipe wall. As can be seen from the figure, the amplitude of the complex mode drops when the parameter increases and the peaks move towards a higher fd . This behavior can be explained by the increasing difference of the inner and outer radii in a thick pipe, by which the symmetry is broken. The agreement between numerical approaches GE and LS is very good. The edge resonance frequencies obtained with the analytical and FE model are shown in Table. 3. The frequency values obtained by the FE method tend to be always smaller than by the numerical model.

To see the extent of the edge resonance along the pipe, the radial displacement of outer surface near the end for the two different pipes $\Delta = 0.25; 0.75$ is calculated by the finite element model and by the analytical approach, shown in Fig. 18. The finite element data represent the amplitudes of the displacements measured in the frequency domain at a resonance frequency. A rapid decrease in amplitudes of the

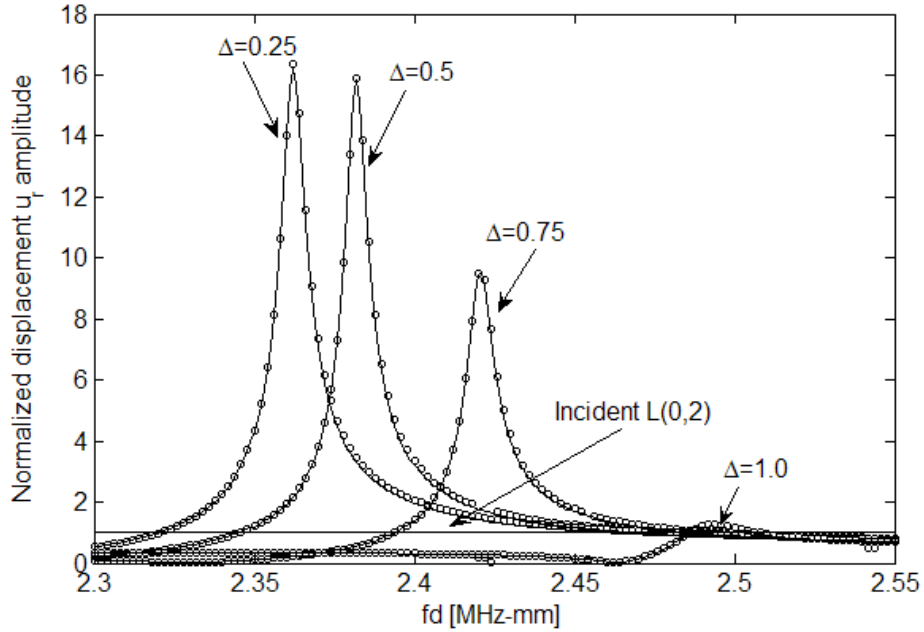


Figure 17. Normalized radial displacement u_r amplitudes of reflected modes at the edge of the pipe as a function of curvature parameter Δ . (—) GE, (o o o) LS.

total displacement field is seen moving away from the edge. There is good agreement between the results obtained using these two methods.

The variation of the curvature parameter also changes the through-thickness displacement variations of the edge. Normalized axial and radial displacement at the resonance frequencies are shown in Fig. 19 for the pipes with a curvature parameter $\Delta = 0.25; 0.75; 1.0$. The axial displacement of the pipe edge ($\Delta = 0.25$) is nearly symmetric to the mid-surface of the pipe wall, which is similar to the plate case. However, when the curvature parameter Δ increases, this symmetry is broken and the inner surface of the pipe vibrates more intensively than the outer surface.

Table 3. Predicted edge resonance frequencies by numerical and FE model

Δ	fd_{num} (MHz-mm)	fd_{FE} (MHz-mm)
0.25	2.362	2.335
0.5	2.382	2.352
0.75	2.420	2.400
1.0	2.493	2.468

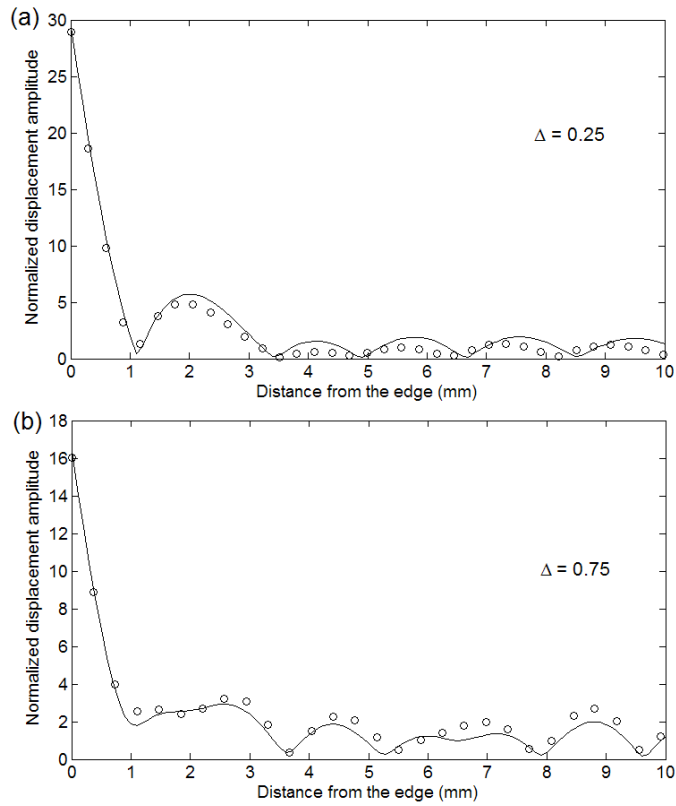


Figure 18. The normal displacement component of the total displacement field at the outer surface of the pipe measured as the function of the distance near the edge at resonance frequency. (—) analytical model, (o o o) FE predictions. The results have been normalized by the outer surface radial displacement amplitude of the incident mode.

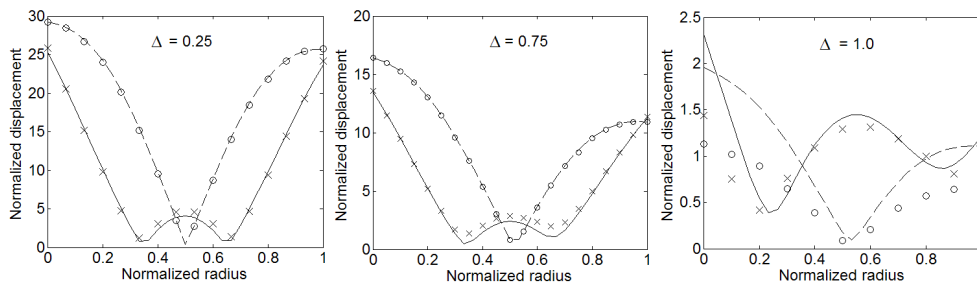


Figure 19. Through-thickness mode shapes of the edge at resonance frequencies for different pipes $\Delta = 0.25; 0.75; 1.0$. Numerical predictions u_r (dashed line), u_z (solid line); FE predictions u_r (o o o), u_z (x x x). The extremities of the normalized radius scale represent the inner and outer radii of the pipe.

It is also interesting to observe the energy balance at the edge of the pipe as a function of the curvature parameter Δ . In Fig. 20 it can be seen that when Δ is close to zero (a very thin shell or plate), the energy is entirely reflected into the L(0,2) mode. This is also true for big curvature parameter values ($\Delta = 2$ for a solid cylinder). Between these extreme values of Δ , reflection of the L(0,2) mode generates antisymmetric type modes L(0,1) and L(0,3). The energy ratio of L(0,2) mode is reduced to zero at $\Delta = 0.667$ (pipe thickness nearly equal to its inner radius), where the reflected energy is completely transferred into L(0,1) and L(0,3) modes at the resonance frequency, as seen in Fig. 21, where energy balance of modes versus fd product is presented.

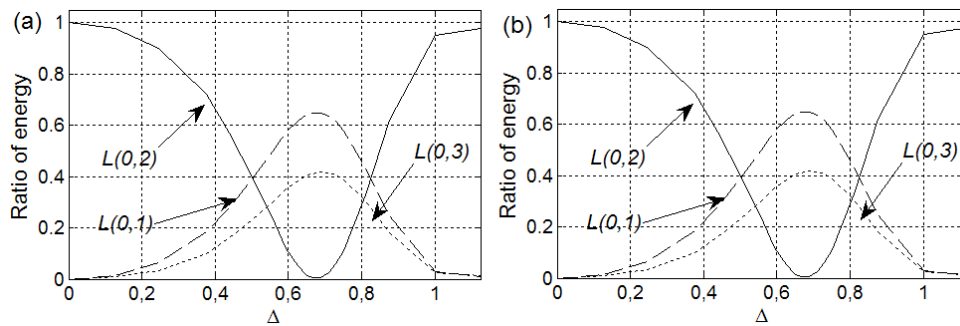


Figure 20. Energy balance of the L(0,2) mode as the function of curvature parameter Δ . a) The energies for the modes have been obtained at resonance frequencies. b) All energies have been calculated at $fd = 2.405$ MHz-mm.

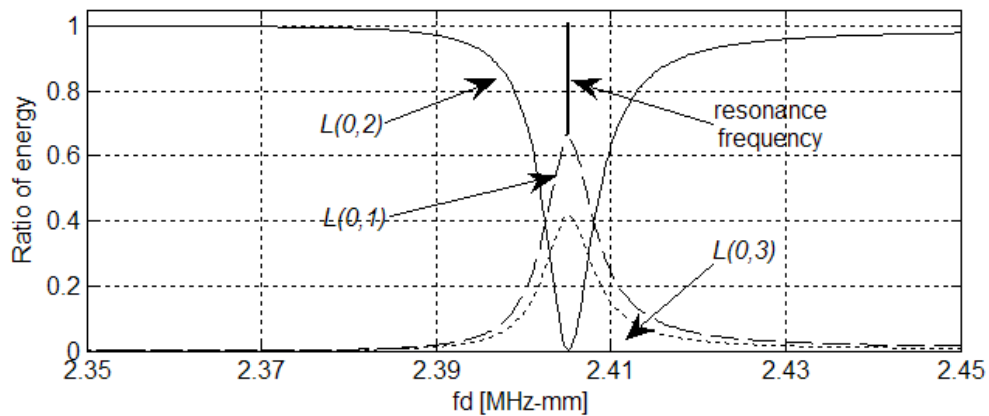


Figure 21. Energy balance of the L(0,2) mode as the function of frequency-thickness fd for the pipe of $\Delta = 0.667$.

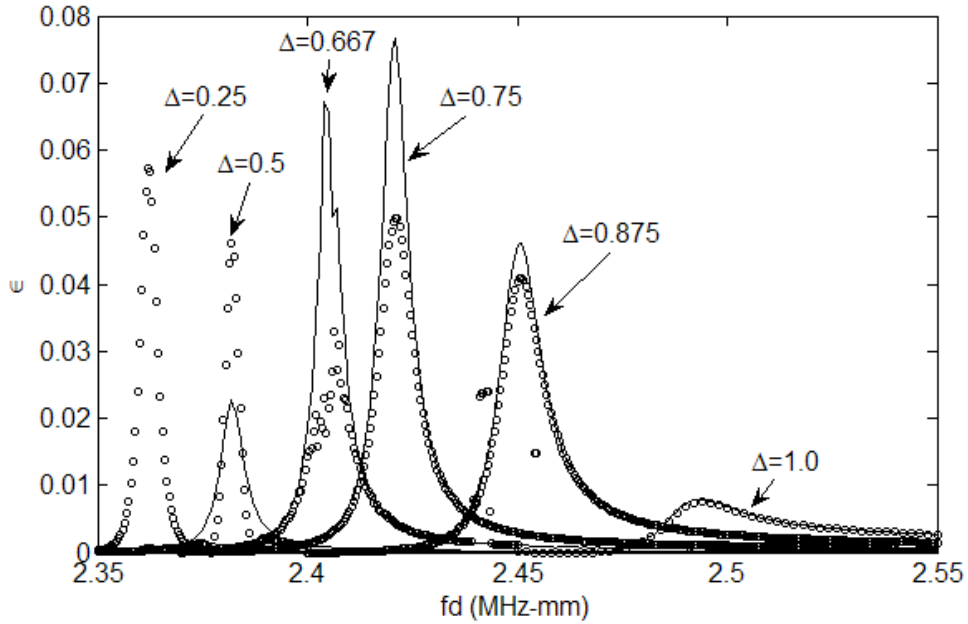


Figure 22. Relative error ϵ in energy balance of the propagating modes as the function of frequency-thickness product fd and curvature parameter Δ ; $\delta = 0$. (—) GE, (o o o) LS.

The relative error ϵ is calculated to evaluate the energy balance criterion. 60 modes were used in the expansion and both numerical approaches Gaussian elimination scheme (GE) ($m = 59, l = 59$) and least squares (LQ) ($m = 59, l = 185$) were implemented. In Fig. 22 it is seen that the largest errors for different Δ appear around the edge resonance frequencies and, for example, GE gives the biggest error $\epsilon = 0.077$ at $\Delta = 0.75$. The convergence of these two methods is different and depends on the number of modes in the expansion as seen in Fig 23(a). This example shows that although the relative error ϵ for LS is less than 0.05, after 100 modes it converges and is the same as in GE 0.077. Similar converging behaviour of ϵ was also observed for other values of Δ but for brevity is not shown here. Another variable that can influence the solution is the parameter δ which allows to change the position of the collocation points along the edge of the pipe wall. Fig 23(b) shows how the error ϵ varies when the positions of the collocation points are changed around its initial point. In general, both approaches are stable to the variation of δ , however, the GE approach is more sensitive to the change whilst some values of the error deflect largely from its stable values.

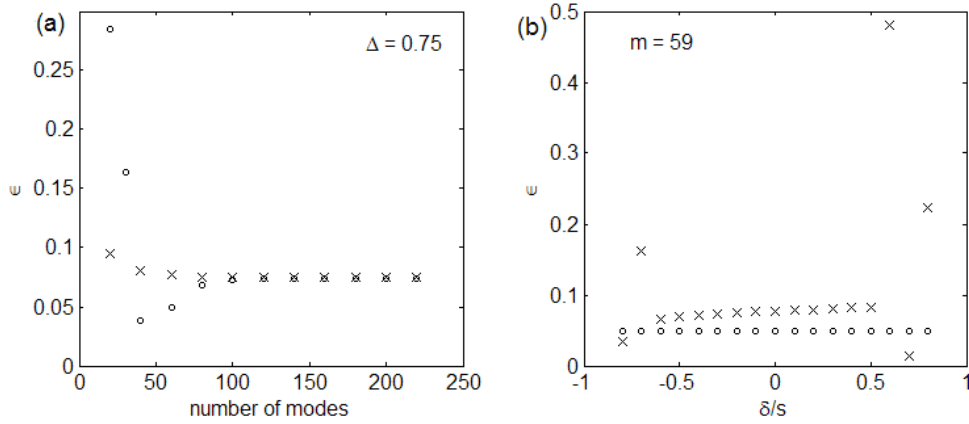


Figure 23. Relative error ϵ in energy balance of the propagating modes as the function of number of modes (a) and the parameter δ/s which controls the position of collocation points (b) at $fd = 2.42$ MHz-mm. (x x x) GE, (o o o) LQ.

2.5 Example 2: wave interaction with a vertical part-through crack in a thick pipe

2.5.1 Introduction

In this section the NME method is applied to investigate the axi-symmetric longitudinal L(0,2) mode interaction with a vertical zero-width crack in the wall of the pipe. The scattering analysis helps to understand how the depth of the crack and the curvature of the pipe influence the scattering process.

An extensive amount of literature has been published on guided wave interaction with crack type features in plate [4, 5, 12, 48–57] and pipe structures [1, 43, 44, 58–65] and only some of them are named here. The experimental and FE modelling study of longitudinal wave scattering at circumferential through and part-through crack was reported by Alleyne and Lowe [43, 44]. They showed that when L(0,2) mode is incident at the notch, the reflected energy is divided between axi-symmetric and nonaxi-symmetric modes, which intensity depends on the circumferential extent and depth of the defect. Later, Bai *et. al* [62] used a three-dimensional numerical wave field expansion technique to validate their results. However, these works did not investigate wave scattering problems in thick pipes. As we saw in the previous section, in the thick pipe the curvature affects wave interaction with discontinuities. Therefore, it is important to study how this influence manifests on wave scattering at cracks.

Here we study a simple axi-symmetric model with a full circumferential extent surface crack that allows to reduce the problem into a two-dimensional problem with

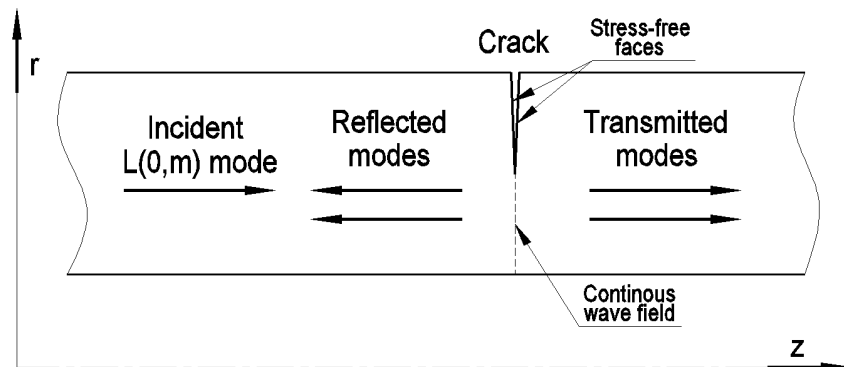


Figure 24. $L(0,m)$ mode scattering at the surface crack in the wall of the pipe.

the assumption of plane strain. Two types of cracks are considered in this study: a) an outer and b) an inner surface crack. The frequency-thickness of the propagating mode is chosen 1.3 MHz-mm, which is below the cut-off frequencies of the $L(0,3)$ and $L(0,4)$ mode. The reflection and transmission coefficients are measured for $L(0,1)$ and $L(0,2)$ modes (due to mode conversion) as the function of the depth of the crack for pipes with different curvature parameter. The difference between the scattering at outer and inner surface crack is investigated. The results are compared with the results of the FE method and the other ones found in literature.

2.5.2 Modelling procedures

Computation of the reflection and transmission at the vertical crack in the wall of the pipe

The present NME technique allows to solve only two-dimensional wave scattering problems. Therefore, this study is limited to treat the $L(0,m)$ mode interaction with the crack, which is circumferential and perpendicular to the axis of the pipe. Then the problem is axi-symmetric and the scattering can be analyzed in a two-dimensional axial cross-section of the pipe as shown in Fig. 24. The normal and shear stress at the crack faces must vanish and, additionally, the continuity of the wave field in the remaining part of the wall must be satisfied:

Stress-free left surface of crack:

$$\begin{aligned}\sigma_{zz}(r) &= \sum_{i=0}^k c_i \sigma_{zzi}(r) = 0, \\ \sigma_{rz}(r) &= \sum_{i=0}^k c_i \sigma_{rzi}(r) = 0;\end{aligned}\tag{34}$$

Stress-free right surface of crack:

$$\begin{aligned}\sigma_{zz}(r) &= \sum_{i=1}^{m-k} d_i \sigma_{zzi}(r) = 0, \\ \sigma_{rz}(r) &= \sum_{i=1}^{m-k} d_i \sigma_{rzi}(r) = 0;\end{aligned}\tag{35}$$

Displacement continuity out of crack:

$$\sum_{i=0}^k c_i u_{zi}(r) - \sum_{i=1}^{m-k} d_i u_{zi}(r) = 0;\tag{36}$$

Stress continuity out of crack:

$$\begin{aligned}\sum_{i=0}^k c_i \sigma_{zzi}(r) - \sum_{i=1}^{m-k} d_i \sigma_{zzi}(r) &= 0, \\ \sum_{i=0}^k c_i \sigma_{rzi}(r) - \sum_{i=1}^{m-k} d_i \sigma_{rzi}(r) &= 0, \\ \sum_{i=0}^k c_i \sigma_{rri}(r) - \sum_{i=1}^{m-k} d_i \sigma_{rri}(r) &= 0.\end{aligned}\tag{37}$$

When the system is correctly solved, the complex displacement field at the crack location is computed in the following equations:

To the left of the crack:

$$u(r, z^{\text{crack left}}) = \sum_{i=0}^k c_i u_i(r),\tag{38}$$

To the right of the crack:

$$u(r, z^{\text{crack right}}) = \sum_{i=1}^{m-k} d_i u_i(r).\tag{39}$$

The reflection and transmission coefficients can be given in the form

$$R_i^* = \left| \frac{c_i u_{kj}(r = a, b)}{c_0 u_{0j}(r = a, b)} \right|, \quad (40)$$

$$T_i^* = \left| \frac{d_i u_{kj}(r = a, b)}{c_0 u_{0j}(r = a, b)} \right|,$$

where i represents the mode and $j = r$ or z .

FE study

Similar FE procedures were performed as introduced in Section 2.4.2 to understand the scattering phenomenon at the crack in the wall of the pipe. The modelled pipe wall was 1.92 m long consisting of axi-symmetric square shape elements as shown in Fig. 25. 8 elements were used through the thickness of the 2.2 mm pipe wall which was more than 15 elements per incident wavelength. Both sides of the pipe were surrounded by absorbing type of elements that help to remove unwanted reflections at the edges. A number of geometries were set up in order to model the pipes with a different thickness to mid-radius ratios Δ . The pipes with the following geometries were studied: $\Delta = 0.25$ and 1. A zero-width crack was created in the middle of the pipe length by disconnecting the nodes at the place of the crack and it ran perpendicularly in the surface of the wall of the pipe. The disconnected nodes that have the same position move independently. That means there is no transfer of stresses and displacements between them. The depths of the crack were varied from $p = 12.5; 25; 37.5; 50; 62.5; 75$ to 87.5% of the thickness of the wall.

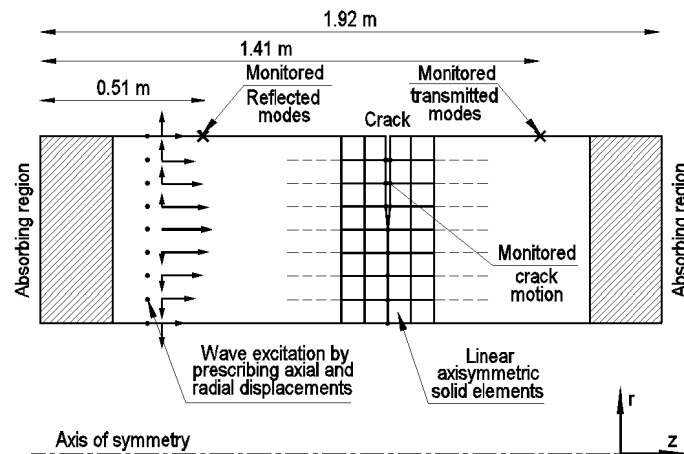


Figure 25. FE axi-symmetric model of the pipe with a surface crack.

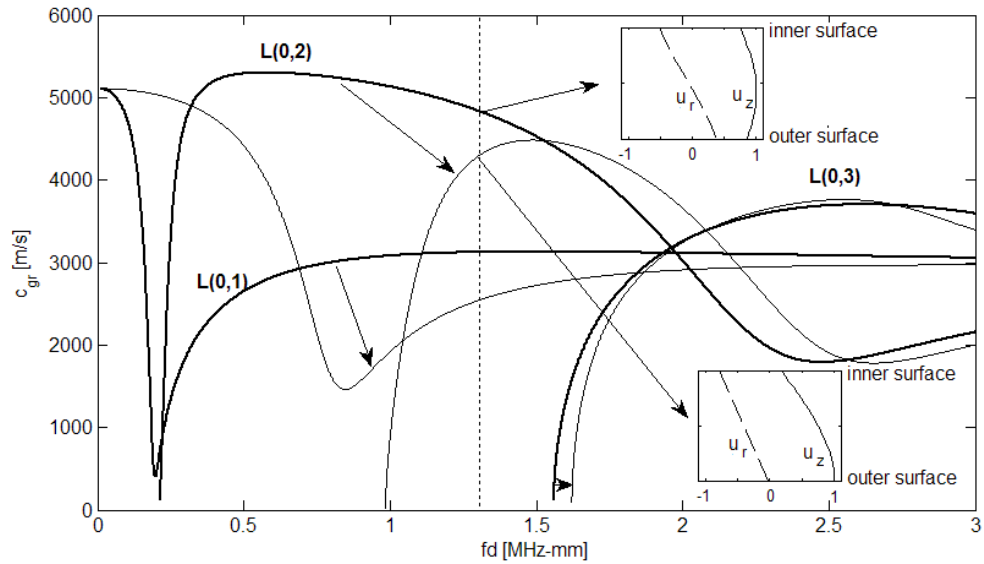


Figure 26. Group velocity dispersion curves and some mode shapes for axi-symmetric longitudinal modes with the pipe curvature $\Delta = 0.25$ (thick solid line) and $\Delta = 1$ (solid line).

The signal was generated 60 mm away from one edge using the center mode shape excitation. A Hanning windowed tone burst containing 30 cycles at a center frequency 590.9 kHz ($fd = 1.3$ MHz-mm) was used as the excitation signal. The dispersive characteristics and mode behaviour are shown in Fig. 26. The results of the simulations were obtained by monitoring nodal displacements at the outer surface of the pipe for reflected and transmitted modes as shown in Fig. 25. Typical time records for reflected and transmitted signals are shown in Fig. 27. In this example, the depth of the outer surface crack is $p = 50\%$ of the thickness of the wall and the curvature parameter is $\Delta = 0.25$. Although some of the energy of the incident mode is converted to L(0,1) mode and there are also some modes reflected and transmitted due to the impure excitation of L(0,2) mode but then the traveling distance of the waves has been taken long enough allowing for the separation of the wanted wave packets. The reflection and transmission coefficients were calculated in the frequency domain, dividing the spectrum of the reflected or transmitted signal by that of the incident wave signal.

The motion of the crack was monitored on both sides of the crack - in the nodes to the left and right straight along the crack. Displacements in both directions r and z were recorded at these points.

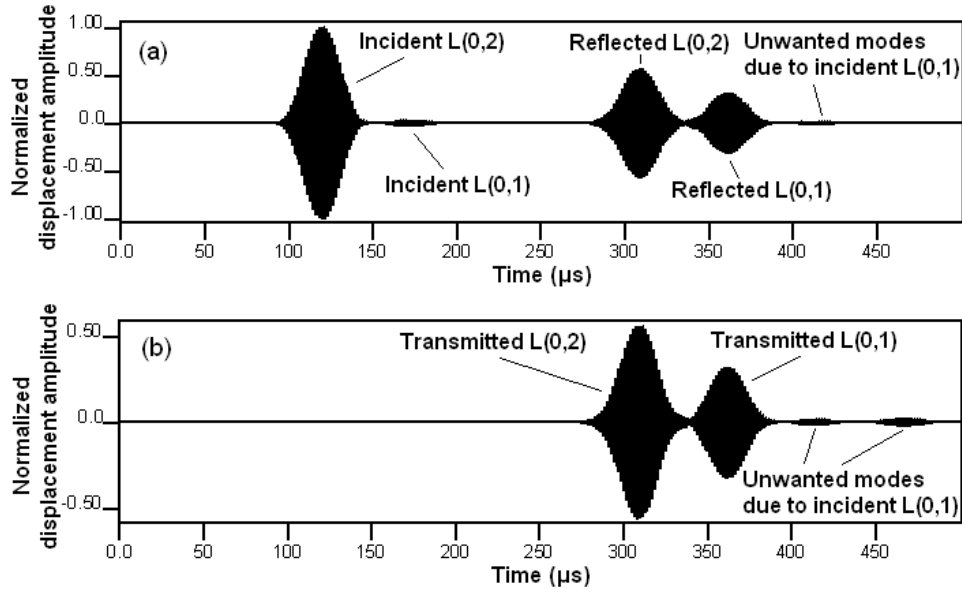


Figure 27. Typical time records of u_z displacement from FE simulations; the crack is $p = 50\%$ deep, the pipe's curvature parameter is $\Delta = 0.25$. a) Reflected signal, b) transmitted signal.

2.5.3 Results and discussion

Validation of some numerical results

Fig. 28 shows the reflection coefficient of the L(0,2) mode from a circumferential notch which covers the whole pipe circumference and is half the wall thickness deep taken from the FE study by Alleyne *et al.*[43] and compared with the reflection from a zero-width crack in a pipe using the NME technique with GE approach. The frequency is varied from 60 to 85 kHz. A similar trend can be seen in the result but a remarkable difference between the values of the two reflection curves. The reason for this is that the axial width of the notch was different in these calculations. The width of the notch influences the reflection strength as it was shown by Lowe *et al.*[52] in case of the Lamb mode S_0 in a plate. They found that the reflection coefficient has a cyclic behaviour when plotted as a function of the notch width. Specifically, the reflection starts at a certain value when the notch width was zero, then raised as the notch width was increased and obtained the peak when the notch width was about 10% of the wavelength of an incident wave. The axial width of a notch in pipe FE study was 4% of the incident wavelength, therefore, suggesting a stronger reflection.

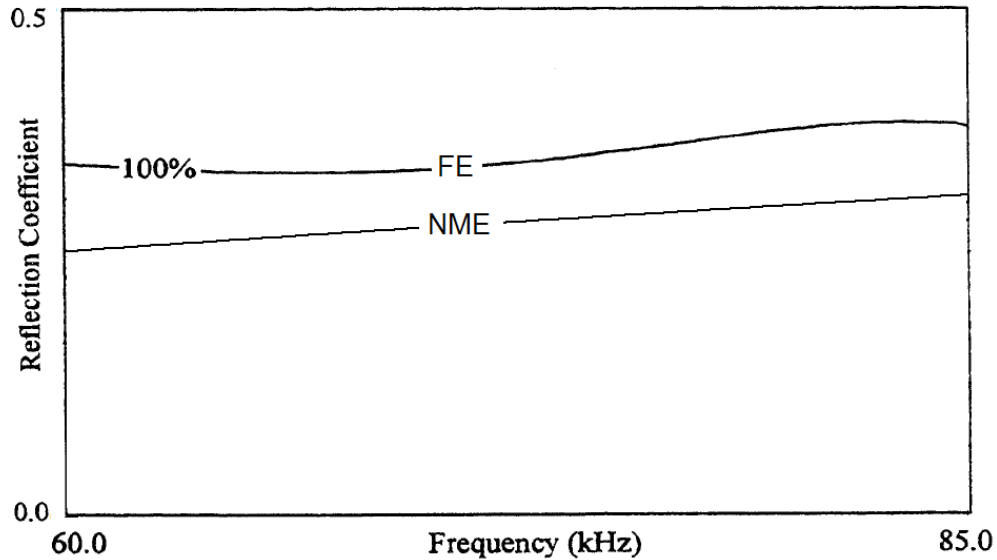


Figure 28. Reflection coefficients of the L(0,2) mode for the full circumference outer crack in a pipe with the depth $p = 50\%$ as the function of frequency; FE - Alleyne *et al.*, NME - current method.

Other results with L(0,2) mode are compared with the S_0 mode reflection from cracks in a plate. Such a comparison can be made with a pipe with a large diameter to wall thickness ratio, in that case the longitudinal modes correspond to plate Lamb waves. The predicted reflection function spectra for various crack depth and frequency-thickness values are shown in Fig. 29. The inner radius of the pipe was assumed 40 times bigger than the thickness. Predictions show the reflection to be an increasing function of frequency and of crack depth. There can be observed a good agreement between the results from FE study by Lowe *et al.* [52] and using the NME method on a pipe.

Finally, in Fig. 30, the crack motion in case of incident L(0,2) mode is compared with the crack motion in a plate for the S_0 mode from the study by Castaings *et al.* [12]. The correlation is again good between the results. They used a similar NME technique at 1.12 MHz-mm. There can be detected an opening behaviour of the crack due to the strong in-plane compression stress σ_{zz} , which causes unequal repartition of L(0,2) modes on both sides of the crack [12]. It is important to note that the model does not account for the contact between the crack faces that actually can take place with a zero-width crack, which faces might have opposite axial movements. In this case a more sophisticated approach, e.g. a crack model with a spring boundary enforced by quasi-static approximation, can be used [66].

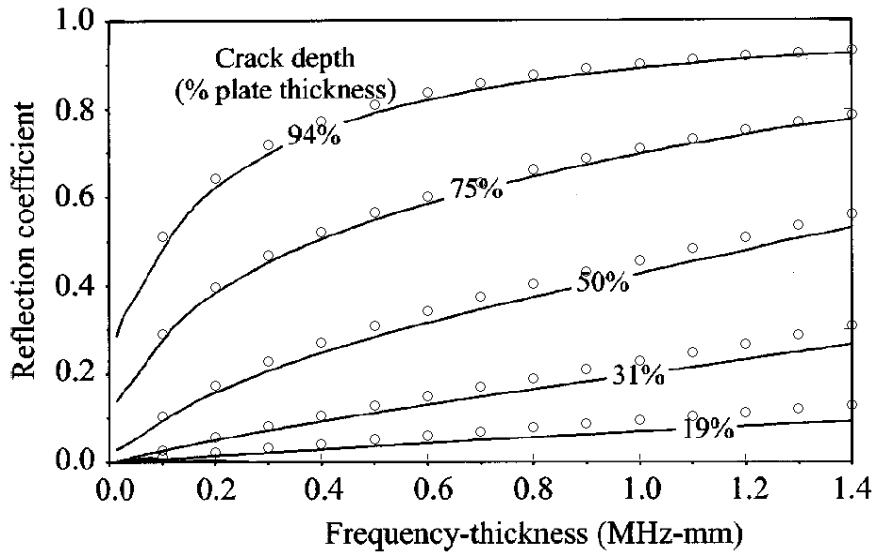


Figure 29. Reflection coefficients of the L(0,2) mode from a surface breaking crack, for various depths of the crack and frequency-thickness value; FE - Lowe *et al.* (solid line), NME - (o o o).

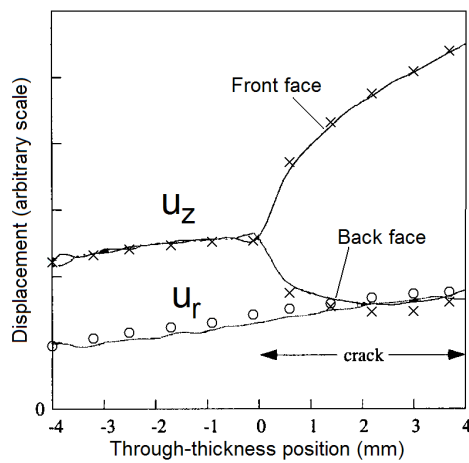


Figure 30. Through-thickness displacements on both sides of an outer-surface crack ($p = 50\%$) in a pipe for the incident L(0,2) mode at 1.12 MHz-mm. Result from Castaings *et al.* (solid line), pipe NME results: u_z - (x x x), pipe u_r - (o o o).

Reflection and transmission characteristics for L(0,2) incidence

Fig. 31 shows the reflection and transmission coefficients, as the function of the crack depth, for the L(0,2) mode in a pipe with various curvature parameters $\Delta = 0.25; 1.0$. Coefficients are calculated by monitoring axial displacements on outer surface of the pipe as it was shown in the FE setup in Fig. 25. Additionally, the energy balance of the scattering problem is considered by observing the relative error ϵ between the energies of reflected and transmitted modes. 99 modes were used in the expansion and the solution was calculated by GE scheme. The author was not able to produce satisfactory results by applying the other two, LS and SVD methods.

As expected, there can be detected a monotonic increase in the reflection amplitudes and decrease in the transmission strength along with the crack depth. Interestingly enough, the curves show that the results are remarkably dependent on the pipe curvature parameter and the location of the crack. While the reflection coefficient of the L(0,2) mode is the same from the outer and inner surface crack in a thin pipe ($\Delta = 0.25$), there is a remarkable difference in case of a thick pipe ($\Delta = 1.0$). Specifically, the reflection from a crack of the same depth on outer surface is much stronger than from the one on the inner surface of the pipe. The reason for this is the change in wave propagation characteristics of the incident mode due to the pipe curvature. Fig. 26 showed that the axial displacement u_z component is almost constant for a thin pipe suggesting equal sensitivity to an outer and inner surface crack. However, in case of a thick pipe it can be seen that the displacement value on the outer surface is much larger than close to the inner surface indicating better sensitivity. The results of NME technique are in a good agreement with the FE data. However, there is a reason for concern when observing the energy balance. In the case of a thin pipe ($\Delta = 0.25$) the energy error ϵ is around 2% but for thicker pipes it reaches 12% for some crack depth values. The error did not decrease when the number of modes was increased in the expansion.

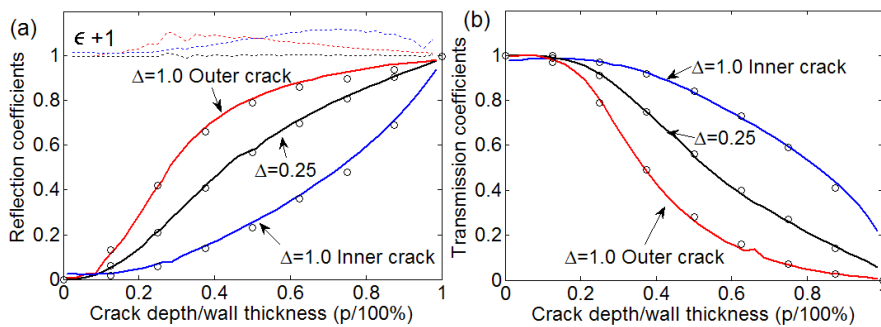


Figure 31. Predicted (a) reflection and (b) transmission coefficients of L(0,2) mode and relative error ϵ in energy balance (dotted line) for L(0,2) incident on outer and inner surface crack as a function of relative crack depth at 1.3 MHz-mm. NME results (—); FE results (o o o).

As the defect represents the non-symmetric reflection boundary in the waveguide, and more than one mode can propagate in the pipe at the studied frequencies, the mode conversion phenomenon may occur. This means that a part of the incident mode energy can be reflected or transmitted into L(0,1) mode. Fig. 32 shows the reflection and transmission coefficients, as the function of crack depth, for the L(0,1) mode in a pipe with a various curvature parameter $\Delta = 0.25; 1.0$. Coefficients were calculated by monitoring axial displacements on the outer surface of the pipe. Again, the results depend on the curvature parameter and the location of the crack. We can see that monitored displacements of the mode converted L(0,1) mode are the strongest in case of a thin pipe ($\Delta = 0.25$) at a half-thickness crack depth. When the pipe is thicker, the amplitudes of the reflected and transmitted L(0,1) mode weaken and the maxima are shifted toward smaller crack depths for the outer crack, and larger crack depth values for the inner crack depth. It can be seen from the results that there are some discrepancies in the results of the two methods. Especially the curve calculated by NME method and representing the displacement amplitude of the reflected and transmitted L(0,1) mode from the inner crack for a pipe $\Delta = 1.0$ does not approach zero when the crack depth comes close to zero, which happens with the FE results. This can indicate some inconsistency in a numerical NME solution or some additional physical phenomenon due to the pipe curvature that is not considered in the crack problem.

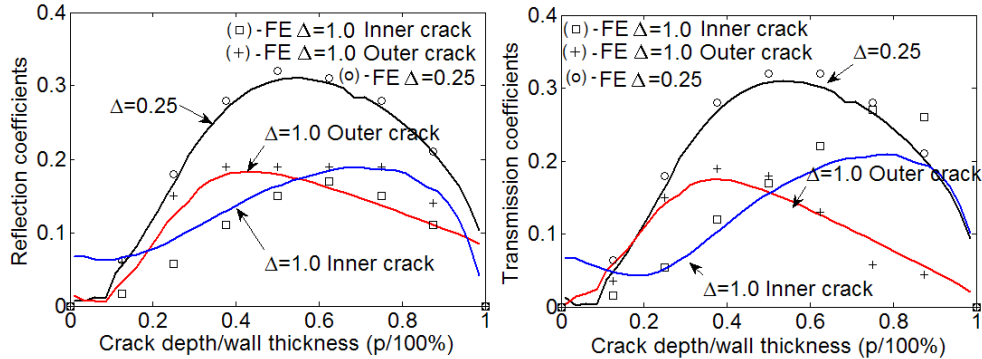


Figure 32. Predicted (a) reflection and (b) transmission coefficients of L(0,1) mode for L(0,2) incident on the outer and inner surface crack as a function of relative crack depth at 1.3 MHz-mm. NME results (—) and various FE results.

In principle, it is possible to determine the surface where the crack begins from by measuring the mode conversion intensity. In Fig. 33(a) the ratio of the reflected L(0,1) and L(0,2) mode displacement amplitude is shown for the inner and outer surface breaking crack for a pipe ($\Delta = 1.0$). It can be seen that the conversion to L(0,1) is much stronger for the inner surface crack and the curve, as a function of

the crack depth indicates that this difference increases along with the reduction of the crack depth. This demonstrates that it is easier to differentiate small cracks, which is important from the practical point of view. Fig. 33(b) shows how the conversion intensity is affected by the curvature parameter Δ for different crack depth values. The curves show the ratio of the reflected L(0,1) intensity from the inner and outer crack, respectively. As expected, larger conversion intensity is more notable in thick walled pipes and the ratio approaches 1 in thin walled pipes.

In practical pipe testing this information should be used with care. Usually, the cracks do not cover the whole pipe circumference which causes also other nonaxi-symmetric modes to be scattered from cracks than only L(0,1) in case of L(0,2) incidence [44]. Secondly, the shape of the defect influences the scattering. For example, even non-zero axial width of the crack can affect the scattering considerably [52]. And thirdly, the need to change the testing frequency, not considered here, which has an effect on wave propagation and scattering characteristics.

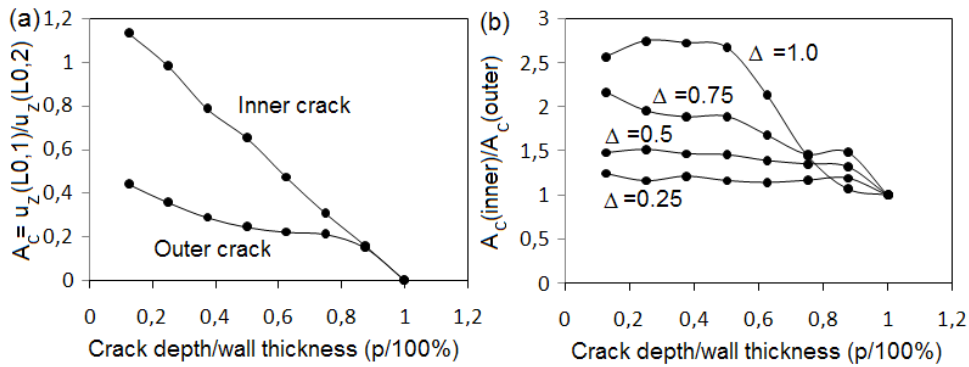


Figure 33. Predicted FE results showing (a) mode conversion intensity and (b) mode conversion intensity ratio for inner and outer cracks for L(0,2) incident at 1.3 MHz-mm.

2.6 Summary

A theoretical investigation of axi-symmetric longitudinal wave propagation in elastic pipe with discontinuities has been presented. Specifically, the scattering of the L(0,2) mode at the edge of a pipe and a full-extent circumferential crack has been modeled by applying the normal mode expansion technique and Finite Element method.

It has been shown that the wave propagation characteristics depend on the curvature of the pipe, which also affects the wave interaction with features.

Firstly, a well-known phenomenon in a plate, the edge resonance, which is caused by the vibration of inhomogeneous wave modes, also exists in a pipe. In a thin-walled pipe it has a similar character to that in a plate, but for thick pipes the influence of the curvature cannot be neglected with a thickness to medium radius ratio $\Delta > 0.5$.

In this case, through-thickness axial displacement distribution is no more symmetric with respect to the middle surface of the pipe, and the results will increasingly differ from those of the plate. The study of the curvature effect on wave propagation showed that the edge resonance in case of L(0,2) weakens when curvature radius decreases, and the resonance frequency shifts to higher values. Interestingly enough, at $\Delta = 0.667$ the L(0,2) wave was completely converted into L(0,1) and L(0,3) wave modes at the resonance frequency. The edge resonance of the pipe was experimentally detected by observing the displacement field near the edge caused by incident L(0,2) mode. Both FE and the experimental studies confirmed the existence of the edge resonance in pipes and were in a good agreement with the theory.

Secondly, in the study of L(0,2) mode interacting with a surface breaking crack at the frequency-thickness 1.3 MHz-mm showed that there is a clear difference in the reflection and transmission characteristics between a thin- and thick-walled pipe. In a thin-walled pipe, the scattering character from the outer and inner surface crack is the same but differs in case of a thick pipe. In a thick pipe the reflection of L(0,2) mode from the outer crack was larger than from the inner crack, and the mode conversion intensity to L(0,1) mode helped to distinguish the crack surface origin.

The present method is also applicable to 2D-modelling of torsional mode interactions with discontinuities in a pipe wall.

3 Scattering of the SH_0 mode in a plate when incident at a crack aligned in the propagation direction of the mode

3.1 Background

The subject of this chapter is to investigate the interaction of the low frequency fundamental shear horizontal mode SH_0 with a crack in a plate. This mode is particularly attractive for this study because the particle displacement is perpendicular to the plane of propagation and therefore it is expected to be sensitive to cracks that are oriented along the propagation direction. Lamb modes such as A_0 and S_0 can also be used for the detection of cracks in plates [52, 53] but they have the particle motion entirely in the plane of the propagation and are thus expected to be reflected less by axially aligned cracks. The SH_0 mode is also very similar in nature to the torsional mode $T(0,1)$ in pipes, the only difference being the geometric curvature of the material. The $T(0,1)$ mode is the main mode of choice for the established long range guided wave pipe inspection tools [3]. Therefore, this study can be helpful to practical pipe testing by improving understanding of the torsional mode interaction with axial cracks in pipes.

Studies of the interaction of shear waves [63, 67–72] and Lamb waves [4, 12, 52, 53, 73] with discontinuities such as thickness changes have already been performed by other authors. For example, Finite Element method (FE) simulations and experimental studies [4, 52, 53] have helped to understand the interaction of individual Lamb waves with a variety of defects. It was shown that the sensitivity of different wave modes to particular notches or cracks is dependent on the frequency-thickness product, the mode type, the mode order, and the geometry of the reflector. Also, analytical approaches, such as modal decomposition, have been useful to describe the role of nonpropagating modes on the reflection and transmission characteristics from thickness changes in planar waveguides using various wave modes [12, 63, 70]. A popular method used has also been to combine Finite Element and analytical techniques for analyzing the interaction of guided waves with arbitrarily shaped planar cracks [68, 69]. However, all these approaches have been focused on defects which are aligned normally to the direction of wave propagation and are, therefore, not suitable for explaining the case of an axial crack which has a small, or indeed negligible, dimension in that direction.

Recent papers by Rajagopal and Lowe [71] showed that the analysis of the SH_0 mode scattering, normally incident at a finite crack, can be performed with a plane stress model, using the FE method. Their study showed that at normal incidence to the face of the crack, the nearby reflected field is strongly affected by the surface waves, diffracting at the tips of the crack. In the present case, these surface waves play a much more important role, because there is no straight reflection due to the

limited or zero cross-section area of the crack. A parallel phenomenon can be seen from the classical problem where bulk shear waves interact with the boundary of a semi-infinite medium at grazing incidence [74]. Moreover, the problem resembles closely that of a bulk shear wave scattering by internal cracks in an infinite media at low frequencies. In this case, the incident mode is converted to Rayleigh surface waves, which travel along the surface of the crack and are diffracted and reflected at the tips of the crack, thus forming the wave field around the crack [75].

The chapter begins with a small introduction into wave propagation characteristics in a plate at low frequencies. Thereafter the scattering characteristics of SH_0 incidence from aligned cracks in a plate will be determined by using FE method. The scattering is investigated for a range of crack lengths, depths and shapes. The report focuses on the straight reflection back towards the source, which is monitored at several distances from the crack. Also, some results are shown for the diffraction of the SH_0 mode in the direction of 90 degrees from the crack face. The predictions are validated by experiments. Finally the influence of several surface waves on the scattering mechanism is investigated. The results of this study will be essential to understand the physical nature of the phenomenon and provide some insight into the possibility of detecting and characterizing this kind of defect using ultrasonic guided waves.

The work presented in this part was the result of collaboration between the Department of Mechanics at Tallinn University of Technology and the the Nondestructive Evaluation Group at Imperial College London. It resulted in a joint publication [P4].

3.2 Low frequency guided waves in a plate

The properties of Lamb waves and SH waves were extensively studied during the past [76]. Fig. 34 presents the group velocity dispersion curves for a steel plate. These group velocity curves show the speed of propagation of a wave packet and are, therefore, useful for long range testing. They were calculated using the program Disperse [18]. In practice, the authors favor an approach to NDT in which the signals are kept as simple as possible and to avoid multimodality [77]. Therefore, the work presented here is limited to the very low frequency-thickness range below 400 kHz-mm, where only three modes - A_0 , S_0 and SH_0 - may exist. This relatively low frequency range is also of particular interest to the authors because this aids our understanding of the case of pipes with cracks where a low frequency torsional wave is used [78].

The SH_0 mode is very attractive for long range NDT. It is completely nondispersive at all frequencies, and its phase velocity and group velocity are equal to the bulk shear wave velocity. The displacement and stress fields of this mode are also simple. In Fig. 35, the mode propagating in the x direction has only one displacement component, u_z , in the z direction and one component of stress. Also, its displacement

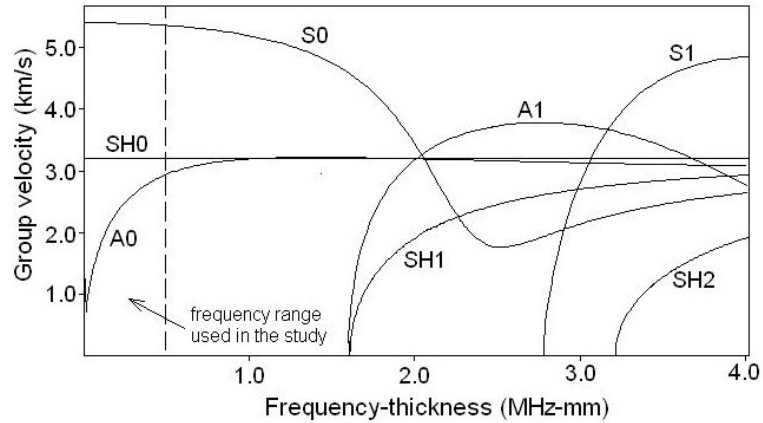


Figure 34. Group velocity dispersion curves for shear and Lamb waves in a steel plate.

and stress are uniform through the thickness of the plate so that its sensitivity to a defect is not dependent on the through-thickness location of the defect. The absence of normal displacement means that there is no attenuation if the plate is in contact with inviscid liquids. The main advantage of using the SH_0 mode in the current study is that its particle motion is perpendicular to the crack surfaces. Therefore it might be sensitive to such defects and provide reflections that characterize the crack.

Although the S_0 and A_0 modes have been used efficiently in defect characterization [52, 53], they are not suitable for the detection of cracks aligned in the wave propagation direction. Both modes have particle motion which is entirely in the plane of the propagation and, therefore, obviously their wave field is much less affected by axially oriented defects. The S_0 mode, being the fundamental symmetric compressional wave, has a predominant in-plane motion in the direction of x . The A_0 mode represents a flexural type of mode having predominant out-of-plane displacement u_y ; in-plane displacement u_x , and stresses σ_{xx} are antisymmetric with respect to the mid-plane of the plate. However, since these two waves may exist within the frequency range of interest, it is possible in principle, for both of them to be excited by mode conversion when SH_0 is incident.

3.3 Finite Element modelling

3.3.1 Plate with a through-thickness notch

The Finite Element study was performed in a two-dimensional domain, with the assumption of plane stress, using the ABAQUS software with its explicit time stepping

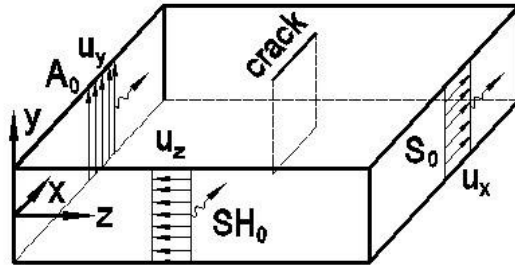


Figure 35. Predominant displacement mode shapes of A_0 , S_0 and SH_0 at low frequencies propagating in x -direction.

procedure [42]. The plane stress approximation has been found to work very satisfactorily in earlier studies modeling the SH_0 mode propagation in plates [71].

The spatial model of the problem is shown in Fig. 36(a). The properties of the material are shown in Table. 4. The mesh of the plate consists of perfectly square four noded linear elements with 2 degrees of freedom (displacements in x , z directions). More than 16 elements per wavelength of the SH_0 mode were used in the study, which satisfies the limit for accurate modeling [71]. Also, these elements describe satisfactorily the motion of the S_0 and SH_0 modes at low frequencies, since these modes have predominant in-plane displacement fields, which are symmetric to the mid-plane of the plate and approximately uniform through the thickness. This model does not support the propagation of the bending type modes, such as A_0 . However, antisymmetric waves are not generated in the cases studied in this work because all of the features of the geometry and of the incident wave are symmetric. The plate is surrounded by an absorbing region [45]. The waves that enter this area are increasingly damped and eventually they die out. This helps to reduce the model size and avoid unwanted reflections from the edges of the plate.

Variants of the spatial models were set up in order to model different cracks, shown in Fig. 37. The following three geometries of the discontinuity were modelled. 1) Crack. This defect type was created simply by disconnecting adjacent elements in the plate model. This approach to defining a crack has been used widely in previous FE studies of guided wave interactions with defects [52, 53, 71]. 2) Rectangular

Table 4. Material properties for steel used in the FE plane stress model.

Density ρ (g/cm ³)	Poisson's ratio ν	Young modulus E (GPa)
7.9	0.3	210

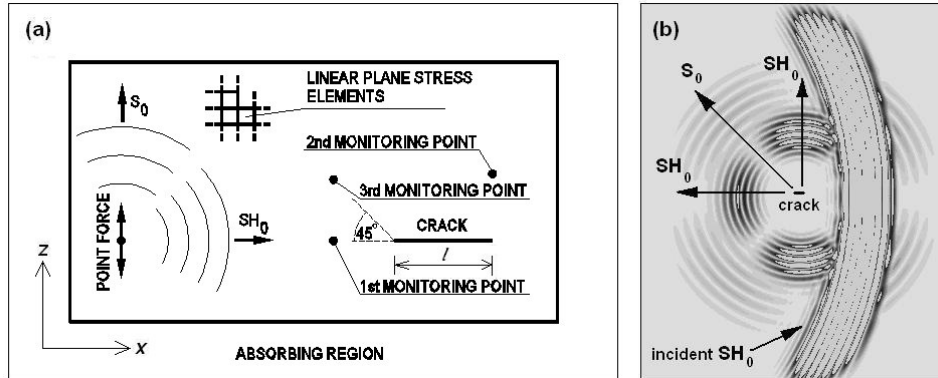


Figure 36. (a) Setup of the FE model. (b) Typical FE time record showing the displacement amplitudes of reflected and diffracted waves around the crack after the interaction of the SH_0 mode with the 24mm long crack.

notch. The notch is defined by removing elements from the mesh of the plate. The width of the elements along the notch line was also modified when necessary to obtain the desired width of the notch. Additional Finite Element analyses with further refinement of the mesh (results not shown here) showed that the unequal element dimensions used in the simulations did not cause discrepancies in the wave propagation. However, care must be taken when modeling very narrow notches. The reduced size of the element also increases the calculation time. 3) V-notch. This geometry is suitable for modeling very narrow notches but with sharp tips. Defect geometries 2) and 3) were important to compare the FE results with experiments where a finite width machined notch was used.

Low frequency excitation in the z direction was applied at the desired node on the crack axis. This generates circular waves of the SH_0 mode primarily propagating in the x direction, and also the S_0 mode, which primarily propagates in the z direction. The displacement amplitude of both modes is the strongest in their principal direction of propagation and decays according to a cosine angular pattern away from the main direction [79]. Although this means that the S_0 mode can be present in areas away from the crack axis, at low frequency-thicknesses this mode travels much faster than SH_0 and can be time-gated out. The point force excitation consisted of a 100 kHz five cycle tone burst multiplied by a Hanning window. The propagation of the waves was simulated in the time domain. Explicit time integration and a fixed time step, corresponding to stable integration, were used for the simulation [80].

The signals were monitored at three different positions [Fig. 36(a)]. The choice of these points was made after trial simulations and points were selected at locations where the scattered wave field was the strongest. A typical plot, showing the contour

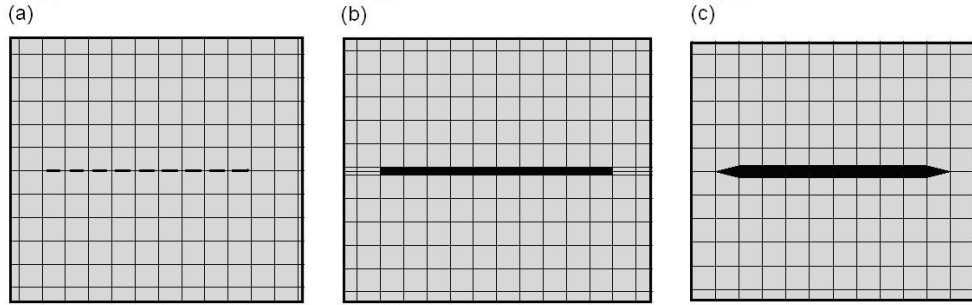


Figure 37. FE defect models: (a) crack, (b) rectangular notch, (c) V-notch.

of resultant displacements of different scattered waves after the interaction of the incident mode with the crack is illustrated in Fig. 36(b). In the first location, which is along the line of the crack and the excitation point, the displacement u_z of the reflected SH_0 mode was monitored. The second monitoring point is at 90° from crack line, measured from the back tip of the crack, in order to monitor the displacement u_x of the diffracted SH_0 mode. In the third position, which is at 45° to the incident direction and has the same x coordinate as the first monitoring point, the displacement component u_z of the reflected S_0 mode was monitored. The incident signal was always monitored at point 1. The model was repeated for different crack lengths. The main focus was directed towards scattering of cracks, which length was up to the wavelength of the incident mode, but the direct reflection was also investigated for long cracks of up to 15 wavelengths in length.

Both modulus and phase of the reflected and diffracted signals were calculated. The modulus was obtained by dividing the amplitude of the reflected or diffracted signals by the amplitude of the incident signal in the frequency domain. To obtain the results for plane waves interacting with the crack, it is necessary to consider the beam spreading of the propagating waves. This is necessary for the comparison of plate results with pipe results. As the waves in the plate model decay cylindrically away from the source, and also assuming the crack to act as the emitter of cylindrical waves, the reduction of the amplitudes in both cases is inversely proportional to the square root of the propagation distance from the source. Thus

$$Coefficient = \frac{A(f)\sqrt{r}}{I(f)\sqrt{d}}, \quad (41)$$

where $A(f)$ is the amplitude in the frequency domain of reflected or diffracted signals, $I(f)$ is the amplitude in the frequency domain of the incident signal, r is the distance between the tip of the crack and the monitoring point, and d is the distance from the source to the monitoring point. The phase was calculated only for the reflected and diffracted SH_0 signals and was obtained by using a simple FFT algorithm.

3.3.2 Plate with a part-through notch

The second study was performed in a three-dimensional domain, using 8 noded linear cubic elements in the plate mesh. 5 elements were used through a 3 mm thick plate. Cracks of a vanishing width were created by disconnecting nodes on elements representing adjacent faces. Also, notches of a 0.6 mm width were created by removing rows of elements from the mesh. The material for the plate was steel, but also material properties of aluminium were used (Table 5), simply in order to match the experiment.

Other parts of the model were similar to the one shown in Fig. 36(a). The plate was surrounded by an absorbing region which helped to remove the unwanted side reflections. The excitation was achieved by applying a force parallel to the plate surface at the desired node in a perpendicular direction to the crack axis. This generates circular waves of the SH_0 and S_0 modes, with their principal directions parallel and perpendicular, respectively, to the applied force and no A_0 is generated. The point source excitation consisted of a 5 cycle Hanning windowed tone burst centered at the required frequency. The propagation of the waves was simulated in the time domain. The signals were monitored in the first and second monitoring points (Fig. 36(a)).

The reflection and diffraction behaviour of SH_0 mode was studied by calculating the frequency domain ratio (41) of the monitored signals.

Table 5. Material properties for the aluminium used in the FE 3D model.

Density ρ (g/cm ³)	Poisson's ratio ν	Young modulus E (GPa)
2.7	0.33	70

3.4 Experimental work

Two sets of plates were used for the experiments described in Table 6. Notches with various depths and lengths were cut into each plate using a milling machine. The notches were positioned approximately 800 mm from one end of the plate, with its axis lying at equal distances from the other sides of the plate, as shown in Fig. 38.

Table 6. Plates with defects used in the experiment.

	Plate size (mm·mm·mm)	Material	Notch depth (%)	Notch length (mm)	Notch width (mm)
1. set	1250×1250×1	steel	100	4, 8, 12, 70	0.7
2. set	1250×1250×3	aluminium	80	3.5, 5.8, 8, 11.4	0.6

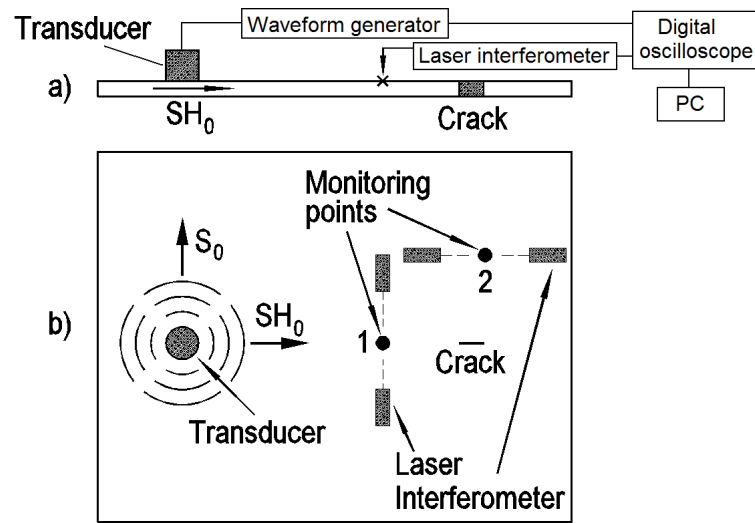


Figure 38. Arrangement of the experimental test. (a) side view, (b) plan view.

Excitation of the SH_0 mode was achieved using a wide-band piezoelectric shear transducer (Panametrics V301, 0.5 MHz center frequency) coupled to the plate through a small area using a small brass disc (3 mm diameter, 0.4 mm thickness) and a shear coupling agent. The excited signal consisted of a five cycle tone burst in a Hanning window centered at the required frequency. Such narrow band signals were used in order to achieve a good signal strength. For each crack length, the center frequency of excitation was varied from 200 kHz to 400 kHz in order to obtain different values of length of the crack in terms of the wavelength of the incident mode. This scaling is permissible because the SH_0 and S_0 modes in the low frequency range of study have velocity and mode shapes which are independent of the plate thickness; thus the only spatial dimensions of the problem are the crack dimensions and the propagation distances. The signals were generated using a Wavemaker (Macro Design Ltd, UK) instrument.

The monitoring of the incident signal and detection of the reflected and diffracted signals was achieved using a laser interferometer (Polytec OFV 2700, with dual differential fiber optic lines) to measure the displacements at the surface of the plate at the required positions. Two laser beams were aligned at +30 degrees and -30 degrees to the normal, but focused on the same spot; thus the difference between their two signals gave the in-plane displacement. In the test with aluminium plates it was decided to measure in-plane velocity. The reason for this was the better signal-to-noise ratio of the velocity decoder at the frequencies used here. A thin reflective tape was attached to the surface of the plate to enhance the optical backscatter. The signals were in general quite weak and the quality of each measurement was enhanced by

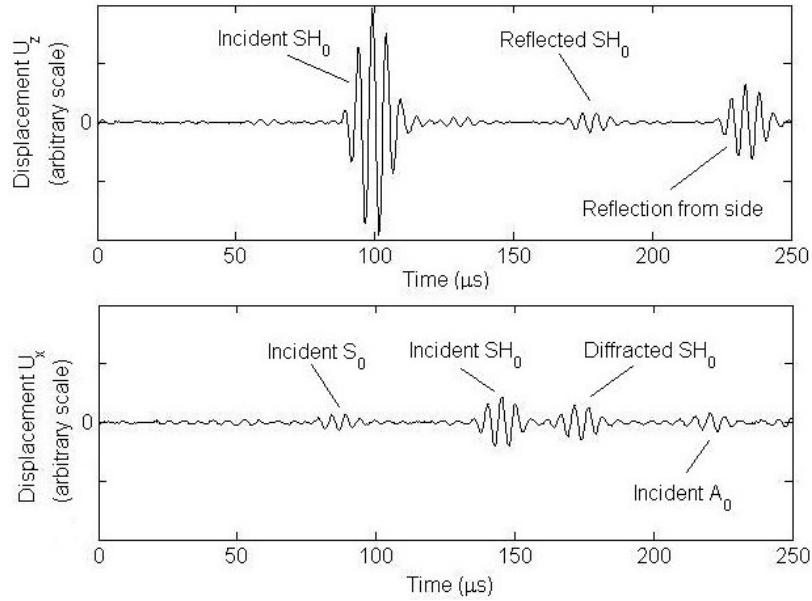


Figure 39. Typical experimental signals; center frequency is 200kHz; the through-thickness notch is 12 mm long. (a) time record from the 1st monitoring point 118 mm away from notch, (b) time record from the 2nd monitoring point 118 mm away from notch. Both signals are plotted to the same scale.

taking 500 averages and by applying a band pass filter.

The excitation and detection positions were varied at each center frequency value, so that the distances between the crack and monitoring point and transducer remained a certain number of wavelengths. Typical experimental time records measured at the 1st and 2nd monitoring points are shown in Fig. 39(a) and Fig. 39(b), respectively. The length of the through-thickness notch was 12 mm, excitation frequency 200 kHz, the signal was generated at $22 \lambda_{SH_0}$ (SH_0 wavelengths at the center frequency of the tone burst) away from the notch and the measurement distance from the notch was $7 \lambda_{SH_0}$ for both measurement points. From the measurement in Fig. 39(a), it can be seen that only the incident and reflected SH_0 mode are presented, but in Fig. 39(b) the measured signal at the 2nd point contains also some S_0 and A_0 modes that were excited by the transducer. Differentiation of unwanted signals and the SH_0 mode may most easily be achieved by choosing sufficiently long propagation distances that their signals separate.

The coefficient of the reflected and diffracted SH_0 mode for each crack length was calculated similarly to that of the FE procedure, by dividing the frequency spectrum of the reflected signal by that of the incident signal and compensating for beam spreading.

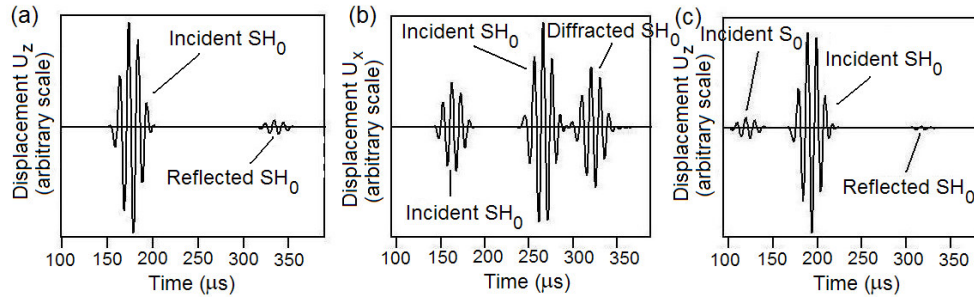


Figure 40. Typical FE time records from the (a) first, (b) second, and (c) third monitoring points showing the reflected and diffracted signals; 0.7 mm wide notch 24 mm in length was used in the model; and center frequency of the incident pulse is 100 kHz.

3.5 Results and discussion

3.5.1 Through-thickness crack: reflection and diffraction as a function of crack length

Using the results of the FE simulations, the scattering effect was studied with SH_0 mode incident. This was done over varying defect lengths in a plate. The excitation was located at a distance of $22 \lambda_{SH_0}$ and nodal displacements were monitored at $7 \lambda_{SH_0}$ from the defect. Fig. 40(a,b,c) shows the typical FE time history records monitored at the 1st, 2nd and 3rd points. Notch is 0.7 mm wide and 24 mm long ($\lambda_{SH_0}/l = 0.75$, where l is the length of the notch). The figures show that the incident, reflected and diffracted parts of the signals are separable, allowing time gating for the calculation of the modulus of reflection and diffraction.

The reflection and diffraction coefficients were calculated for each crack length using Eq. 41 and the results of different excitation frequencies and crack lengths were normalized to the wavelength of the incident mode SH_0 . In the FE study, the excitation frequency was 100 kHz, and in the experiment this was varied from 200 to 400 kHz. Experimental measurements were taken at the appropriate excitation and monitoring distances for each frequency. It is important to add here that the results of 100 kHz would be valid at other excitation frequencies, provided the crack length and the other dimensions are scaled appropriately by incident wavelength.

At first, we investigate the scattering at short cracks the length of which is comparable to the wavelength of the incident mode. This means that the direct reflection of SH_0 includes the reflection components at the tip and at the end of the crack which are not separable in the signal. Fig. 41 shows the reflection modulus for monitored SH_0 modes at the 1st and S_0 mode at the 3rd point. The predictions for direct SH_0

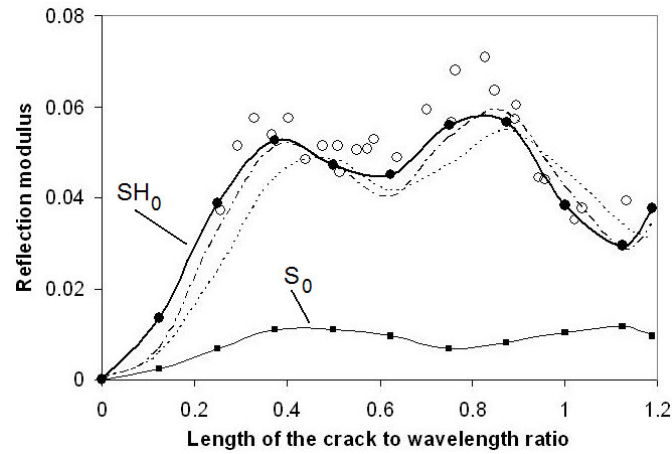


Figure 41. Predicted variation of reflection modulus with length of the crack normalized to wavelength. Monitored SH_0 mode at the 1st point: FE results with a 0.7 mm width notch (solid circle), 0.7 mm width V crack (dash-dot), zero-width crack (dotted line), and experimental results (empty circle). Monitored S_0 at the 3rd point - FE results (solid square).

mode reflection were obtained for three defect cases: crack, 0.7 mm wide notch and 0.7 mm wide V-notch. As we see, the width of the defect slightly affects the reflection behavior. It can be observed that the reflection from the crack is slightly weaker, and its values are shifted towards higher crack length to wavelength ratios compared to other defect types used in the study. The simulations with a notch and with a V-notch are similar, and give the best agreement with the experimental results. The S_0 mode is clearly the weakest reflected signal and, therefore, it is not suitable for the defect characterization. However, it shows that the scattering phenomenon is accompanied by mode conversions. Due to the symmetry of the problem there is no reflection of the S_0 mode along the axis of the defect and the 1st monitoring point.

The reflection coefficient of the SH_0 mode at crack in Fig. 41 starts at a value of zero, and then rises, as the crack length is increased. But while we would expect the ratio to approach a constant value as the crack grows larger, there is an oscillation the origin of which is not clear. As we can see, the first maximum reflection occurs when the length of the crack is about 45% of the incident wavelength SH_0 . Then there is a low point at around 63%, followed by an increase again reaching a maximum at about 87%. Finally the ratio starts to drop again. This behavior is due to interference between the reflection from the near tip of the crack and the reflection slightly later from the far tip of the crack. This will be shown and discussed later. Their superposition in the resulting reflected wave packet may be constructive or destructive, depending on the duration of the delay. Thus, for example, the reflection from the far end of a crack of 45% wavelength returns with a delay corresponding to one

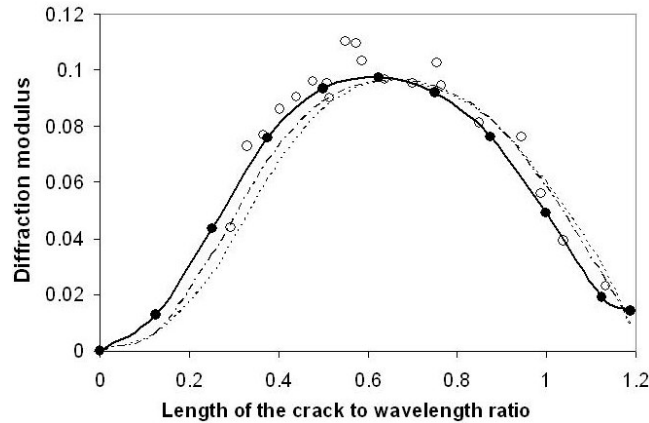


Figure 42. Predicted variation of diffraction modulus with length of the defect normalized to wavelength. Monitored SH_0 mode at the third point: FE results with a 0.7 mm width notch (solid circle), 0.7 mm width V-notch (dash-dot), crack (dotted line), and experimental results (empty circle).

wavelength, so that it is in the same phase as the reflection from the start of the crack, and thus causes maxima. However, the maxima and minima do not occur precisely at multiples of 25% wavelength positions, but at slightly smaller distances. The reason for this is that the SH_0 mode is partially converted to "Rayleigh type" surface waves, also known as pseudo-Rayleigh waves [81], on the stress free surfaces of the crack, which are reflected and diffracted at the crack tips. These waves are slower than the shear mode and have a smaller wavelength. Additionally, it is worth noting that these interfering waves have different amplitudes. This explains a reflection minimum that is not zero at 63% of λ_{SH_0} .

Fig. 42 shows the diffraction modulus of monitored SH_0 modes at the 2nd point, 90 degrees from the crack face. The diffraction in this direction is stronger than the reflection in the incident direction. Here we can see a similar initial rise of the diffraction strength with the increase in the crack length. However, there is a maximum instead of a trough at 60% of SH_0 compared with the reflection modulus of the direct reflection. Again "Rayleigh type" surface waves play an important role here. The diffraction is composed of two signals - one diffracted from the front tip of the crack and the other from the back tip of the crack. The second diffraction is delayed due to the surface wave propagation along the crack faces. However, this time the diffraction is in phase with the first diffraction, because there is no additional phase delay due to the absence of back propagation. Finally, the ratio starts to decrease. Again the finite width rectangular crack gives the best fit with the experimental results. However, the difference between the results with the different crack types is

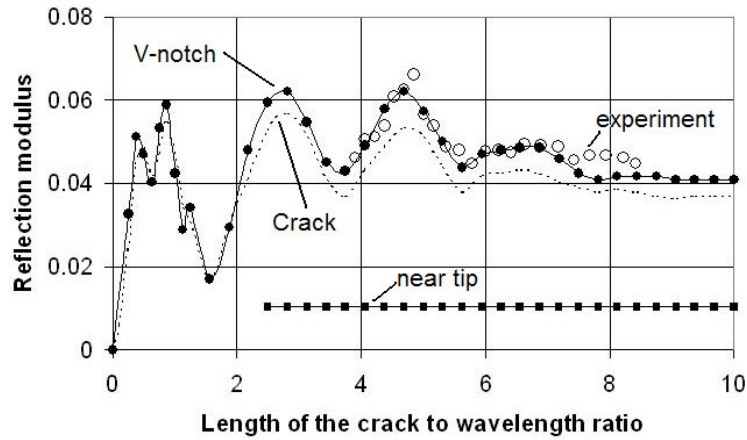


Figure 43. Reflection modulus of SH_0 mode for short and long defects. FE results: SH_0 near tip reflection at 0.7 mm V-notch (solid square), SH_0 far tip reflection at 0.7 mm V-notch (solid circle), and SH_0 far tip reflection at the crack (dashed). Experimental SH_0 far tip reflection (empty circle).

not significant.

The reflection character from longer cracks up to $10 \lambda_{SH_0}$ is investigated in Fig. 43. Predictions were made for the crack and the V-notch. There is a very good agreement between modeling and experimental results. Again we can observe that the reflection from the crack is slightly weaker compared to the other results.

Now we can easily separate the near tip reflection, which is notably smaller than the delayed far tip reflection. Its amplitude is independent of the crack length. Interestingly enough, the modulus of the far tip reflection, even if it is separated from the near one, remains periodically undulating with a weakening amplitude. The interval between peaks is longer for long cracks than for short cracks (in a wavelength range). The main reason for this is that the interference phenomenon is complicated considerably by the presence of another wave generated at the surfaces of the crack, the reflection of which is not separable from the reflected SH_0 in short crack cases. But the reflection of these waves can be seen separately in cases of long cracks, as shown in Fig. 44(a,b). Here it is important to note that the separation of reflected signals also depends on the duration of the tone burst. In case of a longer tone burst, the crack would also have to be longer before it is possible to separate the reflections. These figures show the FE and experimental time records of SH_0 wave interaction with a $8.1 \lambda_{SH_0}$ long crack. The two reflections are clearly separable - the smaller reflection at the near tip is followed by the second stronger reflection from the far tip, induced by "Rayleigh type" surface waves. But we can also see small amplitude waves arriving before the second reflection. These waves are generated due to the presence of

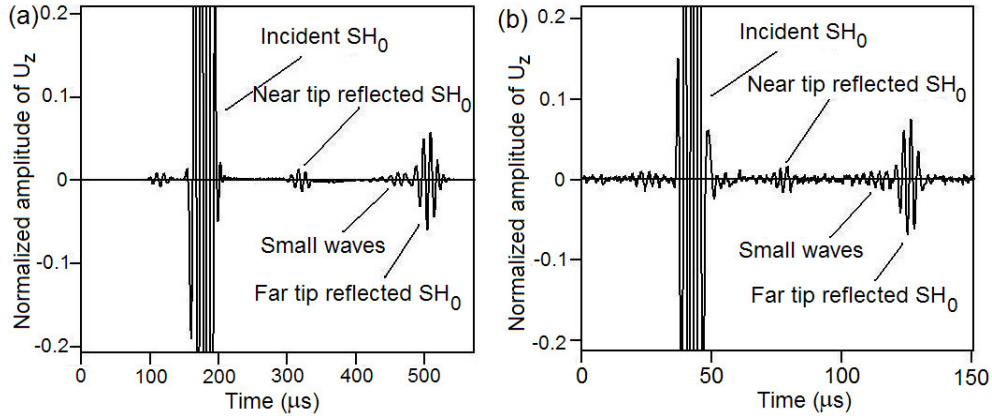


Figure 44. Typical time domain signals showing the reflections at long cracks. (a) FE measurement at 262 mm ($8.1\lambda_{SH_0}$) long crack, center frequency 100 kHz; (b) experimental measurement at 70 mm ($8.1\lambda_{SH_0}$) long crack, center frequency 390 kHz.

”leaky type” surface waves on the crack, which also cause small reflection of the SH_0 mode. These waves are faster than ”Rayleigh type” surface waves and are generated due to the S_0 mode interacting with the crack surfaces; this is a similar phenomenon to that of bulk pressure wave conversion to leaky surface waves on the free boundary of a semi-infinite medium [82]. Quantitative analyses will follow later. The weakening oscillation in Fig. 43 is explained by the fact that this wave is coupled into a plane shear wave that propagates away from the crack. Due to this, the surface wave loses energy and, thus, decays in its propagation direction. Therefore, the strength of the final diffraction weakens as the crack length is increased, and this also decreases the amplitude of undulations in superimposed signals as seen in Fig. 44.

3.5.2 Through-thickness crack: influence of the distance of source and measurement location on direct reflection

In order to see how the distance between the source, receiver and the crack influences the reflection of the SH_0 mode, FE predictions were made for a couple of source and receiver points along the crack axis. The distance between the source and measurement point was chosen to be $5\lambda_{SH_0}$, while the distance between source and the crack was varied through four values: $\lambda_s=10, 20, 30$ and $40\lambda_{SH_0}$. The crack length was again varied using a number of simulations, and the reflection modulus was calculated according to Eq. 41. Fig. 45 shows that the reflection modulus for all crack length to wavelength ratios decreases with the source distance from the crack. The reason for this is that the reflected waves show simple cylindrical decay away from

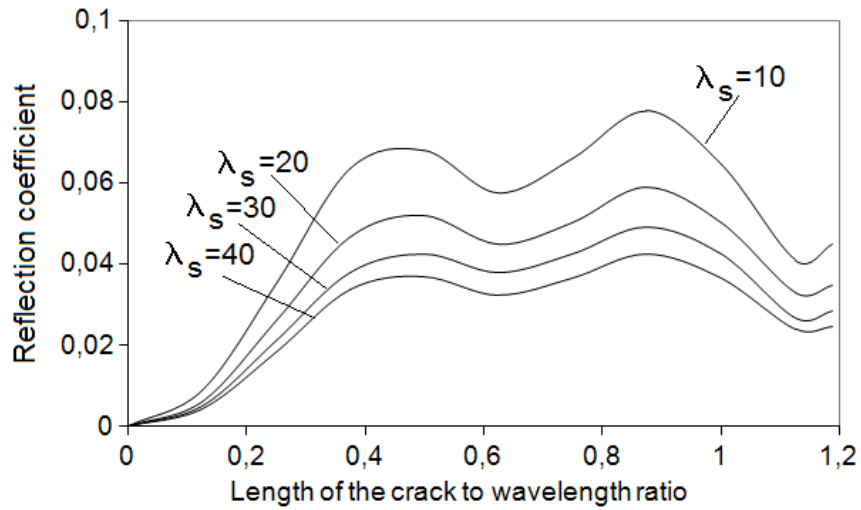


Figure 45. FE predictions of SH_0 reflection modulus as a function of crack length for various source distances λ_s from the crack. The distance between the source and monitoring point was always $5 \lambda_s H_0$.

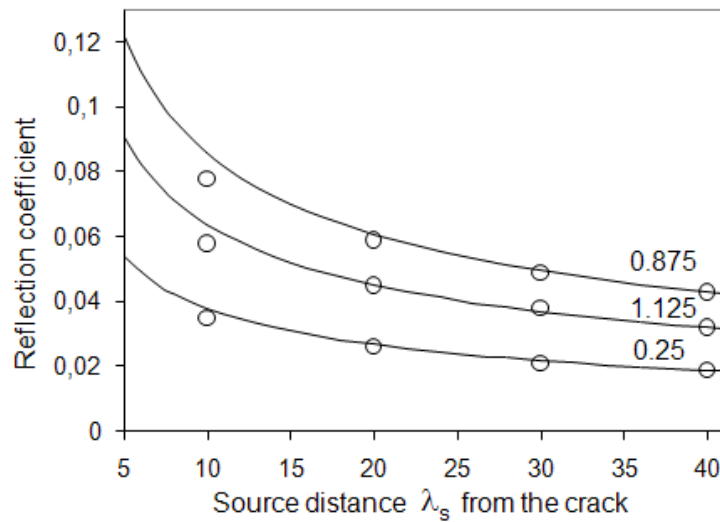


Figure 46. FE predictions of the dependence of reflection modulus on the distance between the source and the crack for different crack length to wavelength ratios. Reflection modulus extrapolated from the source distance $40\lambda_{SH0}$ (line), reflection modulus obtained using the source distances 10, 20 and $30\lambda_{SH0}$ (empty circle).

the crack. It is clearly seen that the reflection modulus for different source and measurement locations has the same variance when the crack length to wavelength ratio changes. The placement of peaks and troughs is similar for all curves. Moreover, the ratio of modulus M_1/M_2 of any two arbitrarily chosen source location results 1 and 2, at each crack length, can be expressed as a square root inverse ratio of source distances from the crack. This assumption is valid when the measurements have been made in the far field. In Fig. 46, the reflection modulus for different crack length to wavelength ratios 0.25, 0.875 and 1.125 is calculated using the modulus that is obtained at the source point $40\lambda_{SH_0}$ from the crack, and it is extrapolated to smaller source distances and compared with the exact calculations with source distances 10, 20 and $30\lambda_{SH_0}$. As we see, the results agree well when the source distance is equal or larger than $20\lambda_{SH_0}$, thus the compensation based on cylindrical spreading is acceptable.

3.5.3 A through-thickness crack: the influence of a "leaky type" surface wave on SH_0 reflection in the incident direction

The most important signal for identifying and characterizing the crack is that which reflects directly towards the source, measured at the 1st point. As we saw in Subsection 3.5.1, this reflection had an undulating nature due to the presence of different surface waves. Here we take a deeper look at the generation mechanism of this reflection to explain the contribution of "leaky type" surface waves to the reflection. In order to understand this we use FE simulations. We study the reflection for a very long crack $l = 15\lambda_{SH_0}$ and at central frequency 100 kHz. This ensures that all signals investigated can be separated and analyzed.

The wave field patterns from FE study at different time steps that describe the interaction and reflection/diffraction of the waves at the crack are shown in Fig. 47(a-c). Fig. 47(a) shows the wave field record when the incident SH_0 mode interacts with the front tip of the crack. It is seen that there is a small backward reflection, denoted as near tip reflected SH_0 , in the figure. Due to the free boundary of the crack edges, the incident mode and also the diffraction are converted to Rayleigh type surface waves at the tip. Besides, there is the diffracted S_0 mode, which is converted to leaky type surface waves on the crack faces. All these surface waves propagate toward the end of the crack and are reflected and diffracted. This is illustrated in Fig. 47(b). We can see that Rayleigh type waves are converted strongly to SH_0 modes and also to reflected S_0 modes, which again interact with the crack face causing the leaky type surface waves to propagate. Finally, the surface waves interact with the front tip of the crack, and the far tip reflected SH_0 mode is generated, shown in Fig. 47(c). It is obvious that this reflection is much stronger than the near tip reflected SH_0 .

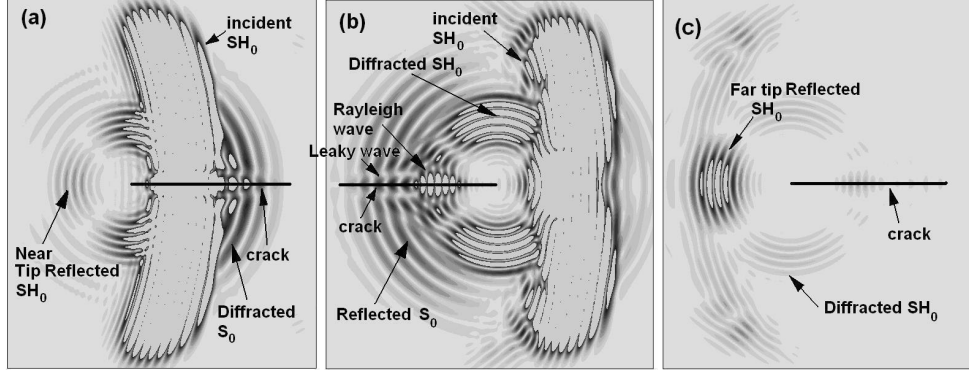


Figure 47. Various FE time records showing the displacement amplitudes of the wave field around the crack during the interaction of the SH_0 mode with the crack. (a) Incident SH_0 mode interaction with the near tip of the crack. (b) Rayleigh type wave interaction with the far tip of the crack. (c) Reflected and diffracted waves after back propagating leaky and Rayleigh type wave interaction with the near tip of the crack.

The interference phenomenon between different surface waves causes the undulations in the reflected signal. As we saw, they travel with different speeds along the crack face and their phase changes are, therefore, also different. By predicting the wave number of these waves we can explain the occurrence of the undulations more quantitatively. Following a procedure similar to that in the preceding parts of the work [71], the wave numbers of the surface waves can be calculated by measuring the phase difference between the diffracted and reflected signals as a function of the crack length. Here we investigate the diffraction at the second point and reflection at the first point (Fig. 36(a)) at an equal distance from the crack again. Fig. 48(a) and (b) show the corresponding time histories recorded at these points. We measure the phase ϕ_1 of the diffracted SH_0 mode (the last signal) in Fig. 48(a) by taking the Fourier transform of the gated signal. Similarly, we calculate the phase ϕ_2 of the far tip reflected SH_0 mode from the Rayleigh type wave contribution, and phase ϕ_3 of the reflected SH_0 from leaky type wave contribution, both shown in Fig. 48(b). Thereafter, we plot the phase differences $\Delta\phi_2 = \phi_1 - \phi_2$ and $\Delta\phi_3 = \phi_1 - \phi_3$ for increasing crack lengths. The slope of these linear variations yields then the wave number for the surface wave. Fig. 49(a) shows that the wave number for Rayleigh type surface waves is $k = 215.7$ rad/m. The corresponding phase velocity 2913 m/s is close to Rayleigh wave phase velocity 2966 m/s for the material properties used in the FE simulations. Fig. 49(b) gives the wave number for leaky type surface waves $k = 118.1$ rad/m, indicating that its phase velocity 5320 m/s is slightly lower than the phase velocity of the S_0 mode 5404 m/s of the studied plate.

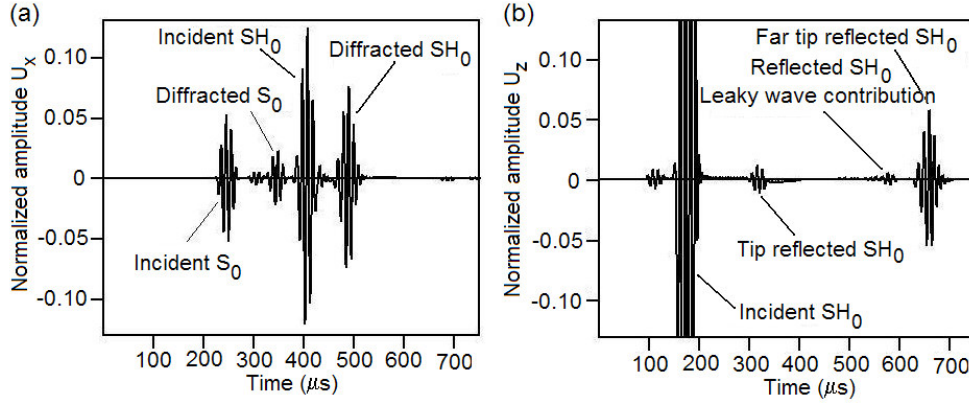


Figure 48. FE time traces; the length of the crack is $15\lambda_{SH_0}$; center frequency is 100 kHz. (a) Measurement at the second point; (b) measurement at the first point.

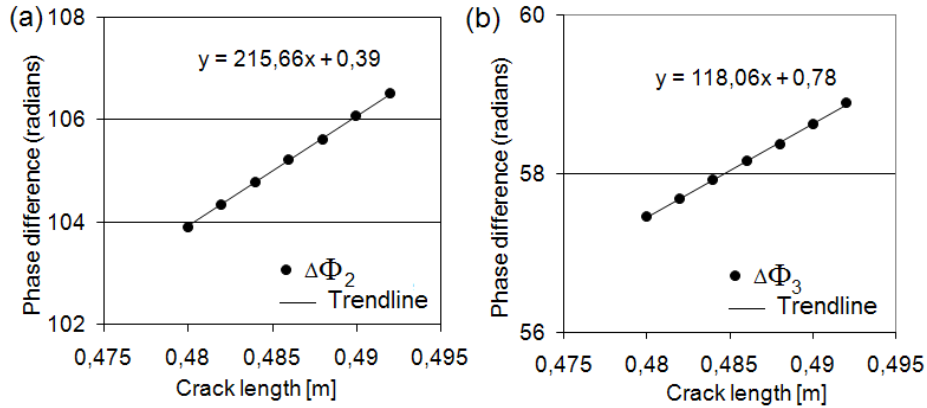


Figure 49. Phase differences from FE simulations as a function of crack length. (a) ϕ_2 and its slope showing the wave number of Rayleigh type surface waves; (b) ϕ_3 and its slope showing the wave number of leaky type surface waves.

Let us return now to Fig. 43 in Subsection 3.5.1, where the reflection modulus was characterized by undulations. Here the explanation to the undulations, which take place for crack lengths longer than $2\lambda_{SH_0}$, are given. We are interested in the period of these undulations. We can see from the figure that the reflections caused by surface waves are in the same phase when the crack length is $2.8\lambda_{SH_0}$. The changing part of the phase difference $\phi_2 - \phi_3 = 97.6 \times$ gives us the phase delay between these two reflections. The first minimum occurs after a half cycle calculated as $\pi/97.6$ which corresponds to $1\lambda_{SH_0}$ and the first maximum occurs after 1 cycle at $2\pi/97.6$ which

corresponds to $2\lambda_{SH_0}$. Similar values between the peaks and troughs are seen also in the figure; maxima occurring at $2.8, 4.8,$ and $6.8\lambda_{SH_0}$; minima lying at 3.8 and $5.8\lambda_{SH_0}$. This supports the fact that undulations in the reflected signal are caused by the interference of these different surface waves.

3.5.4 A part-through crack: reflection and diffraction as a function of defect depth, width and frequency-thickness

In practice, it is important to detect defects that are not through. Therefore, it is essential to know the impact of the defect depth on the scattering. Also, previous studies have shown that the scattering from a part-thickness defect is strongly influenced by the operating frequency [52, 53, 83]: in general, higher frequencies are more sensitive in finding smaller defects.

Firstly, it is shown that the scattering results are also dependent on defect width. Fig. 51(a) and (b) show the predicted reflection and diffraction coefficients as a function of a defect length from a 80% deep crack and notch which width was 0.6 mm. The incident SH_0 mode was generated at 250 kHz. Compared with the through-thickness defect results in Fig. 41 and Fig. 42 it can be seen that the width of the defect has a much stronger influence on the scattering from part-through defects. Similar observations were made in the study of SH_0 mode interaction with cracks at normal incidence [84].

Secondly, FE scattering studies with finite-width notches in aluminium plate were experimentally compared. Fig. 51(a) and (b) show the measured reflection and diffraction coefficient respectively at 200 to 325 kHz from a 80% deep notch in which the defect length was 3.5, 5.8, 8.8 and 11.4 mm long. The excitation was located at the distance $27\lambda_{SH_0}$ and nodal displacements of scattered SH_0 were monitored at $7\lambda_{SH_0}$

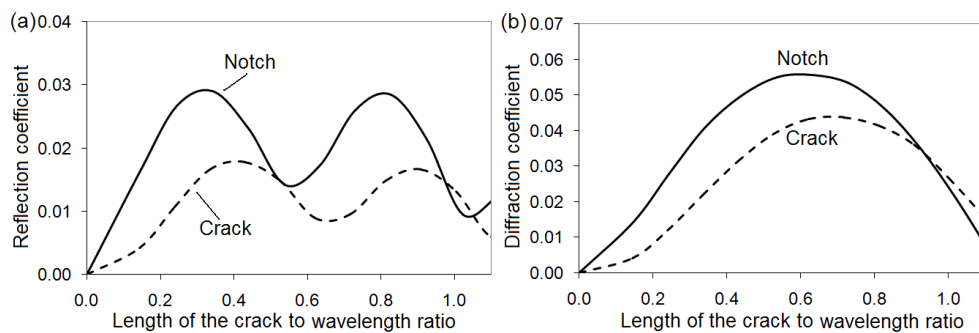


Figure 50. Predicted (a) reflection and (b) diffraction coefficients from an 80% deep crack and 0.6 mm wide notch expressed as a function of ratio of defect length to incident wavelength. The SH_0 mode was excited at 250 kHz in a 3 mm thick plate.

from the defect at monitoring points 1 and 2 according to Fig. 36(a).

Compared to through-notch results there can be detected a similar variation of the reflection and diffraction coefficient with a notch length but a remarkable drop in amplitude for almost all notch lengths, except for some short and long length defects.

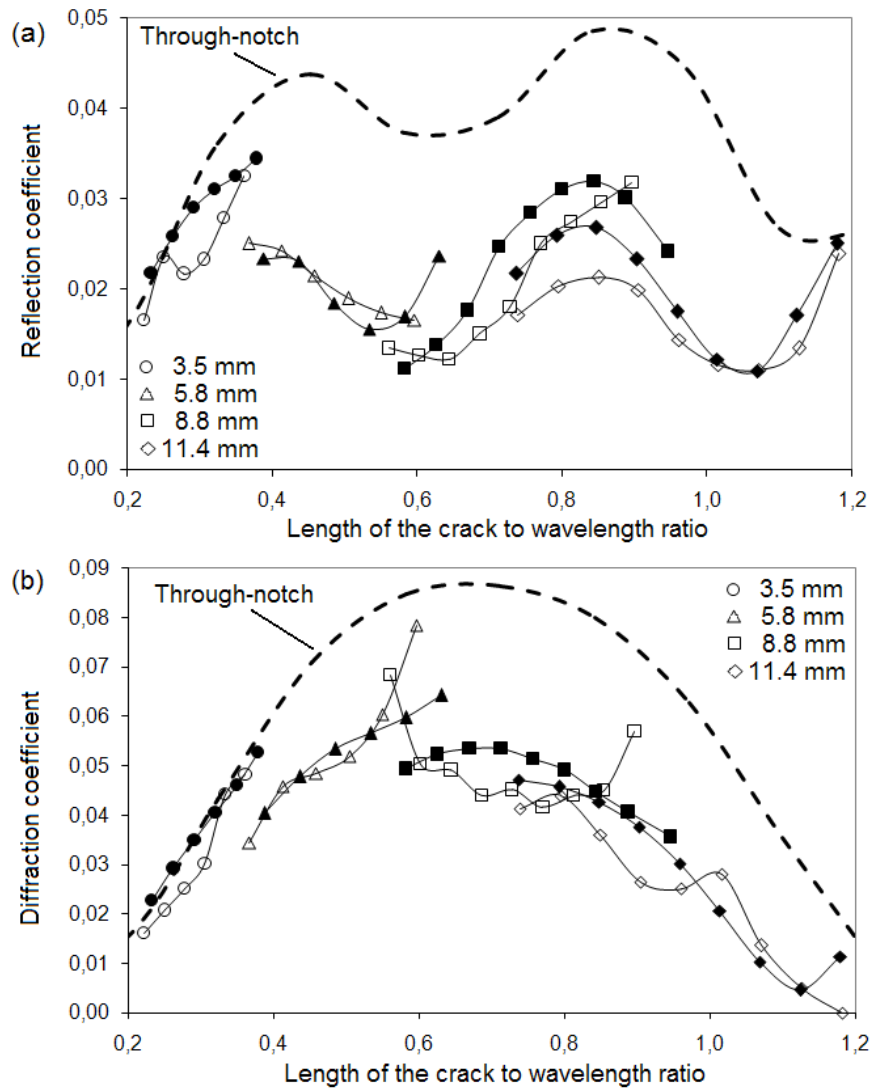


Figure 51. Measured (empty) and predicted (solid) (a) reflection and (b) diffraction coefficients from an 80% and 100% deep (dashed line) notch expressed as a function of ratio of defect length to incident wavelength. Measurements and predictions are made within the frequency range of 200 to 325 kHz.

Besides that, the results are affected by frequency. This is seen as a discontinuity between the results of different notch lengths: higher frequency reflections are stronger than the ones at a lower frequency from notches which values of the scaled lengths are the same. The experimental measurements and FE predictions can be seen to agree well in both cases, except for the diffraction coefficient from an 8.8 mm notch where some of the values of the curves differ significantly. The reason for such discrepancy is not clear but the author believes that it might be caused by a non-ideal shape of the notch which might affect the diffraction. It is not possible to ensure the uneven depth along the entire notch length while machining.

In order to understand the effect of the frequency more clearly, some additional FE modeling was performed. This time a crack geometry was considered. Fig. 52 shows the variation of the reflection and diffraction coefficient with the depth of the crack for different frequencies in a plate with a constant thickness. The normalized crack length was taken as $l/\lambda_{SH0} = 0.7$. It is clear that when the depth of the crack decreases, the amplitudes of scattered waves also decrease in a nonlinear manner. However, it can be seen that if the frequency decreases, the curve becomes increasingly concave, the reflectivity and diffraction at low frequency decreasing markedly. Therefore, this result suggests that it is more difficult to detect shallow defects as the test frequency is decreased.

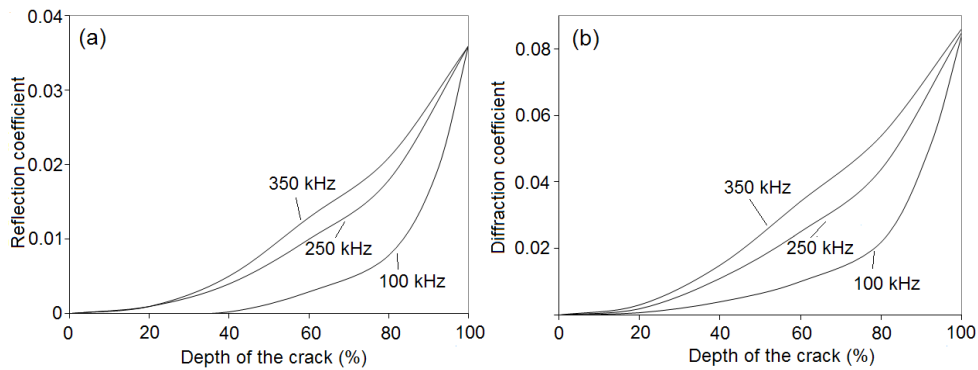


Figure 52. Predicted variation of (a) reflection and (b) diffraction coefficient as the function of depth of the crack normalized to wavelength $l/\lambda_{SH0} = 0.7$. The SH_0 mode was excited at 100, 250 and 350 kHz in a 3 mm thick plate.

Another important parameter that should be considered in the scattering study is the plate thickness. Fig. 53 shows the predicted variation of the reflection and diffraction coefficient with frequency-thickness in the case of an 80% deep crack. The simulations were performed with centre-frequencies 100, 250 and 350 kHz. It can be seen that the reflection amplitude increases almost linearly with the frequency-thickness.

It is also interesting to observe that when the frequency-thickness is similar, the reflection amplitude is also similar. Thus, the results may be applied equally to other thicknesses of plate provided the frequency-thickness is retained.

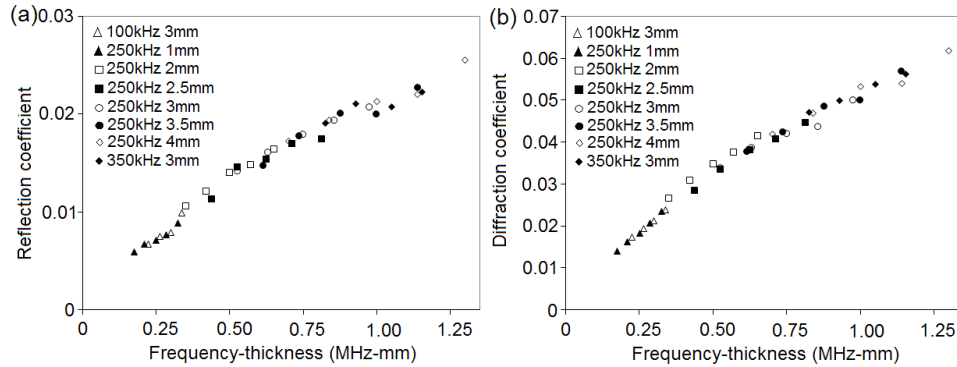


Figure 53. Predicted (a) reflection and (b) diffraction coefficient versus frequency-thickness for 80% deep crack in a plate at $l/\lambda_{SH0} = 0.7$.

3.6 Summary

FE studies, supported by experimental measurements, were performed in order to investigate the nature of the interaction of the low frequency SH_0 wave mode with a narrow notch in a plate, oriented in the wave propagation direction. Both, through-thickness and part-through defects, were considered. Satisfactory agreement between the FE results and measurements was achieved.

The interaction between the wave and the defect was not strong. The scattering field mainly consisted of SH_0 modes, which were reflected in the incident direction and diffracted at 90° to that direction. The study showed that the incident wave is mode-converted at a defect to several types of surface waves which propagate along the crack faces and radiate at the tips of the crack, thus forming a scattered field. The examination of the results has identified the important phenomenon of the interference between the reflections from the near and far tip of the crack, which leads to an undulating shape of the reflection as the function of crack length. The larger delayed far tip reflection was caused by the conversion of the incident mode into Rayleigh type surface waves, propagating along the crack faces.

The interaction of the SH_0 wave with a part-depth crack showed a weakening trend in the scattering when decreasing the crack depth and excitation frequency. It has also been shown that the reflection and diffraction function is depending on the notch width and is characterized by a linear dependence of frequency-thickness.

4 T(0,1) mode interaction with axial crack in pipes

4.1 Background

The aim of this chapter is to investigate the low frequency T(0,1) mode interaction with an axial crack in a pipe. This mode has already been adopted for a guided wave inspection of pipes [3] due to its suitable properties for long range inspection. Similarly to SH₀ wave mode in a plate, this mode is non-dispersive and its incident pulse signals maintain their waveforms and can propagate long distances with small attenuation. Also, at lower frequencies it is the only mode in the torsional wave family that can propagate in the pipe when applying axi-symmetric torsional excitation, thus excluding multimode generation by the transducers. This simplifies the analysis of the signals reflected from the features, which is highly desirable in practical testing.

Like SH₀ mode, the T(0,1) mode has a uniform particle displacement perpendicular to the plane of propagation, and is therefore expected to be sensitive to cracks that are oriented along the propagation direction [85]. Axi-symmetric longitudinal modes can also be used for the detection of cracks in pipes but they have the particle motion entirely in the plane of the propagation and are thus expected to be reflected little by axially aligned cracks [86]. Although some nonaxi-symmetric flexural modes can also be sensitive to axial defects, having a significant circumferential stress field, their dispersive nature and changing wave field along the propagation direction dramatically complicates their exploitation for practical NDT [87]. In principle, it is also possible to use guided circumferential waves for the detection of axial cracks in pipes [88]. However, guided circumferential waves have the limitation that they propagate around the pipe over a small axial extent of the pipe, and cannot be used for long-range inspection.

The research into the potential of using guided waves for the detection of defects in pipes has been intense [1, 3, 43, 44, 58, 59, 61, 62, 64, 65, 78, 85–91]. Quantitative studies [78] of the T(0,1) mode scattering at circumferential notches and cracks have revealed that the reflection coefficient is a roughly linear function of the circumferential extent of the defect. It was shown that when the defect becomes narrower in the circumferential direction of the pipe, its detection possibility decreases. Therefore, defects aligned axially along the pipe have not received as much attention until this time, as they were known to give much smaller reflections than circumferential defects. However, Liu *et al.* [92] demonstrated in their experimental work with the torsional mode that the reflection coefficient at a through-thickness axial notch was more than 15 times larger than its negligible circumferential width should allow, according to previous knowledge. Besides, the reflected signal consisted of a substantial tail the origin of which was not clear. Kwun *et al.* [89] proposed that the interaction is accompanied by the circumferential shear-mode resonance which leads to the generation of regularly spaced decaying signals in the reflection. Such a

scattering mechanism can be understood from the previous chapter where the plate studies showed that the SH_0 mode is scattered remarkably in lateral directions, which in case of the pipe will propagate circumferentially around the pipe and then interact again with the crack.

The aim of this chapter is to determine the reflection coefficients from cracks and notches of a varying depth and axial length when the $T(0,1)$ mode is traveling in the pipe. The results of this study are important to understand the physical nature of the phenomenon and provide some insight into the possibility of detecting and characterizing this kind of defect using ultrasonic guided waves. Finite element models and experiments on a 5 inch diameter pipe were used for this investigation. The report focuses on the analysis of the reflection as functions of length, depth, thickness and diameter of the pipe, and frequency of the incident signal.

The work presented in this part was the result of collaboration between the Department of Mechanics at Tallinn University of Technology and the the Nondestructive Evaluation Group at Imperial College London. It will result in a joint publication [P2].

4.2 Experimental work

Experiments were performed on nominal 5 inch, schedule 120 steel pipes with an outer diameter of 141.3 mm and a wall thickness 12.5 mm. The pipes were 3.7 m long. Fig. 54 shows the experimental set-up. The pipes were supported horizontally on 'v' blocks which had a negligible effect on the wave propagation behavior in the pipe. A milling machine was aligned so that an axial slot could be cut along the axis of the pipe, and the axial position of the cut was changed by simply moving the pipe along its axis. This enabled the cutting of the axial notches in an accurate fashion without having to disturb the guided wave instrumentation. The cut was started 1.8 m from the end of the pipe, where the transducers were located and extended away from it. Experiments were conducted on two separate pipes, using the following notches: a) a through thickness notch; b) an 80% deep notch. The notches were 3 mm wide and their length was increased incrementally in steps of 8 mm from 8 mm up to 120 mm. Due to the shape of the cutting tool the ends of the notch were rounded and the part depth notch was flat-bottomed.

The torsional $T(0,1)$ mode was generated by clamping a transducer ring at one end (end A) of the pipe, as shown in Fig. 54. The transducer ring was produced by Guided Ultrasonics Ltd [93]. The ring is made up of two rows of piezoelectric transducer elements [90], each consisting of 16 elements spaced uniformly around the circumference. The elements impart tangential force and are oriented in such a way as to act in the circumferential direction around the pipe. This means that only the $T(0,1)$ mode is excited [3]. The contact between the transducers and the pipe was dry and no pipe surface cleaning was performed. Although in usual practice it is

possible to control the directionality of the generated waves, by controlling the phase difference between the two rows, this was not necessary in this test, because the ring was at the end of the pipe, so all the transducers were excited simultaneously.

The equipment used to generate and receive the signals was a Guided Ultrasonics Ltd. Wavemaker G3 instrument. The test signal was 5 cycle tone burst modulated by a Hanning window. For each crack length, the center frequency of excitation was varied from 20 kHz to 65 kHz in increments of 5 kHz. In order to obtain a reference measurement, reflections from end B were recorded before any milling was done. As the signals reflected from the notch were in general quite weak, the quality of each measurement was enhanced by taking 256 averages and applying a band pass filter.

By summing up all the received signals of the transducer elements it was possible to monitor just the reflected T(0,1) mode [44] and ignore mode converted signals reflected at the crack. The reflection coefficient for each crack length was calculated in the given time domain. This was done by calculating the envelope of the time signal, by taking a Hilbert transform, then simply dividing the value of the reflection peak by that of the end-wall reflection peak which had been recorded in the undamaged pipe. Since the signals are fairly narrow-band, this approach gives a reflection coefficient which is sensibly representative of the center frequency of the signal.

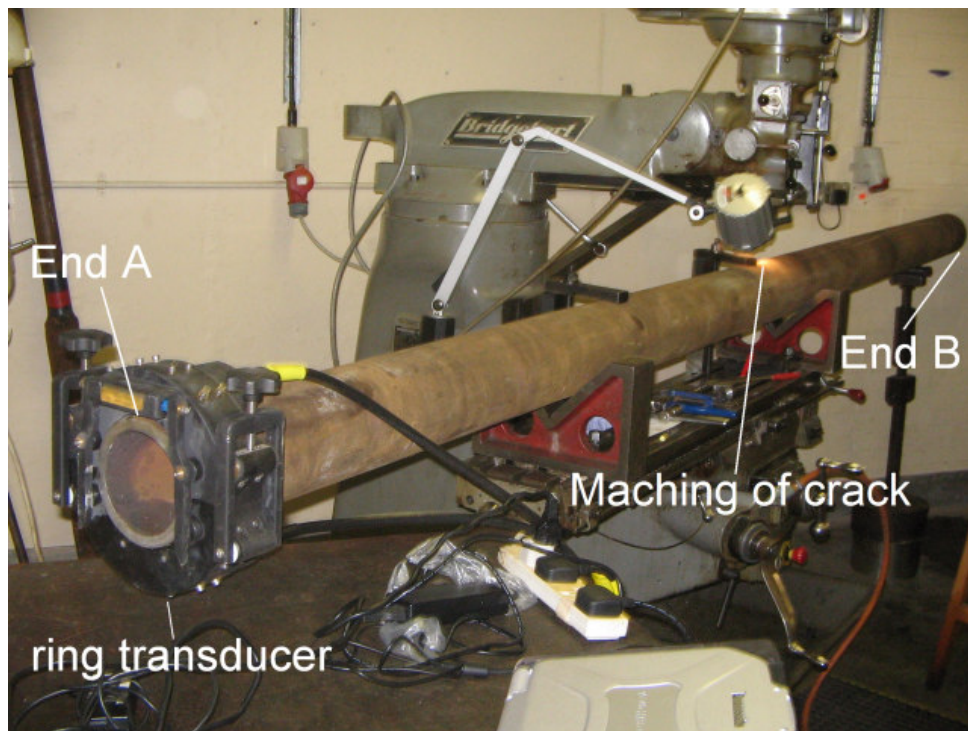


Figure 54. Experimental setup of pipe testing.

4.3 Finite Element modelling

4.3.1 The membrane model for through-thickness axial crack

The interaction of the T(0,1) mode with circumferential cracks and notches in pipes has been successfully studied in the past using the Finite Element (FE) method [78]. A similar study was performed here to predict the scattering at an axial through-thickness crack, using the ABAQUS software with its explicit time stepping procedure [42]. The geometry of the pipe model was discretized using two-dimensional membrane elements, assuming a plane stress condition in the pipe wall. This approach has already been shown to work well to model the extensional and torsional behavior of the propagating modes around the frequencies at which the experiments were performed. However, it is not possible with this approach to simulate modes in which there is a local bending of the pipe wall, nor to model part-through notches.

A mesh of identically sized linear (four noded) quadrilateral membrane elements was used. The models of the 5 inch pipe represented a 3.7 m length, using 925 elements along the length and 128 elements around the circumference. As a result each element was 4 mm long and 3.16 mm wide around the circumference corresponding to about 12 elements per wavelength at the highest frequency used, respecting the spatial discretization limit required for accurate modelling. Additionally, some larger radius pipes were modelled by using more elements with the same element dimension along the circumference. Zero-width cracks with zero stress on edges were modelled by disconnecting adjacent elements. Notches with nonzero width were introduced by removing elements from the model; the notches were, therefore, rectangular in shape.

The axi-symmetric torsional mode T(0,1) was generated by prescribing identical tangential displacement time histories at all nodes at the end A of the pipe. The central frequency of the tone burst varied from 15 to 65 kHz. The detection of reflected waves was achieved simply by monitoring circumferential displacements at 16 nodes, simulating the receivers, around the circumference at the end A of the pipe. The reflected T(0,1) mode was obtained by summing all the received signals, and the reflection coefficient measurements were performed in the same way as in experiments. Some results were also obtained by measuring the nodal displacements around the pipe at a location between the excitation end of the pipe and the defect.

4.3.2 3D model for part-through axial crack

The whole volume of the pipe was discretized using 8-node "brick" elements. Each node of the element has three degrees of freedom (displacements in x; y; z directions) and such elements permit a full 3D vibration analysis of the pipe. Although this approach enables the modelling of real part-thickness notches, it is computationally expensive due to the large number of elements.

The 3.7 m long pipe was modelled with 925 elements along the length, 128 elements around the circumference, and 5 elements through the wall thickness. Both cracks and finite width notches were modelled 80% deep through the wall thickness. The width of the notch varied through the thickness of the pipe wall, being 3.46 mm wide on the surface of the pipe and 2.96 mm wide at the bottom of the defect. Excitation and monitoring locations were arranged similarly to the membrane model.

4.4 Results

4.4.1 Through-thickness notch (membrane models)

The results from the experimental data and FE simulations are presented. Typical time records from the experiment and simulation are shown in Fig. 55(a,b). Both of these records are for a 5 inch pipe with a notch of 56 mm in axial extent, and for a 5-cycle T(0,1) mode incident at 35 kHz. The results are normalized to the maximum absolute displacement value of the end-wall reflection. The figures show clearly the initial tone burst on its way towards the notch and then the reflected T(0,1) mode at the defect and at the pipe end. Interestingly enough, the reflection consists of a series of pulses with gradually decaying amplitudes. In this example these pulses are spaced with a period which is approximately equivalent to the duration of the shear wave pulse passing the circumference of the pipe. Such behavior is caused by the diffraction at the notch, as was shown in the previous chapter for fundamental shear mode interaction with the crack in a plate. The resulting scattering consisted of the direct reflection and diffraction which was composed of ultrasonic shear waves propagating in both directions perpendicularly to the crack alignment. Similarly, such waves are generated in the present case which propagate circumferentially around the pipe and subsequently interact repeatedly with the crack, giving characteristic echoes after the first reflected pulse. This phenomenon affects the time-domain amplitude of the final reflection, if the pipe is sufficiently small in diameter, and the tone burst is too long that overlapping of signals can occur.

It can also be seen from the results that there is a small time shift between the two records and that the generated and reflected wave packets in the experimental measurements are slightly wider than those in the FE data. The reason for this comes from the design of the transducer ring. It has two rows of transducers which are set apart by a specific distance, so one of the rows is slightly away from the end of the pipe. When this ring is excited, there is an additional delayed reflection at the near end of the pipe which distorts the shape of the incident signal. Also, we can see that the back-wall reflection is significantly larger in amplitude than the incident signal. This is due to the doubling of the displacement amplitudes as the measured displacements incorporate both incoming and reflected wave fields at the end A of the pipe [23].

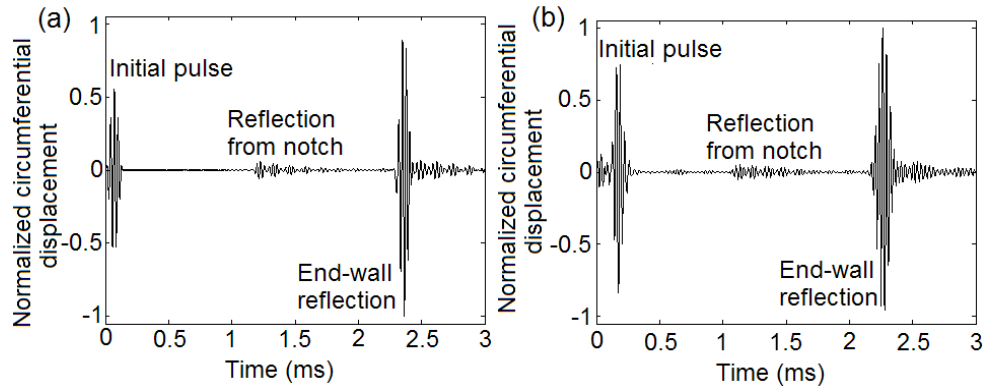


Figure 55. Predicted FE (a) and experimental (b) time record for a 5 inch pipe with a 56 mm axial notch, and a 5-cycle T(0,1) mode incident at 35 kHz.

The variation of the T(0,1) reflection coefficient with axial length l of the notch normalized to incident wavelength λ is shown in Fig. 56 at 30, 35 and 40 kHz. In general, the agreement between the FE and experimental results is good. The differences between the results can be accounted for by the presence of noise. Very small signals are being examined and the small deviations in an experimental set-up can cause a small noise level. The reflection coefficient has similar features to that of the plate case from the previous chapter. The predicted FE curve has small characteristic peaks and troughs which are due to interference of reflection components at the tip and at the far end of the notch which are not separable in the first dominant reflection of T(0,1).

Fig. 57 shows the predicted T(0,1) reflection coefficient versus axial length of the crack normalized to the incident wavelength for a wider range of incident frequencies. If we consider a specific normalized crack length value, we observe that the reflection ratio decreases when the frequency increases. This is not consistent with the previous plate results, from where it is known that the reflection coefficient does not depend on the operating frequency when the crack length is similarly scaled to the wavelength of the incident wave for those frequencies. In the plate study the waves were excited and monitored at a single point along the crack alignment, and the signals were beamcompensated. However, in the pipe case the reflection from a crack spreads around the pipe and the reflection coefficient is calculated by summing all the amplitudes of the received waves, measured at the pipe circumference. Recently, an approximate relationship between the pipe mode and plate solutions was derived [91] and it was shown that pipe mode amplitudes are related to plate amplitudes by the law of inverse square root of frequency. The reduction in frequency can be also seen in the figure.

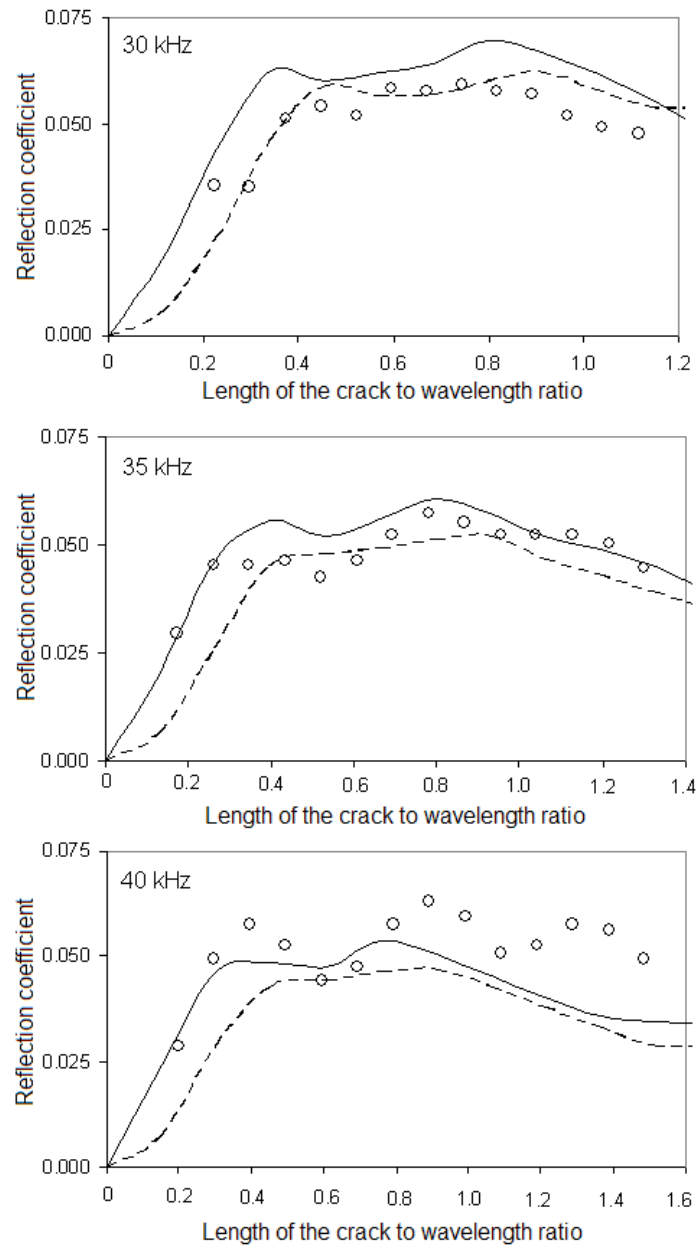


Figure 56. Variation of the reflection coefficient with the length of the notch normalized to wavelength for a 5 inch pipe and T(0,1) mode incident at 30, 35 and 40 kHz; (ooo) - experiment, (solid line) - FE membrane model with a notch, (dashed line) - FE membrane model with a crack.

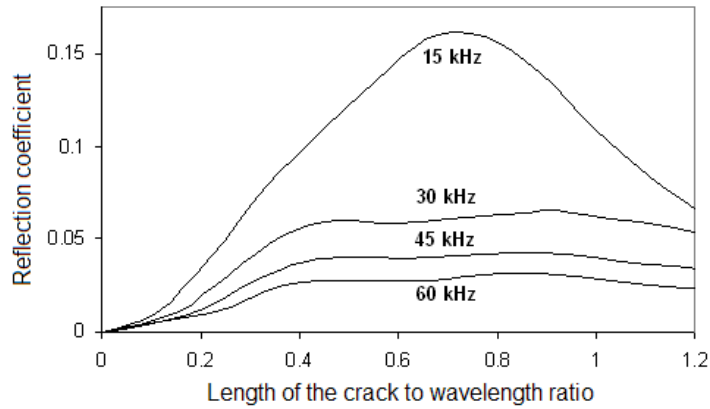


Figure 57. Variation of the reflection coefficient with the length of the crack normalized to wavelength at various frequencies for a 5 inch pipe.

Another difference between the curves in Fig. 57 is the remarkable increase in the reflection coefficient of the 15 kHz result, compared to the plateau region, exhibited by the higher frequency curves. This is due to a resonance of the different wave packets reflected at the crack. As the excitation signal was a 5-cycle tone burst, and the circumferential extent of the pipe is slightly less than 2λ , there is an overlapping between the prime reflection, and the reflections induced later by circumferential waves interacting with the crack. Furthermore, the lateral scattering, and thus the interaction of the circumferential waves with the crack, is the strongest at crack dimensions around $l/\lambda = 0.7$ [71].

Fig. 58(a) shows a normalized FE time signal for a 5-cycle T(0,1) wave reflected from a 36 mm long zero-width notch at 45 kHz. The signals were monitored at 1.4 m from the pipe end A. Its magnitude of reflection coefficient in Fig. 58(b) was calculated by dividing the magnitude of the Fourier transform of the full reflected signal by that of the incident signal. Note that there are two horizontal axes (frequency and normalized circumference) in the figure. It is interesting to observe that, it is not a smooth function of the frequency as was found for circumferential through-cracks in pipes [78], but there are regularly spaced peaks in the spectrum. These peaks are due to resonance of the consecutive wave pulses reflected at the crack. The interpretation of this can be understood by observing the reflection coefficient as a function of the circumference l_c of the pipe, measured in wavelengths of the tone. It can be seen that the maxima of the reflection coefficient spectrum occur almost at the frequencies corresponding to integer wavelength values around the pipe circumference. Consequently, constructive interference occurs at those wavelengths, when the reflections are an integer number of cycles behind the leading reflection. However, the results indicate that these maxima do not occur exactly at an integer number of wavelength values but at slightly smaller values. The reason for this is not known, but it is

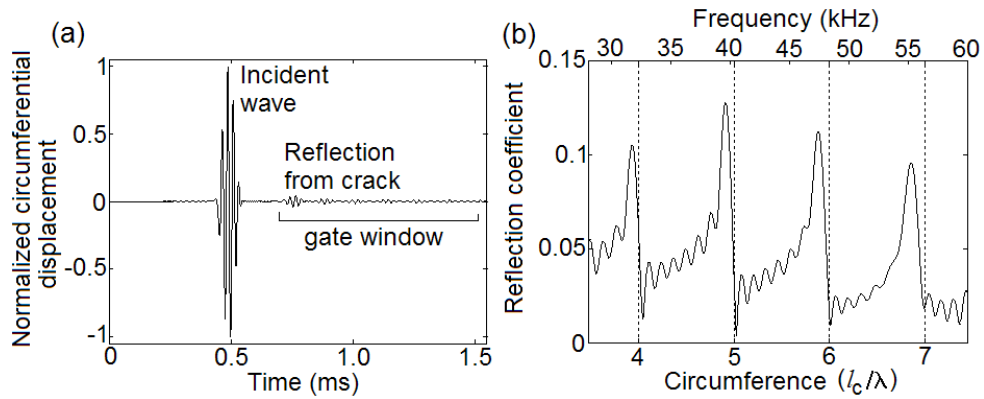


Figure 58. Results for a 5-cycle T(0,1) mode incident at an axial crack $l = 36\text{mm}$ ($l/\lambda = 0.524$): (a) predicted FE time record and (b) reflection coefficient as the function of frequency and pipe circumference for 5 inch pipe at 45 kHz.

believed that this is probably due to a phase delay when the circumferential waves are reflected at the crack, giving the appearance of lengthening the propagation path. The revealed peak-like nature of the signal can be a clear indicator of the presence of an axial crack.

Fig. 59 shows the prediction for the reflection coefficient versus the circumference of the pipe for a specific case of a 36 mm long crack and a 5-cycle T(0,1) tone burst with center frequency of 45 kHz. Both the time-domain (solid line) and frequency domain (dashed line with circles) reflection coefficients are shown. The time-domain reflection coefficient decreases smoothly along with the increase in the pipe circumference, except at low pipe circumference values, where the curve oscillates. Most of the curve is smooth because the time domain amplitude is given only by the peak of the first arrival wave packet, without interference from later packets. The irregularity at a low frequency is because there is overlapping of the subsequent reflected wave pulses from the crack. Closer examination shows that the amplitude of the reflection is inversely proportional to the pipe circumference which is consistent with the data above [91]. The overall reduction in the reflection coefficient with increasing circumference means that it is more difficult to detect the crack of the same length in larger radii pipes at the same testing frequency. As expected, the frequency domain results oscillate with the variation of pipe circumference. The reason for this was explained in Fig. 58. The frequency spectrum incorporates the summation of the amplitudes of all the waves reflected at a crack which may, at certain pipe circumferences, be in phase, having maxima in the frequency spectrum, or being out of phase and causing reduction in the amplitude in the final spectrum.

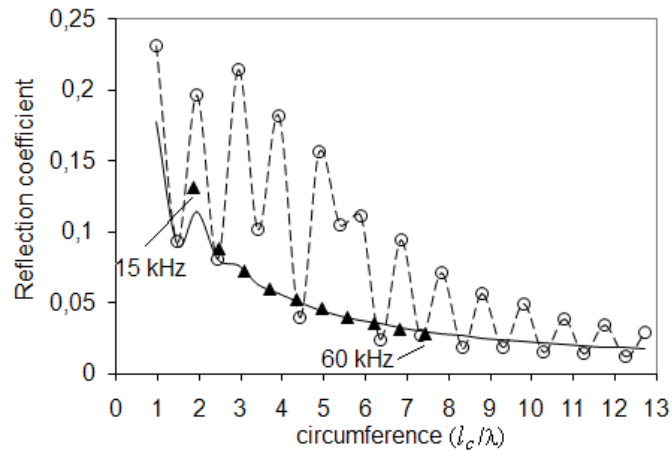


Figure 59. Variation of reflection coefficient with circumference: (solid line) - time domain values at 45 kHz, (dashed line) - frequency domain values at 45 kHz, (solid triangle) - values at 15 to 60 kHz for a 5 inch pipe.

An interesting correlation is observed in the time-domain results if we replot the reflection coefficients using different incident frequencies and the same normalized crack length. Fig. 59 shows that the reflection coefficient values, which are obtained for a 5 inch pipe at frequencies from 15 kHz to 60 kHz (solid triangle), agree with the above 45 kHz results, if the circumferences are similarly scaled. This means that, in the studied frequency range for a given normalized circumference and normalized crack length, the reflection has the same amplitude whatever the frequency is. For example, if the pipe diameter is 125 mm, the reflection amplitude from a 62 mm long crack at 30 kHz, will be approximately the same as that for the pipe with the diameter of 75 mm and a 37 mm long crack at 50 kHz.

4.4.2 Part-thickness notch (3D model)

A typical FE time trace showing the interaction of a 35 kHz 5-cycle T(0,1) mode with a 56 mm long and 80% deep notch is presented in Fig. 60. The reflection at the notch is hardly noticeable, and its amplitude is around half the size of the reflection amplitude of the through thickness notch of the same length. This means that the variation of the amplitude is not linearly related to the variation of the depth of the notch. Such behavior was observed in the previous chapter for the SH₀ scattering from a part-thickness crack and notch in a plate. As the T(0,1) is closely related to the plate SH₀, some scattering aspects for the pipe case have the same explanation. Moreover, an approximate relationship between the solutions for plates and pipes exists [91]. Fig. 52 demonstrated that the reflection coefficient for a plate is decreasing in a non-linear manner, when the depth of the crack decreases.

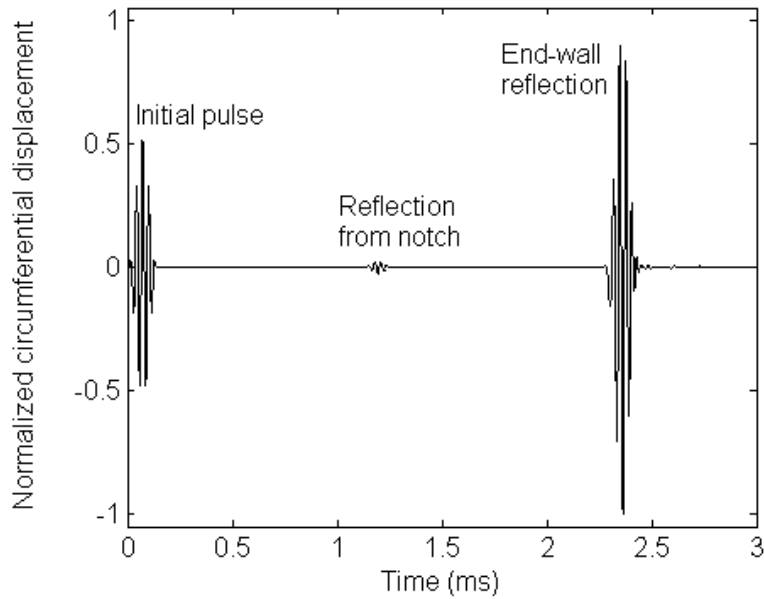


Figure 60. Predicted FE time record from 56 mm 80% deep axial notch at 35 kHz for a 5 inch pipe.

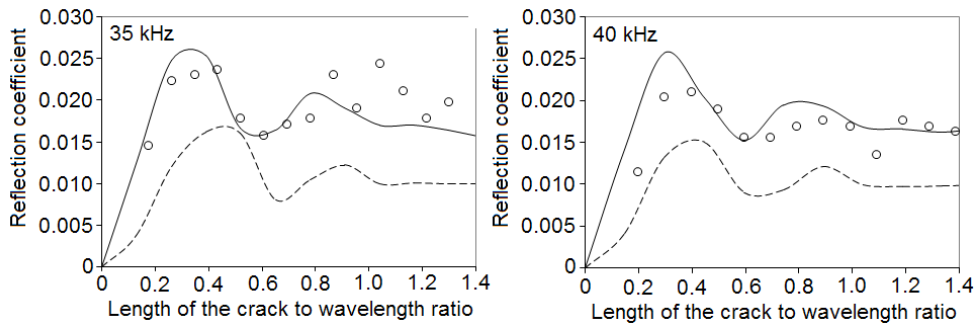


Figure 61. Variation of reflection coefficient with a length of the 80% deep notch normalized to wavelength at 35 and 40 kHz for a 5 inch pipe; (ooo) - experiment, (solid line) - 3D model with a notch, (dashed line) - 3D FE model with a crack.

The variation of the T(0,1) reflection coefficient with a normalized notch length from the 80% deep notch is shown in Fig. 61 at 35 and 40 kHz. Although the amplitudes of the reflected signals were very small, the agreement between the experimental and FE notch model results is quite satisfactory. Here it is important to note that the width of the notch affects the reflection strength substantially. It is clearly seen that the reflection from the crack in a pipe is much smaller than from a finite

width notch at all defect lengths. Again, this is a similar result to the one found for the scattering from a part-thickness crack and notch in a plate.

Fig. 62 shows FE predictions of the variation of the reflection coefficient with a normalized crack length for a wider range of incident frequencies. We can see that the maximum reflection strength is slightly weaker for higher frequencies. Compared with the through-crack results in Fig. 57 it can be seen that the reflection strength has dropped drastically, especially for low frequencies. The plate results in Fig. 53 showed that the reflection amplitude for part-thickness cracks decreases with the decreasing frequency-thickness product parameter which also occurs here in case of the pipe.

Finally, the similarity between the reflections of the incident pipe $T(0,1)$ and plate SH_0 mode from a crack, is shown. In Fig. 63 the frequency-domain plate reflection coefficient results are compared with the time-domain pipe results. The FE predictions have been obtained for 60% and 80% deep cracks and are normalized to the reflection amplitude of the through-thickness crack. It can be seen that the results are close. Therefore, it is reasonable to use the plate results for the pipe analysis. Another important observation from the figure is that at varying crack lengths, variation of reflection strength with the depth is different. This means that it is not possible to obtain the unique scale factor, which links the reflection amplitude from a part-thickness crack, by knowing that from a through-crack of the same length, because in general the effects of the length and depth of the crack on the scattering process are coupled [83].

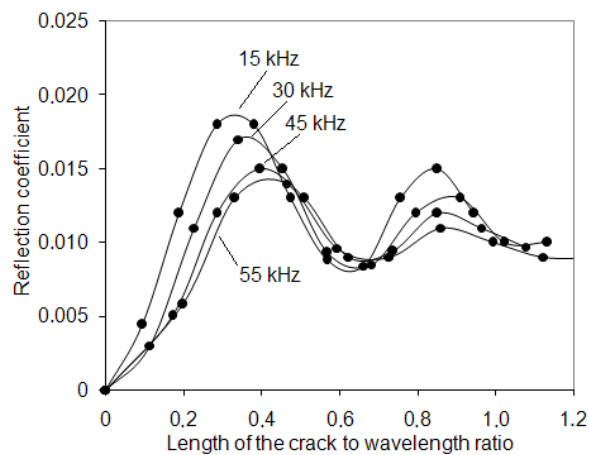


Figure 62. Variation of reflection coefficient with length of the 80% deep crack normalized to wavelength at various frequencies for a 5 inch pipe.

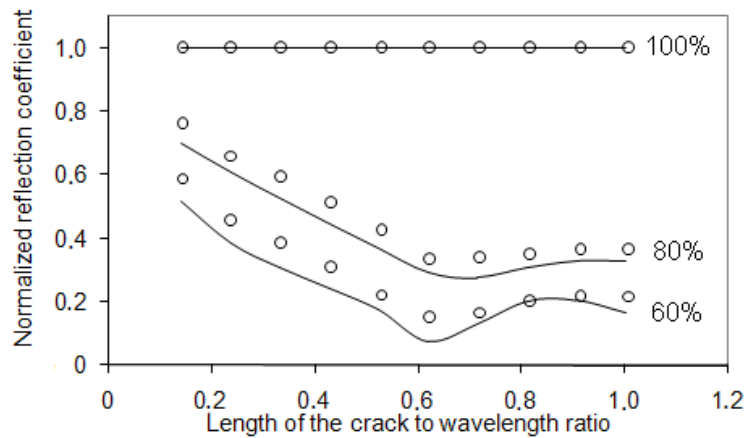


Figure 63. Predicted variation of normalized reflection coefficient with the length of crack normalized to wavelength for 60% and 80% deep cracks. (solid line) - plate FE results, (ooo) - pipe FE results; waves were excited at 250 kHz and the thickness of the structure was 3 mm.

4.5 Discussion

The aim of this chapter is to provide an insight into the possibility of detecting and characterizing axially aligned cracks in the wall of a pipe. As it has been observed above, the interaction of the torsional mode with an axial crack was influenced by several parameters: crack length, crack depth, frequency-thickness and diameter of the pipe. Furthermore, in practice we have to deal with the cracks the geometry of which is much more complex compared to the idealized straight-edge crack model used in this study. Nevertheless, some generalizations can be made with this idealized crack model and some limits for practical testing concluded. The results showed two important trends. On the one hand, the study of through-thickness cracks showed that lower frequencies allowed the acquisition of larger reflections, as was seen in Fig. 57. On the other hand, investigating reflections at part-depth cracks in plates, it was observed that as the frequency-thickness value decreased, so did the reflection amplitude, shown in Fig. 53. Therefore it is important to discuss where to make the compromise using different frequencies for different pipes with different crack lengths. In the following part we will find the reflection coefficients for an axial through-crack in a specific defined pipe at all axial extents using FE, and will then introduce approximation formulas to generalize the results for other pipe sizes. The collection of reflection coefficients of the part-depth cracks in a plate helps us to estimate the reflection strength of similar defects in pipes.

4.5.1 The effect of frequency and pipe circumference in case of a through-thickness crack

According to Velichko *et al.* [91], the reflection coefficient from a fixed sized defect is inversely proportional to the pipe radius. Thus, for any pipe circumference, the reflection coefficient R at a given crack length and frequency can be approximated with the formula:

$$R = R_0 \frac{l_{c0}}{l_c}, \quad (42)$$

where R_0 is the reference reflection coefficient for a pipe, with the reference circumference l_{c0} , and l_c refers to the circumference of pipe under investigation.

From equation (42), we can see another useful relation if the circumference is given in terms of incident wavelength, which is related to the frequency. This links reflection coefficients R for different incident frequencies at a given pipe circumference and a normalized crack length:

$$R = R_0 \frac{f_0}{f}, \quad (43)$$

where R_0 is the reference reflection coefficient for a pipe with the reference incident frequency f_0 and f is the required test frequency.

The advantage of the relations (42, 43) is that they enable us to calculate reflection coefficients for all crack lengths at different frequencies and pipe circumferences if the reflection coefficients for all crack lengths from a specific pipe size are known. An example which shows sensitivity limits for practical testing for a clean pipe is given in Fig. 64 where the contour curves for 2% reflection coefficients for different pipe sizes are shown. In this case, the reference reflection coefficients are defined for a 5 inch schedule 80 pipe. We limit our study to the lowest frequency $f = c_{ph}/2\pi r$ (r is the mean radius of the pipe), in which case the wavelength corresponds to the pipe circumference. As expected, it is possible to detect shorter cracks in smaller diameter pipes and also, as the pipe size grows, the highest frequency that can be used decreases. Another observation from this figure is that higher frequency waves are more sensitive to shorter cracks, but the increase in sensitivity is rather slow. For example, in the case of a 5 inch pipe, even if the frequency increases by a factor of four, it is only possible to detect cracks that are half as long.

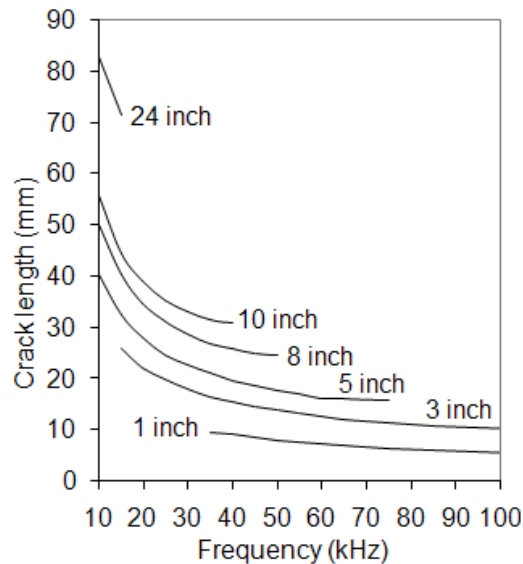


Figure 64. Variation of the crack length with a frequency for reflection amplitude 2% from incident wave amplitude for schedule 80 pipes; results derived from FE 5 inch pipe membrane model.

4.5.2 Estimating the smallest detectable crack depth

Evaluation of the maximum depth of a defect is one of the main targets in pipe inspection. It was demonstrated that the reflection coefficient from an axial crack of a given length increased monotonously with depth at all frequencies, but the variation was not monotonous over the observable range of crack length, as was shown in Fig. 62. Therefore, the appropriate selection for maximum sensitivity would depend on the crack length. In the studied cases, the highest sensitivity could be established when the crack length-incident wavelength ratio was between 0.2 and 0.5 but, in general, the exact value also depends on frequency and pipe dimensions.

From the findings in Section 4.5.1, we propose that a simplified analysis for the crack depth estimation may be achieved by using combined results from the plate and pipe models. An interesting outcome was that the scattering strength at a part-depth crack in a plate can be scaled to frequency-thickness, and reflection amplitudes at a crack can be approximated with the results from the FE plate model. Therefore, by obtaining the normalized reflection amplitudes for different crack depths and lengths at a specific frequency-thickness value from a plate model, it is possible, by using additionally the equations (42, 43), to derive the reflection amplitudes for different pipe sizes having the same frequency-thickness. It is also possible to derive the result

by using the theory in Ref.[91].

Such a study was performed by modeling 3 mm thick plates with 60, 80 and 100% deep cracks. The SH_0 mode was excited at 60, 100, 200 kHz and the normalized reflection coefficients at different crack lengths were obtained in the frequency domain. The additional frequency-thickness data points were obtained by making use of the full width of the spectrum of the signal, so that the frequency-thickness range 115...800 kHz-mm covered most of the studied pipe cases. At each frequency-thickness product value, the reflection coefficients for different crack depths were obtained by an approximate third-degree polynomial fit through the coefficient values at crack depths 60, 80 and 100%. Thereafter, reflection maps showing the reflection coefficient with varying crack depth and length for each specific pipe case at a fixed frequency were created.

Fig. 65(a) shows a 3D plot of the reflection coefficient for T(0,1) at 35 kHz incident on an axial crack of a varying depth and axial length. The results are obtained for cracks with normalized lengths up to $l/\lambda = 0.6$, where the highest sensitivity to crack depth is expected to occur. In Fig. 65(b), the contour curves of this 3D plot show that the satisfactory sensitivity to axial cracks can be achieved only for very deep cracks. Furthermore, it can be seen that the sensitivity is similar for various crack depth and length combinations, which means that it is not possible to extract both dimensions from the measurement of a single reflection coefficient; this makes the evaluation of the crack parameters impossible. However, it is possible to suggest the crack length for which the sensitivity is the highest at a given frequency. For example, in this studied case the shallowest crack with the reflection coefficient of 2% can be detected, when the crack is 40 mm long. Similar analysis was also performed for other frequencies and pipe sizes, and the results are shown in Fig. 65(c). There is a clear trend for all pipe sizes showing that the detectable crack depth increases and crack length decreases with the increase in frequency. Therefore, in practice it is useful to test the pipe at several frequencies, as the crack length is not known.

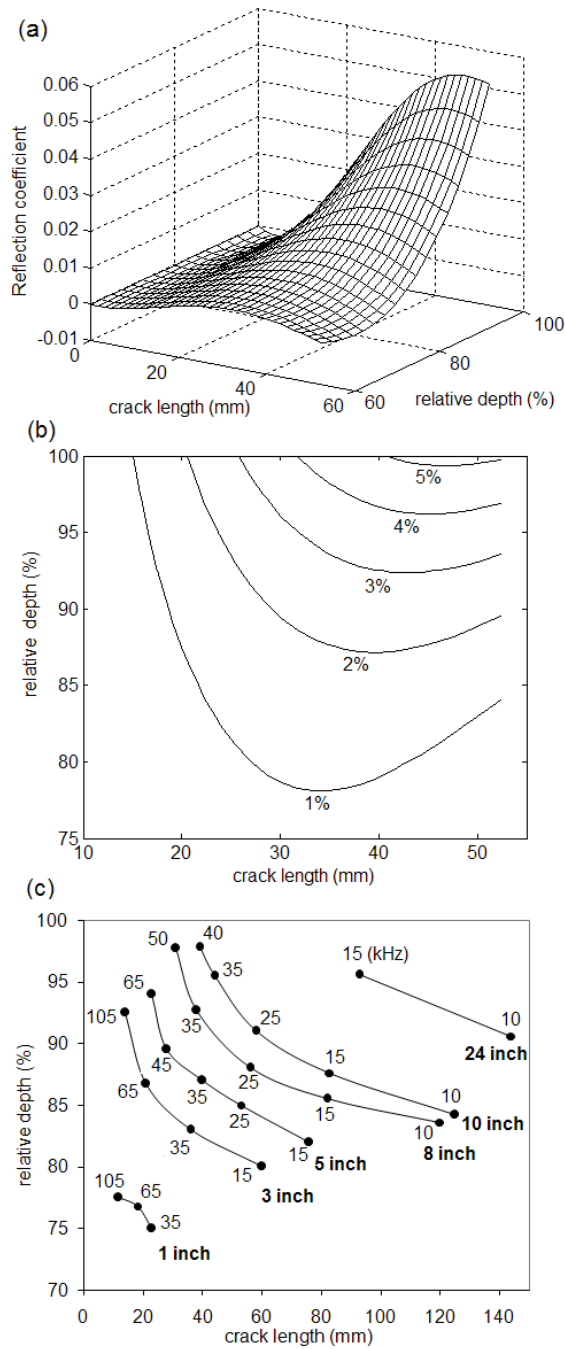


Figure 65. Results for schedule 80 pipes and T(0,1) mode incident: (a) 3D graph of reflection coefficient from axial cracks with varying depth and length and (b) contour curves of reflection coefficients 1, 2, 3, 4 and 5% at 35 kHz in a 5 inch pipe; (c) variation of the crack length with depth and frequency for a reflection amplitude of 2% from incident wave amplitude for various pipe sizes, results are derived from the FE 5 inch pipe membrane model.

4.5.3 The effect of the crack shape

So far the work has described wave scattering at a perfect straight-edge notch or a crack. It was shown that the reflection from a part-thickness notch was stronger than the one from a part-thickness crack. However, in practice these two cases rarely occur, and the shape of the defect can be much more complex having irregularly shaped surfaces and varying depth along its axial extent, and, therefore, the scattering might be different. The influence of the crack shape on the scattering is studied by using the FE modelling, the depth variation is not considered. Two different cracks (a) and (b) with constant depths of 80% and 100% of wall thickness were modelled by disconnecting the nodes following the regular square grid on the pipe surface, as shown in Fig. 66(a,b). Both defects are oriented along the pipe axis and are characterized by their width w in the circumferential direction of the pipe. These shapes do not cover all the cases met in practice but still such a crude approach can illustrate what happens with the reflection. Fig. 66(c) shows the time-domain reflection coefficient as a function of the crack width w from a 24 mm long crack. The excitation was a 5 cycle tone burst at 45 kHz. It can be seen that the reflection amplitude increases with the crack width w in both crack cases suggesting that randomly shaped axial defects with a non-zero circumferential extent can more easily be detected than the zero-width cracks. This trend was also confirmed for all the other frequencies from 15 to 60 kHz. Therefore, it is reasonable to assume that the zero-width crack is a good limit for the minimum sensitivity.

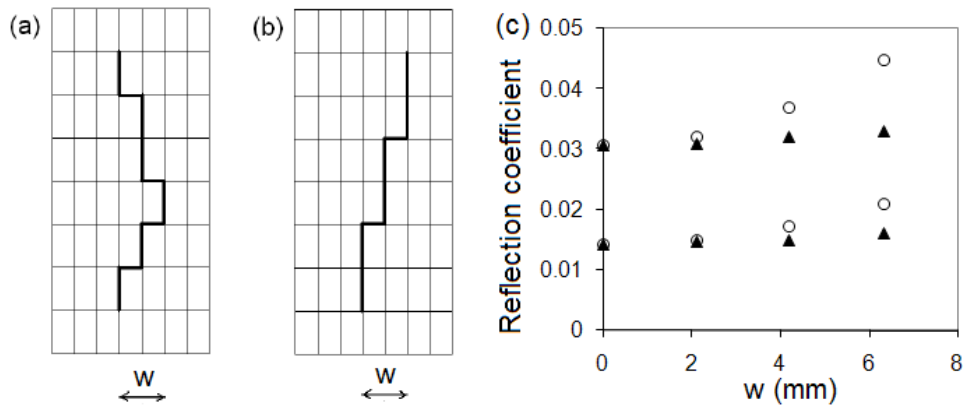


Figure 66. Schematic representation of irregularly shaped cracks (a) and (b). (c) Variation of reflection coefficient with a crack circumferential width w for the 24mm long and 80, 100% deep crack. The results are for T(0,1) incident at 45kHz in a 5 inch schedule 120 pipe. (empty circle) - crack (a), (solid triangle) - crack (b).

4.6 Summary

This chapter dealt with the scattering of the fundamental torsional mode by an axially oriented defect in a pipe wall.

The FE simulations, confirmed by experimental measurements for selected cases, provided a useful collection of reflection coefficient results at notches of various lengths and depths. Furthermore, the examination of the time signal identified an interesting phenomenon of the series of wave pulses with a gradually decaying amplitude reflecting from a defect, which led to a periodic peak-like structure in the frequency spectrum. The phenomenon was found to be due to the diffraction at a notch which then, propagating in the circumferential direction, interacted repeatedly with the notch, giving additional echoes. Thus the axial notch could be identified by the occurrence of the peaks in the frequency spectrum. It was shown that the time-domain reflection coefficient increases with the crack length at all frequencies but finally reaches an oscillating regime. The reflection behavior for a through-thickness crack can be normalized to account for the crack length, the pipe circumference and excitation frequency. Thereby at a given frequency and crack length the reflection decreases with the increase in pipe circumference.

The examination of the reflection coefficient as a function of crack depth demonstrated that the reflection strength decreases substantially with the decrease in the crack depth. The three-dimensional plate study allowed to show that the sensitivity for a given crack length drops with the decreasing frequency-thickness product. However, in the pipe case the higher frequency reflection strength suffers from beam-spreading of reflected waves to a larger area of the pipe. The results demonstrated that the torsional wave is capable of detecting defects which are deeper than 75% of the wall thickness, if the noise level is very low. The sensitivity to defects is dependant on frequency, whereby higher frequencies are more sensitive to deeper cracks, though the crack length also influences the detectability. Therefore, in practice, it is reasonable to test at more than one frequency to avoid missing the defects due to the unknown length of the crack. The results were shown for various pipe sizes.

5 Conclusions

5.1 Summary of findings

In this thesis the effects of geometrical discontinuities on the propagation of guided waves in plates and pipes were investigated.

In chapter 2, a numerical method based on normal mode expansion (NME) technique was employed for the analysis of axi-symmetric longitudinal wave interactions with features in a pipe. This study brought new insights into the characterization of wave propagation in thick pipes where the plate analogy cannot be used any more. The curvature effect on the wave propagation was investigated in two examples. Firstly, the interaction of the compressional type $L(0,2)$ mode with a free edge demonstrated that there exists resonance of the pipe edge similar to that of incident S_0 mode in a plate. The NME study highlighted the importance of nonpropagating and inhomogeneous modes in the resonance generation mechanism. It was found that with increasing thickness to the medium radius ratio, the pipe results will increasingly differ from those of the plate. This was due to the changes in the wave field of the incident wave which led to the weakening of the resonance. Both Finite Element (FE) simulations and experimental measurements validated the main predictions. Secondly, the interaction of the $L(0,2)$ mode with surface breaking circumferential cracks was examined. It was shown that sensitivity to outer surface cracks, compared to inner cracks, increased gradually with the increase in the wall thickness of the pipe.

A study of the scattering of the SH_0 mode from a defect was presented in chapter 3. FE simulations and experimental measurements showed that SH_0 mode is sensitive to a crack which is aligned in the direction of the propagating mode. This is due to its wave field which is perpendicular to crack orientation. The scattered field at the crack consisted of the SH_0 modes, which were reflected in the incident direction and diffracted at the lateral directions. The results revealed an undulating shape of the reflection amplitude as the function of defect length. The influence of different surface waves, propagating along the defect faces on the scattering, was explained. The scattering weakened when the crack depth or excitation frequency was decreased. The study on SH_0 in a plate was an effective starting point for a more complicated analysis of reflection from similar defects in pipes.

In chapter 4, a systematic analysis of effect of pipe size, defect size and excitation frequency on the reflection of the $T(0,1)$ mode from axial defects in a pipe was carried out. As an interesting phenomenon, a series of wave pulses reflected from a through-thickness crack, was observed in a time signal. This was due to diffraction at a notch which then, propagating in the circumferential direction, interacted repeatedly with the crack, giving additional echoes. Its spectrum showed a strong frequency dependence which could be an indicator of such defects. The reflection behavior in

the time-domain for a through-thickness crack can be normalized to account for the crack length, the pipe circumference and excitation frequency. Thereby, at a given frequency and crack length, the reflection decreases along with the increase of pipe circumference. The examination of the reflection coefficient as a function of crack depth demonstrated that the reflection strength decreases substantially along with the decrease of the crack depth. The maps of reflection coefficients, as a function of crack length and depth, showed that the evaluation of both parameters is not possible. The study showed that the torsional mode is capable of detecting very deep axial cracks.

5.2 Recommendation for future research

The topic on the interaction of guided waves with discontinuities is still attractive. It is desirable to understand the scattering from defects with complex geometry. The first step for the L(0,2) mode study could be the development of the waveguide model with irregularly shaped defects. This could be achieved by modelling the defect as a superposition of small steps which then are connected with proper boundary conditions. Another important area that could be investigated is the three-dimensional scattering in plate and pipe structures.

Secondly, the study with the torsional mode T(0,1) showed that the reflection from an axial crack is quite weak and its sizing and circumferential positioning is complicated. However, recently it has been demonstrated [94] that it is possible to use the same torsional mode for imaging of pipe features. The pipe image which is reconstructed by using synthetic focusing of the recorded signals shows the information about the location and severity of defects. Moreover, it has been shown that there is a large increase in defect sensitivity when using this technique over simple screening as used in this work. This might be helpful in detecting and characterizing axial defects in pipe-lines. The research on this has already been started and the first results will be reported in [P1].

References

- [1] D. N. Alleyne and P. Cawley. Long range propagation of Lamb waves in chemical plant pipework. *Mater. Eval.*, 55:504–508, 1995.
- [2] P. Wilcox. Omni-directional guided wave transducer arrays for the rapid inspection of large areas of plate structures. *IEEE Trans. Ultrason. Ferroelectr. Freq. Control*, 50(6):699–709, 2003.
- [3] D. N. Alleyne, B. Pavlakovic, M. J. S. Lowe, and P. Cawley. Rapid, long range inspection of chemical plant pipework using guided waves. *Insight*, 43(2):93–96,101, 2001.
- [4] D. N. Alleyne and P. Cawley. The interaction of Lamb waves with defects. *IEEE Trans. Trans. Ultrason. Ferroelectr. Freq. Control*, 39(3):381–397, 1992.
- [5] Y. Cho, D. D. Hongerholt, and J. L. Rose. Lamb wave scattering analysis for reflector characterization. *IEEE Trans. Trans. Ultrason. Ferroelectr. Freq. Control*, 44(1):44–52, 1997.
- [6] A. Gunawan and S. Hirose. Mode-exciting method for Lamb wave-scattering analysis. *J. Acoust. Soc. Am.*, 115(3):996–1005, 2004.
- [7] B. A. Auld. *Acoustic fields and waves in solids. Volume 2*. Krieger Publishing Company, Malabar, Florida, 1990.
- [8] H. E. Engan. Torsional wave scattering from a diameter step in a rod. *J. Acoust. Soc. Am.*, 104(4):2015–2024, 1998.
- [9] T. Vogt, M. Lowe, and P. Cawley. The scattering of guided waves in partly embedded cylindrical structures. *J. Acoust. Soc. Am.*, 113(3):1258–1272, 2003.
- [10] T. Grahn. Lamb wave scattering from a circular partly through-thickness hole in a plate. *Wave Motion*, 37:63–80, 2003.
- [11] Xiao-Min Wang, C. F. Ying, and Ming-Xuan Li. Scattering of antiplane shear waves by a circular cylinder in a traction-free plate. *J. Acoust. Soc. Am.*, 108(3):913–923, 2000.
- [12] M. Castaings, E. Le Clezio, and B. Hosten. Modal decomposition method for modeling the interaction of Lamb waves with cracks. *J. Acoust. Soc. Am.*, 112(6):1258–1272, 2002.
- [13] D. C. Gazis. Three-dimensional investigation of the propagation of waves in hollow circular cylinders. I. Analytical foundation. *J. Acoust. Soc. Am.*, 31(5):568–573, 1959.

- [14] B. Pavlakovic. *Leaky guided ultrasonic waves in NDT*. PhD thesis, University of London, 1998.
- [15] W. H. Press, S. A. Teukolsky, W. T. Vetterling, and B. P. Flannery. *Numerical recipes in FORTRAN 77: the art of parallel scientific computing. 2nd Edition*. Cambridge University Press, New York, 1992.
- [16] M. Silk and K. Bainton. The propagation in metal tubing of ultrasonic wave modes equivalent to Lamb waves. *Ultrasonics*, 17(1):11–19, 1979.
- [17] H. Nishino, S. Takashina, F. Uchida, M. Takemoto, and K. Ono. Modal analysis of hollow cylindrical guided waves and applications. *Jpn. J. Appl. Phys.*, 40(1):364–370, 2001.
- [18] B. Pavlakovic, M. Lowe, D. Allayne, and P. Cawley. Disperse: A general purpose program for creating dispersion curves. *In Review of Progress in Quantitative NDE, edited by D. Thompson and D. Chimenti*, (Plenum, New York), 16:185–192, 1997.
- [19] John J. Ditri and Joseph L. Rose. Excitation of guided elastic wave modes in hollow cylinders by applied surface tractions. *J. Appl. Phys.*, 72(1):2589–2597, 1992.
- [20] Y. Cho and J. L. Rose. A boundary element solution for a mode conversion study on the edge reflection of Lamb waves. *J. Acoust. Soc. Am.*, 100(1):92–97, 1996.
- [21] B. Morvan, N. Wilkie-Chancellier, H. Duflo, A. Tinel, and J. Duclos. Lamb wave reflection at the free edge of a plate. *J. Acoust. Soc. Am.*, 113(3):1417–1425, 2003.
- [22] O. Diligent and M. J. S. Lowe. Prediction and measurement of nonpropagating Lamb modes at the free end of a plate when the fundamental antisymmetric mode a_0 is incident. *J. Acoust. Soc. Am.*, 113(6):1417–1425, 2003.
- [23] H. Bian and J. L. Rose. A physical interpretation of elastic guided-wave reflection from normal ends of a waveguide. *IEEE Trans. Trans. Ultrason. Ferroelectr. Freq. Control*, 51(7):838–847, 2004.
- [24] J. M. Galán and R. Abascal. Lamb mode conversion at edges. A hybrid boundary element-finite element solution. *J. Acoust. Soc. Am.*, 117(4):1777–1784, 2005.
- [25] G. Ribay, S. Catheline, and D. Clorennec. A_0 mode interaction with a plate free edge: theory and experiments at very low frequency by thickness product. *J. Acoust. Soc. Am. Lett.*, 122(2):711–714, 2007.

- [26] P. J. Torvik. Reflection of wave trains in semi-infinite plates. *J. Acoust. Soc. Am.*, 41(2):346–353, 1967.
- [27] B. A. Auld and M. T. Tsao. A variational analysis of edge resonance in a semi-infinite plate. *IEEE Trans. Sonics. Ultrason.*, SU-24(5):317–326, 1977.
- [28] V. T. Grinchenko and N. S. Gorodetskaya. Excitation of the edge mode in an elastic half strip. *Int. Appl. Mech.*, 34(2):115–122, 1998.
- [29] E. Le Clezio, M. V. Predoi, M. Castaings, B. Hosten, and M. Rousseau. Numerical predictions and experiments on the free-plate edge mode. *Ultrasonics*, 41(1):25–40, 2003.
- [30] N. Wilkie-Chancellier, H. Duflo, A. Tinel, and J. Duclos. Numerical description of the edge mode at the beveled extremity of a plate. *J. Acoust. Soc. Am.*, 117(1):194–199, 2005.
- [31] V. Pagneux. Revisiting the edge resonance for Lamb waves in a semi-infinite plate. *J. Acoust. Soc. Am.*, 120(2):649–656, 2006.
- [32] V. Zernov, A. V. Pichugin, and J. Kaplunov. Eigenvalue of a semi-infinite elastic strip. *Proc. R. Soc. A*, 462:1255–1270, 2006.
- [33] E. A. G. Shaw. On the resonant vibrations of thick barium titanate disks. *J. Acoust. Soc. Am.*, 28(1):38–50, 1956.
- [34] J. Oliver. Elastic wave dispersion in a cylindrical rod by a wide-band short duration pulse technique. *J. Acoust. Soc. Am.*, 29(2):189–194, 1957.
- [35] H. D. McNiven. Extensional waves in a semi-infinite elastic rod. *J. Acoust. Soc. Am.*, 33(1):23–27, 1961.
- [36] J. Zemanek. An experimental and theoretical investigation of elastic wave propagation in a cylinder. *J. Acoust. Soc. Am.*, 51(1B):265–282, 1972.
- [37] R. D. Gregory and I. Gladwell. Axisymmetric waves in a semi-infinite elastic rod. *Q. J. Mech. Appl. Math.*, 42(2):327–337, 1989.
- [38] M. de Billy. End resonance in infinite immersed rods of different cross sections. *J. Acoust. Soc. Am.*, 99(4):2097–2109, 1996.
- [39] J. Tasi. Reflection of extensional waves at the end of a thin cylindrical shell. *J. Acoust. Soc. Am.*, 44(1):291–292, 1968.
- [40] J. Kaplunov, L. Y. Kossovich, and M. V. Wilde. Free localized vibrations of a semi-infinite cylindrical shell. *J. Acoust. Soc. Am.*, 107(3):1383–1393, 2000.

- [41] V. T. Grinchenko and G. L. Komissarova. Features of the dynamic deformation of a hollow cylinder. *Int. Appl. Mech.*, 22(5):393–397, 1986.
- [42] Abaqus. *Analysis user's manual. Abaqus 6.5*. Abaqus, 2004.
- [43] D. N. Alleyne, M. J. S. Lowe, and P. Cawley. The reflection of guided waves from circumferential notches in pipes. *J. Appl. Mech.*, 65(3):635–641, 1998.
- [44] M. J. S. Lowe, D. N. Alleyne, and P. Cawley. The mode conversion of a guided wave by a part-circumferential notch in a pipe. *J. Appl. Mech.*, 65(3):649–656, 1998.
- [45] M. Castaings and C. Bacon. Finite element modeling of torsional wave modes along pipes with absorbing materials. *J. Acoust. Soc. Am.*, 119(6):3741–3751, 2006.
- [46] B. Pavlakovic, D. Alleyne, M. Lowe, and P. Cawley. Simulation of Lamb wave propagation using pure mode excitation. In *Review of Progress in Quantitative NDE*, edited by D. Thompson and D. Chimenti, (Plenum, New York), 17:1003–1010, 1998.
- [47] R. D. Gregory and I. Gladwell. The reflection of a symmetric Rayleigh-Lamb wave at the fixed or free edge of a plate. *J. Elast.*, 13(2):185–206, 1983.
- [48] S. I. Rokhlin. Diffraction of Lamb waves by a finite crack in an elastic layer. *J. Acoust. Soc. Am.*, 67(4):1157–1165, 1980.
- [49] M. Koshiya, S. Karakida, and M. Suzuki. Finite-element analysis of Lamb wave scattering in elastic plate waveguide. *IEEE Trans. Trans. Son. Ultrason.*, SU-31(1):18–25, 1984.
- [50] S. W. Liu, S. K. Datta, and T. H. Ju. Transient scattering of Rayleigh-Lamb wave by a surface-breaking crack: comparison of numerical simulation and experiment. *J. Nond. Eval.*, 3:111–126, 1991.
- [51] T. Ghosh, T. Kundu, and P. Karpur. Efficient use of Lamb modes for detecting defects in large plates. *Ultrasonics*, 36:791–801, 1998.
- [52] M. J. S. Lowe and O. Diligent. Low-frequency reflection characteristics of the s_0 Lamb wave from a rectangular notch in a plate. *J. Acoust. Soc. Am.*, 111(1):64–74, 2002.
- [53] M. J. S. Lowe, P. Cawley, J-Y. Kao, and O. Diligent. The low-frequency reflection characteristics of the fundamental antisymmetric Lamb wave a_0 from a rectangular notch in a plate. *J. Acoust. Soc. Am.*, 112(6):2612–2622, 2002.

- [54] P. S. Tua, S. T. Quek, and Q. Wang. Detection of cracks in plates using piezo-actuated Lamb waves. *Smart. Mater. Struct.*, 13:643–660, 2004.
- [55] M. A. Flores-López and R. D. Gregory. Scattering of Rayleigh-Lamb waves by a surface breaking crack in an elastic plate. *J. Acoust. Soc. Am.*, 119(4):20412049, 2006.
- [56] E. Glushkov, N. Glushkova, M. Golub, and A. Boström. Natural resonance frequencies, wave blocking, and energy localization in an elastic half-space and waveguide with a crack. *J. Acoust. Soc. Am.*, 119(6):3589–3598, 2006.
- [57] N. Terrien, D. Osmont, D. Royer, F. Lepoutre, and A. Déom. A combined finite element and modal decomposition method to study the interaction of Lamb modes with micro-defects. *Ultrasonics*, 46:74–88, 2007.
- [58] C. M. Fortunko and R. E. Schramm. Evaluation of pipeline girth welds using low-frequency horizontally polarized waves. *J. NDE*, 3(3):155–173, 1982.
- [59] J. Ditri. Utilization of guided elastic waves for the characterization of circumferential cracks in hollow cylinders. *J. Acoust. Soc. Am.*, 96(1):3769–3775, 1994.
- [60] P. Cawley, M. J. S. Lowe, F. Simonetti, C. Chevalier, and A. G. Roosenbrand. Lamb wave scattering analysis for reflector characterization. *IEEE Trans. Trans. Ultrason. Ferroelectr. Freq. Control*, 44(1):44–52, 1997.
- [61] W. Zhuang, A. H. Shah, and S. K. Datta. Axisymmetric guided wave scattering by cracks in welded steel pipes. *J. Press. Vessel Tech.*, 119:401–406, 1997.
- [62] H. Bai, A. H. Shah, N. Popplewell, and S. K. Datta. Scattering of guided waves by circumferential cracks in steel pipes. *Trans. ASME, J. Appl. Mechanics*, 68:619–631, 2001.
- [63] A. Demma, P. Cawley, and M. J. S. Lowe. Scattering of the fundamental shear horizontal mode from steps and notches in plates. *J. Acoust. Soc. Am.*, 113(4):1880–1891, 2003.
- [64] A. Demma, P. Cawley, M. J. S. Lowe, A. G. Roosenbrand, and B. Pavlakovic. The reflection of guided waves from notches in pipes: a guide for interpreting corrosion measurements. *J. NDT&E Int.*, 37:167–180, 2004.
- [65] P. S. Tua, S. T. Quek, and Q. Wang. Detection of cracks in cylindrical pipes and plates using piezo-actuated Lamb waves. *Smart. Mater. Struct.*, 14:1325–1342, 2005.
- [66] C. Pecorari. On the complex conjugate roots of the Rayleigh equation: the leaky surface wave. *Wave Motion*, 33:259–270, 2001.

- [67] C. M. Fortunko and R. B. King. Nondestructive evaluation of planar defects in plates using low-frequency shear horizontal waves. *J. Appl. Phys.*, 53(5):3450–3458, 1982.
- [68] Z. Abduljabbar and S.K. Datta. Diffraction of horizontally polarized shear waves by normal edge cracks in a plate. *Appl. Phys.*, 54(2):461–472, 1983.
- [69] M. Koshiha, K. Hasegawav, and M. Suzuki. Finite-element solution of horizontally polarized shear wave scattering in an elastic plate. *IEEE Trans. Ultrason. Ferroelectr. Freq. Control*, 34(4):461–466, 1987.
- [70] J. J. Ditri. Some results on the scattering of guided elastic SH waves from material and geometric waveguide discontinuities. *J. Acoust. Soc. Am.*, 100(5):3078–3087, 1996.
- [71] P. Rajagopal and M. J. S. Lowe. Short range scattering of the fundamental shear horizontal guided wave mode normally incident at a through-thickness crack in an isotropic plate. *J. Acoust. Soc. Am.*, 122(3):1527–1538, 2007.
- [72] P. Rajagopal and M. J. S. Lowe. Angular influence on the scattering of fundamental shear horizontal guided waves by a through-thickness crack in an isotropic plate. *J. Acoust. Soc. Am.*, 124(4):2021–2030, 2008.
- [73] P. Fromme and M. B. Sayir. Measurement of the scattering of a Lamb wave by a through hole in a plate. *J. Acoust. Soc. Am.*, 111(3):1165–1170, 2002.
- [74] I. A. Viktorov. *Rayleigh and Lamb waves*. Plenum, New York, 1970.
- [75] J. A. Ogilvy and J. A. G. Temple. Diffraction of elastic waves by cracks: application to time-of-flight inspection. *Ultrasonics*, 21:259–269, 1983.
- [76] K. F. Graff. *Wave motion in elastic solids*. Dover, New York, 1975.
- [77] D. N. Alleyne and P. Cawley. Optimization of Lamb wave inspection techniques. *NDT&E Int*, 25(1):11–22, 1992.
- [78] A. Demma, P. Cawley, and M. J. S. Lowe. The reflection of the fundamental torsional mode from cracks and notches in pipes. *J. Acoust. Soc. Am.*, 114(2):611–625, 2003.
- [79] P. Wilcox. Modeling the excitation of Lamb and SH waves by point and line sources. In *Review of Progress in Quantitative NDE*, edited by D. Thompson and D. Chimenti, (Plenum, New York), 23:206–213, 2003.
- [80] K.-J. Bathe. *Finite element procedures in engineering analysis*. Prentice Hall, Englewood Cliffs, NJ, 1982.

- [81] A. A. Oliner. Waveguides for acoustic surface waves: a review. *Proc. IEEE*, 64(5):615–627, 1976.
- [82] C. T. Schröder and W. R. Scott Jr. On the complex conjugate roots of the Rayleigh equation: the leaky surface wave. *J. Acoust. Soc. Am.*, 110(6):2867–2877, 2001.
- [83] P. Rajagopal and M. J. S. Lowe. Scattering of the fundamental shear horizontal guided waves by a part-thickness crack in an isotropic plate. *J. Acoust. Soc. Am.*, 124(5):2895–2904, 2008.
- [84] P. Rajagopal. *Towards higher resolution guided wave inspection: scattering studies*. PhD thesis, Imperial College London, 2007.
- [85] W. Mohr and P. Höller. Some results on the scattering of guided elastic SH waves from material and geometric waveguide discontinuities. *IEEE Trans. Son. and Ultrason.*, Su-23(5):369–374, 1976.
- [86] Y-M. Cheong, D-H. Lee, and H-K. Jung. Ultrasonic guided wave parameters for detection of axial cracks in feeder pipes of PHWR nuclear power plants. *Ultrasonics*, 42:883–888, 2004.
- [87] J. Li and J. L. Rose. Excitation and propagation of non-axisymmetric guided waves in a hollow cylinder. *J. Acoust. Soc. Am.*, 109(2):457–464, 2000.
- [88] W. Luo, J. L. Rose, and H. Kwun. Circumferential shear horizontal wave axial-crack sizing in pipes. *Research in Nondestructive Evaluation*, 15:149–171, 2004.
- [89] H. Kwun, S. Y. Kim, H. Matsumot, and S. Vinogradov. Detection of axial cracks in tube and pipe using torsional guided waves. *In Review of Progress in Quantitative NDE*, edited by D. Thompson and D. Chimenti, (Plenum, New York), 27:193–199, 2008.
- [90] D. N. Alleyne and P. Cawley. The excitation of Lamb waves in pipes using dry-coupled piezoelectric transducers. *Nondestr. Eval.*, 15(1):11–20, 1996.
- [91] A. Velichko and P. D. Wilcox. Excitation and scattering of guided waves: Relationships between solutions for plates and pipes. *J. Acoust. Soc. Am.*, 125(6):3623–3631, 2009.
- [92] Z. Liu, C. He, B. Wu, X. Wang, and S. Yang. Circumferential and longitudinal defect detection using T(0,1) mode excited by thickness shear mode piezoelectric elements. *Ultrasonics*, 44:e1135–e1138, 2006.
- [93] Guided Ultrasonics Ltd., last date visited 8/05/09, <http://www.guided-ultrasonics.com>.

- [94] J. Davis and P. Cawley. The application of synthetic focusing for imaging crack-like defects in pipelines using guided waves. *IEEE Trans. Trans. Ultrason. Ferroelectr. Freq. Control*, 56(4):759–771, 2009.

List of publications

- [P1] S. Fletcher, M. J. S. Lowe, M. Ratssepp and C. Brett. Implementation of focused guided waves to locate axial defects in pipes. *In Review of Progress in Quantitative NDE*, edited by D. Thompson and D. Chimenti, (Plenum, New York), 2010 (accepted).
- [P2] M. Ratssepp, S. Fletcher and M. J. S. Lowe. Scattering of the fundamental torsional mode at an axial crack in a pipe. *Journal of Acoustical Society of America*, 2010 (accepted).
- [P3] M. Ratssepp, M. J. S. Lowe. SH₀ Mode Interaction with the Propagation Directional Crack in a Plate. *In Review of Progress in Quantitative NDE*, edited by D. Thompson and D. Chimenti, (Plenum, New York), 28:161 - 168, 2009.
- [P4] M. Ratssepp, M. J. S. Lowe, P. Cawley and A. Klauson. Scattering of the fundamental shear horizontal mode in a plate when incident at a through-crack aligned in the propagation direction of the mode. *Journal of Acoustical Society of America*, 124(5):2873 - 2882, 2008.
- [P5] M. Ratssepp, A. Klauson, F. Chati, F. Léon and G. Maze. Edge resonance in semi-infinite thick pipe: numerical predictions and measurements. *Journal of Acoustical Society of America*, 124(2):875 - 885, 2008.
- [P6] M. Ratssepp, A. Klauson, F. Chati, F. Léon and G. Maze. Edge resonances in semi-infinite thick pipe: theoretical predictions and measurements. *In Special Issue of the Revista de Acustica: 19th International Congress on Acoustics*, Madrid, Spain, 2-7 September, Sociedad Acústica Española, 1-6, 2007.
- [P7] M. Ratssepp, A. Klauson. Curvature effects on wave propagation in an infinite pipe. *Ultragarsas*, 2(59):19 - 25, 2006.
- [P8] M. Ratssepp, J. Metsaveer and A. Klauson. Model of the plugging detection in metallic pipes using ultrasonic guided waves. *In Proceedings: 11th International Congress on Sound and Vibration*, St. Petersburg, Russia, International Institute of Acoustics and Vibration, 1937 - 1942, 2004.
- [P9] M. Ratssepp, J. Metsaveer, A. Klauson, D. Décultot and G. Maze. Synthesis of the echo-signal from a cylindrical shell. *In Proceedings: 10th International Congress on Sound and Vibration*, Stockholm, Sweden, 7-10 July, International Institute of Acoustics and Vibration, 2483-2490, 2003.

Abstract

The thesis investigates some aspects of the wave propagation and interaction with discontinuities in an isotropic plate and cylindrical pipe. The motivation comes from the need to find and characterize defects in plate structures and pipe-lines by employing non-destructive testing procedures which are based on long range ultrasonic guided wave measurements. Two main themes are addressed.

The first part examines the interaction of axisymmetric longitudinal wave with a free edge of a pipe and circumferential crack. The problems are analyzed with a two-dimensional waveguide model by employing numerical method based on normal mode expansion and finite element simulations. It is shown theoretically and experimentally that in case of the incident $L(0,2)$ mode the pipe edge resonance phenomenon at a specific frequency exists. The importance of the inhomogeneous and nonpropagating wave modes on the resonance generation mechanism is explained. Also, the influence of pipe curvature on the phenomenon is studied. The reflection analysis of the $L(0,2)$ mode from surface-breaking circumferential cracks helps to reveal differences between scattering from inner and outer surface crack in thick-walled pipes.

The second part studies the ways how to detect cracks in plates and pipes which are aligned in the direction of the testing wave. Shear horizontal mode SH_0 in a plate and torsional mode $T(0,1)$ in a pipe are used for such tests. Both waves have the wave field perpendicular to the propagation direction of the wave and therefore are expected to be sensitive to such defects. Finite element method and experiments are used to investigate the scattering from a defect. A systematic analysis of the effect of crack length, depth, excitation frequency and plate/pipe geometry on the reflection from cracks is presented and the defect detection possibility is discussed.

Kokkuvõte

Käesolev töö uurib mõningaid aspekte lainelevist ja lainete interaktsioonist geomeetriliste iseärasustega isotroopsetes plaatides ja silindrilistes torudes. See uuring on vajalik ultrahelil põhinevate mittepurustava kontrolli meetodite täiustamiseks, mille eesmärk on hõlbustada defektide avastamist ja iseloomustamist. Vaadeldakse kahte teemat.

Töö esimeses osas uuritakse telgsümmeetriliste pikilainete interaktsiooni toru vaba servaga ning toru ringsuunalise praoga. Antud probleeme analüüsitakse kahemõtmelise lainejuhi mudeliga, mida lahendatakse normaalmoodide superpositsiooni meetodit ja lõplike elementide meetodit kasutades. Näidatakse teoreetiliselt ja eksperimentaalselt, et teatud sagedusel põhjustab lainemood $L(0,2)$ toru serva resonantsi. Selgitatakse mittehomogeensete ja mittelevivate lainete tähtsust resonantsi tekkemehhanismis. Samuti vaadeldakse toru kõveruse mõju antud protsessile. Lainemoodi $L(0,2)$ peegelduse analüüs toru ringsuunalistelt pragudelt aitab välja tuua erinevused lainete hajumises toru seina sise- ja välispinna pragudelt pakuseinalistes torudes.

Töö teises osas uuritakse, kuidas oleks võimalik avastada plaatides ja torudes pragusid, mis on suunatud kontroll-laine levimise suunas. Selleks kasutatakse nihkelainet $SH0$ plaadis ja väändelainet $T(0,1)$ torus. Mõlema laine laineväli on risti laine levimise suunaga, mille tõttu nad võivad olla tundlikud selliste defektide suhtes. Defektil hajunud lainevälja uuritakse lõplike elementide mudeli abil ning eksperimentaalselt. Teostatakse süstemaatiline analüüs, milles käsitletakse prao pikkuse, sügavuse, testsageduse ja plaadi/toru geomeetria mõju praolt peegeldunud laine parameetritele ning diskuteeritakse prao avastamise võimalikkuse üle.

Curriculum Vitae

1. Personal information

Name: Madis Ratassepp
Date and place of birth: 15.03.1981, Valga, Estonia
Nationality: Estonian
E-mail address: madisr@hotmail.ee

2. Education

Tallinn University of Technology (2005), MSc in Engineering Physics
Tallinn University of Technology (2003), BA in Engineering Physics

3. Language skills (basic, intermediate or high level)

Estonian - native language
English - high
Russian - intermediate

4. Special Courses

Imperial College London, 2006-2008, Finite Element method software ABAQUS

5. Professional Employment

Tallinn University of Technology, 2005- ..., assistant
Peipmani Inseneribüroo OÜ (Inseneribüroo Printsip OÜ), 2004-2006, engineer-designer

6. Defended theses

Wave propagation in elastic hollow cylinder, Master's degree
Wave scattering from cylindrical shells, Bachelor's degree

7. Honours and awards

TUT Development Foundation (Jaanus Ots) PhD Scholarship, 2009
Prize from the competition of the best scientific publication in TUT in the field of technology, 2008
Imperial College NDT Group Scholarship, 2006
Archimedes Foundation, Kristjan Jaak Scholarship, 2006

8. Main areas of scientific work

Modelling wave propagation in elastic structures

9. Other research projects

Mechanics of fluid-structure interaction

Probabilistic modelling of NDT crack detection

Signature:

Date:

Elulookirjeldus

1. Isikuandmed

Ees- ja perekonnanimi: Madis Ratassepp
Sünniaeg ja -koht: 15.03.1981, Valga, Eesti
Kodakondsus: eestlane
E-posti aadress: madisr@hotmail.ee

2. Hariduskäik

Tallinna Tehnikaülikool (2005), tehnilise füüsika magister
Tallinna Tehnikaülikool (2003), tehnilise füüsika bakalaureus

3. Keelteoskus (alg-, kesk- või kõrgtase)

eesti keel - emakeel
inglise keel - kõrgtase
vene keel - kesktase

4. Täiendusõpe

Imperial College London, 2006-2008, Lõplike elementide meetodi tarkvara ABAQUS

5. Teenistuskäik

Tallinna Tehnikaülikool, 2005- ..., assistent
Peipmani Inseneribüroo OÜ (Inseneribüroo Printsip OÜ), 2004-2006, insener-joonestaja

6. Kaitstud lõputööd

Lainelevi modelleerimine elastses silindrilises torus, magistritöö
Kajasignaalide hajumine silindrilistel koorikutel, bakalaureusetöö

7. Teaduspreemiad ja -tunnustused

SA TTÜ Arengufondi doktoriõppe (Jaanus Ots) stipendium, 2009
TTÜ aasta parima teadusartikli auhinnaline koht tehnika ja tehnoloogia valdkonnas, 2008
Imperial College NDT Group Scholarship, 2006
SA Archimedes, Kristjan Jaagu stipendium, 2006

8. Teadustöö põhisuunad

Lainelevi modelleerimine elastsetes struktuurides

9. Teised uurimisprojektid

Vedeliku ja konstruktsiooni koostoime mehaanika

Tõenäosuslik prao avastamise modelleerimine mittepurustavas kontrollis

Allkiri:

Kuupäev:

**DISSERTATIONS DEFENDED AT
TALLINN UNIVERSITY OF TECHNOLOGY ON
CIVIL ENGINEERING**

1. **Heino Mölder**. Cycle of investigations to improve the efficiency and reliability of activated sludge process in sewage treatment plants. 1992.
2. **Stellian Grabko**. Structure and properties of oil-shale Portland cement concrete. 1993.
3. **Kent Arvidsson**. Analysis of interacting systems of shear walls, coupled shear walls and frames in multi-storey buildings. 1996.
4. **Andrus Aavik**. Methodical basis for the evaluation of pavement structural strength in Estonian Pavement Management System (EPMS). 2003.
5. **Priit Vilba**. Unstiffened welded thin-walled metal girder under uniform loading. 2003.
6. **Irene Lill**. Evaluation of Labour Management Strategies in Construction. 2004.
7. **Juhan Idnurm**. Discrete analysis of cable-supported bridges. 2004.
8. **Arvo Iital**. Monitoring of Surface Water Quality in Small Agricultural Watersheds. Methodology and optimization of monitoring network. 2005.
9. **Liis Sipilgas**. Application of satellite data for monitoring the marine environment. 2006.
10. **Ott Koppel**. Infrastruktuuri arvestus vertikaalselt integreeritud raudtee-ettevõtja korral: hinnakujunduse aspekt (Eesti peamise raudtee-ettevõtja näitel). 2006.
11. **Targo Kalamees**. Hygrothermal criteria for design and simulation of buildings. 2006.
12. **Raido Puust**. Probabilistic leak detection in pipe networks using the SCEM-UA algorithm. 2007.
13. **Sergei Zub**. Combined treatment of sulfate-rich molasses wastewater from yeast industry. Technology optimization. 2007.
14. **Alvina Reihan**. Analysis of long-term river runoff trends and climate change impact on water resources in Estonia. 2008.
15. **Ain Valdmann**. On the coastal zone management of the city of Tallinn under natural and anthropogenic pressure. 2008.
16. **Ira Didenkulova**. Long wave dynamics in the coastal zone. 2008.
17. **Alvar Toode**. DHW consumption, consumption profiles and their influence on dimensioning of a district heating network. 2008.

18. **Annely Kuu.** Biological diversity of agricultural soils in Estonia. 2008.
19. **Andres Tolti.** Hiina konteinerveed läbi Eesti Venemaale ja Hiinasse tagasisaadetavate tühjade konteinerite arvu vähendamise võimalused. 2008.
20. **Heiki Onton.** Investigation of the causes of deterioration of old reinforced concrete constructions and possibilities of their restoration. 2008.
21. **Harri Moora.** Life cycle assessment as a decision support tool for system optimisation – the case of waste management in Estonia. 2009.
22. **Andres Kask.** Lithohydrodynamic processes in the Tallinn Bay area. 2009.
23. **Loreta Kelpšaitė.** Changing properties of wind waves and vessel wakes on the eastern coast of the Baltic Sea. 2009.
24. **Dmitry Kurennoy.** Analysis of the properties of fast ferry wakes in the context of coastal management. 2009.
25. **Egon Kivi.** Structural behavior of cable-stayed suspension bridge structure. 2009.